Chemical Looping Combustion Reactions and Systems

Task 5 Topical Report, Utah Clean Coal Program

Reporting Period Start Date: April 2012

Report Period End Date: August 2013

Principal Authors: Adel F. Sarofim, JoAnn S. Lighty, Philip J. Smith, Kevin J. Whitty, Edward Eyring, Asad Sahir, Milo Alvarez, Michael Hradisky, Chris Clayton, Gabor Konya, Richard Baracki, and Kerry Kelly

Issue date: March 2014

DOE Award Number: DE-NT0005015
Project Officer: David Lang

University of Utah
Institute for Clean & Secure Energy
380 INSCC
155 South, 1452 East
Salt Lake City, UT 84112

DISCLAIMER

ABSTRACT

Chemical Looping Combustion (CLC) is one promising fuel-combustion technology, which can facilitate economic CO_2 capture in coal-fired power plants. It employs the oxidation/reduction characteristics of a metal, or oxygen carrier, and its oxide, the oxidizing gas (typically air) and the fuel source may be kept separate. This topical report discusses the results of four complementary efforts: (5.1) the development of process and economic models to optimize important design considerations, such as oxygen carrier circulation rate, temperature, residence time; (5.2) the development of high-performance simulation capabilities for fluidized beds and the collection, parameter identification, and preliminary verification/uncertainty quantification; (5.3) the exploration of operating characteristics in the laboratory-scale bubbling bed reactor, with a focus on the oxygen carrier performance, including reactivity, oxygen carrying capacity, attrition resistance, resistance to deactivation, cost and availability; and (5.4) the identification of kinetic data for copper-based oxygen carriers as well as the development and analysis of supported copper oxygen carrier material.

Subtask 5.1 focused on the development of kinetic expressions for the Chemical Looping with Oxygen Uncoupling (CLOU) process and validating them with reported literature data. The kinetic expressions were incorporated into a process model for determination of reactor size and oxygen carrier circulation for the CLOU process using ASPEN PLUS. An ASPEN PLUS process model was also developed using literature data for the CLC process employing an iron-based oxygen carrier, and the results of the process model have been utilized to perform a relative economic comparison.

In Subtask 5.2, the investigators studied the trade-off between modeling approaches and available simulations tools. They quantified uncertainty in the high-performance computing (HPC) simulation tools for CLC bed applications. Furthermore, they performed a sensitivity analysis for velocity, height and polydispersity and compared results against literature data for experimental studies of CLC beds with no reaction. Finally, they present an optimization space using simple non-reactive configurations.

In Subtask 5.3, through a series of experimental studies, behavior of a variety of oxygen carriers with different loadings and manufacturing techniques was evaluated under both oxidizing and reducing conditions. The influences of temperature, degree of carrier conversion and thermodynamic driving force resulting from the difference between equilibrium and system O_2 partial pressures were evaluated through several experimental campaigns, and generalized models accounting for these influences were developed to describe oxidation and oxygen release. Conversion of three solid fuels with widely ranging reactivities was studied in a small fluidized bed system, and all but the least reactive fuel (petcoke) were rapidly converted by oxygen liberated from the CLOU carrier. Attrition propensity of a variety of carriers was also studied, and the carriers produced by freeze granulation or impregnation of preformed substrates displayed the lowest rates of attrition.

Subtask 5.4 focused on gathering kinetic data for a copper-based oxygen carrier to assist with modeling of a functioning chemical looping reactor. The kinetics team was also responsible for the development and analysis of supported copper oxygen carrier material.

TABLE OF CONTENTS

DISCLAIMER 1
ABSTRACT 2
LIST OF FIGURES 5
LIST OF TABLES 9
LIST OF ABBREVIATIONS 10
EXECUTIVE SUMMARY 13
INTRODUCTION 16
METHODS 17
Subtask 5.1 – Process Modeling and Economics 17
Development of Kinetic Expressions for CLOU 17
CuO Decomposition 18
Cu_2O Exidation 19
Mexican Petcoke Oxidation 20
Development of a Custom Model for CLOU 20
Development of ASPEN PLUS process models for CLOU and CLC 23
ASPEN PLUS Process Model for CLOU using a Copper-Based Oxygen Carrier 23
ASPEN PLUS Process model for CLC using an Iron-Based Oxygen Carrier 26
Relative Economic Comparison between CLC and CLOU 28
Subtask 5.2 – LES-DQMOM Simulation of a Pilot-Scale Fluidized Bed 30
Kinetic Theory of Granular Flows 31
Modeling Approach 32
Sensitivity Analysis 35
Geometry and Mesh description 35
Subtask 5.3 – Laboratory-Scale CLC Studies 41
Subtask 5.4 – CLC Kinetics 44
Development of Supported Copper Oxide 44
Wet Impregnation Preparation Method 44
Preparation by Rotary Evaporator 44
β-SiC Support Preparation Method 44
TGA Experimental Setup 45
TGA Analysis Procedure 45
Particle Characterization 46
RESULTS AND DISCUSSION 47
Subtask 5.1 – Process Modeling and Economics 47
Development of Kinetic Expressions for CLOU 47
CuO Decomposition 47
Cu_2O Oxidation 49

Mexican Petcoke Oxidation 50
Development of a Custom Model for CLOU 52
Development of ASPEN PLUS Process Models for CLOU and CLC 54
ASPEN PLUS Process Model for CLOU using a Copper-Based Oxygen Carrier 54
ASPEN PLUS Process Model for CLC using an Iron-Based Oxygen Carrier 55
Relative Economic Comparison between CLC and CLOU 57
Subtask 5.2 – LES-DQMOM Simulation of a Pilot-Scale Fluidized Bed 60
Case 1: Monodisperse Model Parameter 60
Case 2: Monodisperse Model Parameter 64
Case 3a: Monodisperse Model Parameter 67
Case 3b: Monodisperse Model Parameter 69
Case 1: DQMOM Three Classes 70
Case 1: DQMOM Five Classes 74
General Analysis 76
Effects of Physical and Modeling parameters 79
Computational Costs 81
Subtask 5.3 – Lab-Scale CLC Studies 82
Measurement and Modeling of O_2 Release by Reduction of CuO 82
Reaction Order with Respect to Oxygen Driving Force 86
Preexponential Factor 87
Overall Expression for Rate of CuO Decomposition 87
Measurement and Modeling of Oxidation of Cu_2O to CuO 88
Influence of Oxygen Partial Pressure 88
Influence of Degree of Conversion 89
Influence of Temperature on Oxidation Rate 92
High Temperature Model Comparison 93
Conversion of Solid Fuels with CLOU Carriers 94
Evaluation of Attrition Rates for Various Copper-based Carriers 99
Subtask 5.4 – CLC Kinetics 102
SEM Images 111
CONCLUSIONS 113
REFERENCES 115

LIST OF FIGURES

Figure 1. Schematic of CLC. A metal and its oxide are looped between the air reactor and the fuel reactor. By separating the air from the fuel a nearly pure CO_2 stream may be generated. 16

Figure 2. Design of a CLC reactor using natural gas proposed by Lyngfelt. Section 1: air reactor (AR)/riser. Section 2: cyclone to separate oxygen depleted air from the oxygen carrier. Section 3: fuel reactor (FR). Sections 4: loop seals. (Bergurand and Lyngfelt, 2009). 17

Figure 3. Mass of copper loading per MW_{th} vs mole ratio of CuO at the exit of fuel reactor for different values of ΔX_S. 25

Figure 4. Residence time in a reactor (on logarithmic scale) versus temperature (— CuO reduction, - - Cu_2O Oxidation, •• PRB coal char burnout). 25

Figure 5. Schematic of ASPEN PLUS process model for CLOU with CuO-ZrO_2 as an oxygen carrier. . 26

Figure 6. Schematic of ASPEN PLUS process model for CLC with Fe_2O_3-Al_2O_3 as an oxygen carrier... 28

Figure 7. Experimental PSD. 34

Figure 8. Schematic drawing of the bubbling fluidized bed unit. 37

Figure 9. Ring sparger for air distribution inside the unit. 37

Figure 10. The complete BFB system created in STAR-CCM+. a) Entire unit. b) Ring sparger side view. c) Ring sparger bottom view. 38

Figure 11. Reduced geometrical representation of the BFB, containing only the fluidized bed. 39

Figure 12. Complete geometry mesh. a) Bottom half. b) Top half. c) Mesh refining around the ring sparger. 40

Figure 13. Mesh for the reduced geometry. a) Overall mesh. b) Sparger mesh detail. 41

Figure 14. Schematic of the bubbling bed CLC reactor system at the University of Utah. 43

Figure 15. Logarithm of rate constant of CuO decomposition (ln k_{CuO}) versus $1/T_{avg}$ [▲ Experimental Data, − Equation Fit, - - Error Bar representing the temperature measurement range, − ·· − Error bar representing the scenario if the outlet partial pressure of O_2 is reduced by half. 48

Figure 16. Comparison of experimental data and prediction from rate equation of CuO decomposition with time [■ Experimental Data: 900°C, ···· Prediction: 900°C , ▲ Experimental Data: 950°C, − − − Predictions:950° C, ● Experimental Data: 985°C, − Prediction:985°C]. 48

Figure 17. Comparison of experimental data for conversion of Cu_2O versus time at temperatures of 950°C (oxidation with 10% O_2 in N_2) with the Equation 5.1.11 derived by the law of additive reaction times for $k_{app,Cu2O} = 18.6\ s^{-1}$ (● experimental data points, - - - conversion for chemical reaction control). 50

Figure 18. Logarithm of global reaction rate constant of Mexican petcoke oxidation (ln $k_{r,C}$) versus $1/T_{avg}$ [♦ experimental data, − equation fit]. 51

Figure 19. Comparison of experimental data and prediction by rate equation of Mexican Petcoke particles with time [■ experimental data: 900°C, ···· prediction: 900° C, ▲ experimental data: 950°C, − − − prediction: 950°C, ● experimental data: 985°C, −prediction: 985°C]. 52

Figure 20. O_2 concentration trends at 950°C (♦ Experimental data, — ¨ — O_2 equilibrium concentration for the reaction $4CuO(s) \rightarrow 2Cu_2O(s)+O_2(g)$ determined from experimental temperature measurements, —— Model predictions of the O_2 concentration, - - Model predictions of the O_2 concentration in the bubble phase, ¨ Model predictions of the O_2 concentration in the emulsion phase). 53

Figure 21. CO_2 concentration trends at 950°C (♦ Experimental data, —— Model predictions of the CO_2 concentration.¨ Model predictions of the CO_2 concentration in the emulsion phase, - - Model predictions of the CO_2 concentration in the bubble phase)..... 53

Figure 22. Relative capital costs of CLC and CLOU associated with 1 MW_{th} capacity. 58

Figure 23. Relative capital costs of CLC and CLOU associated with 10 MW_{th} capacity. 59

Figure 24. Relative capital costs of CLC and CLOU associated with 100 MW_{th} capacity. 59

Figure 25. Relative operating costs of CLC and CLOU associated with 1, 10 and 100 MW_{th} capacity. ... 60

Figure 26. Volume fraction profiles for Case 1, monodisperse (v = 0.3 m/s, h = 2.44 m) at t = 0.0 s. 61

Figure 27. Volume fraction profiles for Case 1, monodisperse (v = 0.3 m/s, h = 2.44 m) at t = 2.4 s. 62

Figure 28. Volume fraction profiles for Case 1, monodisperse (v = 0.3 m/s, h = 2.44 m) t = 5.9 s. 63

Figure 29. Time-averaged pressure drop profiles for Case 1 with monodisperse model during the first 6 seconds of the simulation. 63

Figure 30. Volume fraction profiles for Case 2, monodisperse (v = 0.3 m/s, h = 3.66 m) t = 0.0 s. 64

Figure 31. Volume fraction profiles for Case 2, monodisperse (v = 0.3 m/s, h = 3.66 m) t = 2.4 s. 65

Figure 32. Volume fraction profiles for Case 2, monodisperse (v = 0.3 m/s, h = 3.66 m) t = 5.9 s. 66

Figure 33. Time-averaged pressure drop profiles for Case 2 with monodisperse model for the first 6 seconds. 66

Figure 34. Volume fraction profiles for Case 3a, monodisperse (v = 0.6 m/s, h = 1.22 m) t = 0.0 seconds. 67

Figure 35. Volume fraction profiles for Case 3a, monodisperse (v = 0.6 m/s, h = 1.22 m) t = 1.3 seconds. 68

Figure 36. Volume fraction profiles for Case 3a, monodisperse (v = 0.6 m/s, h = 1.22 m) t = 4.0 seconds. 68

Figure 37. Time-averaged pressure drop profiles for Case 3a, monodisperse model for the first 4 seconds. 69

Figure 38. Effect of the superficial velocity in the fluidized bed 70

Figure 39. Volume fraction profiles, DQMOM 3 classes (v = 0.3 m/s, h = 2.44 m) t = 0.0 s. 71

Figure 40. Volume fraction profiles DQMOM 3 classes (v = 0.3 m/s, h = 2.44 m) t = 2.0 s. 72

Figure 41. Volume fraction profiles DQMOM 3 classes (v = 0.3 m/s, h = 2.44 m) t = 5.7 s. 73

Figure 42. Time-averaged pressure drop profiles for simulation of Case 1 using DQMOM 3 classes during the first 5.7 seconds of the simulation. 73

Figure 43. Volume fraction profiles DQMOM 5 classes (v = 0.3 m/s, h = 2.44 m) t = 0.1 s. 74

Figure 44. Volume fraction profiles DQMOM 5 classes (v = 0.3 m/s, h = 2.44 m) t = 1.6 s. 75
Figure 45. Time-averaged pressure drop profiles for DQMOM 5 classes, during the first 1.6 s. 75
Figure 46. Direct comparison of simulation results carried out by PSRI-NETL (Shadle, et al. 2011) and simulation results in this study for Case 1 monodisperse and Case 1 DQMOM with 3 classes..... 77
Figure 47. Direct comparison of simulation results carried out by PSRI-NETL (Shadle, et al. 2011) and simulation results in this study for Case 2 monodisperse. 78
Figure 48. Direct comparison of simulation results carried out by PSRI-NETL (Shadle, et al. 2011) and simulation results in this study for Case 3a monodisperse. 79
Figure 49. Relationship between pressure drop and gas velocity for a polydisperse bed (Kunii and Levenspiel 1991). 80
Figure 50. Effect of height for quartz sand fluidization (Mele, 2011). 81
Figure 51. Equilibrium partial pressure of oxygen for the Cu_2O/CuO system. The partial pressure of oxygen in air is displayed with a dashed line. 82
Figure 52. Conversion vs. time for the decomposition of CuO under an N_2 atmosphere in TGA at various temperatures using 45_CuO_ZrO2_FG. Inset shows blow-up of the time interval from 0 to 5 minutes. 83
Figure 53. Arrhenius plot for decomposition of CuO in 45_ZrO2_FG and 50_TiO2_MM. The apparent activation energies are calculated to be 264 kJ/mole and 284 kJ/mole for the zirconia and titania-supported materials, respectively. 84
Figure 54. Arrhenius plot for the decomposition of 45_ZrO2_Fg and 50_TiO2_MM. This data attempts to separate the dual effect of temperature on the kinetic equation (i.e. influence on the activation energy and driving force) thereby generating the corrected activation energies for both materials... 84
Figure 55. Plots to determine the order of reaction with respect to CuO for the 45_ZrO2_FG material (left pair) and 50_TiO2_MM (right pair). Within each pair the left figures are for 800°C and the right figures are for 900°C. Top to bottom represent zero, first and second order. The shapes suggest the reaction to be zero order in CuO. 86
Figure 56. Decomposition of CuO at 950 °C under 3 different supplied oxygen pressures (0.00, 0.020 and 0.034 atm) for both the zirconia- (--) and titania-supported (**) carriers. 87
Figure 57. Reaction rate versus temperature for 4 different CuO-based oxygen carriers in TGA at four different temperatures along with the rates predicted by the rate expression determined in this study. 88
Figure 58. The influence, fpO2, for the oxidation of Cu_2O powder is identified by varying the supplied partial pressure of oxygen during the oxidation cycle of chemical-looping using a zirconia-based supported oxygen carrier. 89
Figure 59. Conversion profile for oxidation of 45_ZrO2_FG material at temperatures from 600°C to 800°C. 90
Figure 60. Pore-blocking kinetics for the low temperature oxidation of Cu_2O in 45_ZrO2_FG. 91

Figure 61. Conversion profiles for the oxidation of Cu_2O at 800°C (left) and 925° C (right) for 45_ZrO2_FG (□) and 50_TiO2_MM (Δ), compared against the model prediction (- - -). 94

Figure 62. Conversion of three different fuels using 50_TiO2_MM material at 930°C. The conversion is calculated from the mass of carbon (as gas) analyzed and collected by infrared analyzer. 96

Figure 63. Conversion of carbon during combustion of green petcoke at 930°C using 50_TiO2_MM in a fluidized bed. 97

Figure 64. Carbon conversion is tracked during the combustion of PRB at 930°C using 45_ZrO2_FG in a fluidized bed. 98

Figure 65. Conversion of carbon (left) and oxygen liberation (right) during the combustion of petcoke particles with a diameter of roughly 3,000 μm at two temperatures using the 45_ZrO2_FG material. 99

Figure 66. Measured mass loss per hour as a result of carrier attrition for the four carriers tested. 102

Figure 67. SEM image of 20% CuO by weight on SiC (Pfaltz & Bauer) prepared by rotary evaporation method and 8 additions of CuO. 104

Figure 68. Box and whisker plot of all k values of the oxidation reactions calculated for 20% CuO by weight on SiC (Pfaltz & Bauer). 105

Figure 69. Box and whisker plot of all k values of the reduction reactions calculated for 20% CuO by weight on SiC (Pfaltz & Bauer). 106

Figure 70. TGA trace of two loops of 42% CuO on SiO_2 at 900°C. 108

Figure 71. One complete oxidation reaction for a 19mg sample of 42% CuO on SiO_2 at 900°C. 109

Figure 72. Oxidation of a 19mg sample of 42% CuO on SiO_2 to 80% Completion at 900°C. 110

Figure 73. One complete reduction reaction for a 19mg sample of 42% CuO on SiO_2 at 900°C. 111

Figure 74. SEM images of the CB16 sample and corresponding EDS images of elemental Cu and Si A) before baking B) after baking C) after fluidization. 112

Figure 75. SEM images of the CB42 sample and corresponding EDS images of elemental Cu and Si A) before baking B) after baking. 112

LIST OF TABLES

Table 1. Reactor dimensions (Mattisson et al. 2009 a). 21
Table 2. Semi-empirical correlations and design relationships utilized for modeling. 22
Table 3. Proximate Analysis for fuels used for comparison (wt. %). 23
Table 4. Ultimate Analysis for fuels used for comparison. 23
Table 5. Correlations and relationships used to perform relative economic analysis. 29
Table 6. Main moment ratios for the experimental distribution 34
Table 7. Sensitivity analysis. 35
Table 8. Copper-based oxygen carriers used. 42
Table 9. Ultimate analysis for non-reactive coals used for comparison (Smith et al. 1994, Mattisson et al. 2009a). 50
Table 10. Parameters for ASPEN PLUS process model and pressure drop calculations for CLOU. 54
Table 11. Energy requirements and contributions (in kW_{th}) obtained from ASPEN PLUS process model for CLOU. 55
Table 12. Parameters for ASPEN PLUS process model and pressure drop calculations for CLC. 56
Table 13. Energy requirements and contributions (in kW_{th}) obtained from ASPEN PLUS process model for CLC. 57
Table 14. Experimental conditions for excluding the influence of oxygen driving force on the rate of reaction at different temperatures. 83
Table 15. Experiments to isolate the influence of O_2 "driving force" on kinetics of CuO decomposition. 86
Table 16. Influence of temperature within the two different temperature regimes for the oxidation of Cu_2O within two different oxygen carriers. 92
Table 17. Model used to predict the conversion of Cu_2O in two different oxygen carriers using the nucleation/growth kinetics expression Avrami-Erofeev. 93
Table 18. Analyses of solid fuels used in this study. 95
Table 19. Experimental conditions for attrition study. U/Umf represents the ratio of actual gas velocity to calculated minimum fluidization velocity. 100
Table 20. Filter schedule utilized in attrition tests. 101
Table 21. Average oxidation and reduction rate constants of copper oxide supported on various materials. All samples were 20% CuO by weight except for Polish Titania (50%) and sand (10%). The results are for the 4^{th} loop of fresh samples. Note that the initial loops consistently differ from later loops. 103

LIST OF ABBREVIATIONS

ACM	Aspen Custom Modeler
AR	Air reactor
BET	Brunauer, Emmett, and Teller equation used to determine surface area of a substance
BFB	Bubbling fluidized bed
CAD	Computer aided design
CFB	Circulating fluidized beds
CFD	Computational fluid dynamics
CLC	Chemical looping combustion
CLOU	Chemical looping with oxygen uncoupling
DQMOM	Direct quadrature method of moments
EDS	Energy dispersive spectroscopy
FBR	Fluidized bed reactor
FR	Fuel reactor
HPC	High performance computing
KTGF	Kinetic theory of granular flows
LES	Large eddy simulation
NDF	Number density function
NETL	National Energy Technology Laboratory
PBE	Population balance equation
PDU	Process development unit
PSD	Particle size distribution
PSRI	Particulate Solid Research, Inc.
PVC	Polyvinyl chloride
RANS	Reynolds-averaged Navier-Stokes
RSTOIC	Stoichiometric reactor model used in ASPEN PLUS
RTD	Residence time distribution
SA	Sigma-Aldrich
SEM	Scanning electron microscopy
SLPM	Standard liters per minute
TGA	Thermogravimetric analysis – a method
TGA	Thermogravimetric analyzer – an instrument
XRD	X-ray diffraction

Nomenclature

b	number of moles of solid B reacted per mole of fluid reactant A
d_b	diameter of the bubble, cm
d_{b0}	initial diameter of the bubble predicted by Mori and Wen's correlation, cm
d_{bi}	diameter of the bubble at a height interval, cm
d_C	diameter of the fuel particle, μm
d_p	diameter of the oxygen carrier particle, μm
$\mathcal{D}$	diffusivity of O_2 in CO_2 (A mixture of 10% O_2 and 90% CO_2 is considered), cm^2/s
D_e	effective diffusivity, m^2/s
D_M	molecular diffusivity, m^2/s
D_T	diameter of the fluidized bed, cm
E	activation energy, kJ/mol

$f_{g,b}$	fraction of fluidized bed volume occupied by gas in bubble phase
$f_{g,e}$	fraction of fluidized bed volume occupied by gas in emulsion phase
$f_1(p_{O_2})$	dependence of rate on oxygen partial pressure
$f_2(X)$	dependence of rate on fractional conversion
g	gravitational constant, cm/s^2
$g_{F_g}(X)$	conversion function for chemical reaction control
h	height of the fluidized bed, cm
ΔH°	standard enthalpy of reaction, kJ/mol
k_{CuO}	reaction rate constant of CuO decomposition, atm^{-1}s^{-1}
$k_{Cu_2O,app}$	apparent reaction rate constant of Cu_2O oxidation, s^{-1}
k_g	reaction rate constant for grain, m/s
$k_{0,CuO}$	pre-exponential factor, atm^{-1}s^{-1}
$k_{r,C}$	reaction rate constant for petcoke oxidation, g/cm^2 s atm$^{0.5}$
K_{BE}	interchange coefficient for gas between bubble and emulsion phases based on bubble volume, cm/s
L_f	length of fluidized bed, cm
L_{mf}	length of fluidized bed at minimum fluidizing conditions, cm
$\dot{m}_{inlet}$	mass flow rate, kg/s
n	isentropic coefficient
n_C	moles of C, moles
n_{CuO}	moles of CuO, moles
$N_{Sh}{}^*$	modified Sherwood number
p_{inlet}	pressure at inlet of reactor, atm
$p_{O_{2,avg}}$	average partial pressure of oxygen in the reactor, atm
$p_{O_{2,in}}$	partial pressure of oxygen at inlet of reactor, atm
$p_{O_2}^e$	partial pressure of oxygen in the equilibrium conditions of CuO decomposition, atm
$p_{O_{2,out}}$	partial pressure of oxygen at the exit of reactor, atm
$p_{O_2}{}^{bbl}$	partial pressure of O_2 in bubble phase, atm
$p_{O_2}{}^{em}$	partial pressure of O_2 in emulsion phase, atm
$p_{O_2}{}^{exit}$	partial pressure of O_2 at exit conditions, atm
$p_{CO_2}{}^{bbl}$	partial pressure of CO_2 in bubble phase, atm
$p_{CO_2}{}^{em}$	partial pressure of CO_2 in emulsion phase, atm.
$p_{CO_2}{}^{exit}$	partial pressure of CO_2 at exit conditions, atm.
$p_{F_p}(X)$	conversion function for pore-diffusion control
$(-r_{CuO})$	rate of CuO decomposition [$4CuO(s) \rightarrow 2Cu_2O(s) + O_2(g)$], 1/s
$(-r_C)$	rate of petcoke oxidation [$C(s) + O_2(g) \rightarrow CO_2(g)$], 1/s
r_C	radius of the carbonaceous fuel particle, m
r_g	radius of a grain, m
r_p	radius of the oxygen carrier particle, m
R	gas constant, cm^3 atm/mol K
R_i	initial radius of coal char particle, cm

t	time, s
t_g^*	dimensionless time
T	temperature, K or °C
T_{avg}	average of the temperature, K or °C
u_b	bubble rising velocity, cm/s
u_e	rise velocity of emulsion through the bed, cm/s
u_0	superficial velocity, cm/s
u_{mf}	minimum velocity for fluidization, cm/s
v_{inlet}	specific volume at inlet of reactor, m^3/kg
V_R	volume of the fluidized bed, cm^3
W	compressor work in kW
X	conversion
X_{CuO}	conversion of CuO particles
X_C	conversion of petcoke particles
z	axial coordinate, cm

Greek Symbols

α	ratio of wake volume to bubble volume
α_S	fraction of particle volume initially occupied by solid reactant
δ	fraction of fluidized bed volume occupied by bubbles
ε	porosity
ε_{mf}	voidage at minimum fluidization conditions
ρ_C	density of carbonaceous particle, g/cm^3
ρ_S	density of oxygen carrier particle, g/cm^3
$\tilde{\rho}_S$	molar density of solid reactant (mol/m^3)
$\tilde{\rho}_{S,Cu_2O}$	molar density of Cu_2O (mol/m^3)
ρ_g	density of gas, g/cm^3
μ	viscosity, kg/m s
$\hat{\sigma}^2$	porous solid reaction modulus

EXECUTIVE SUMMARY

CLC is a novel technology for producing electric power while producing a CO_2-rich stream that can be suitable for sequestration with little additional processing. The typical CLC design is based on a dual fluidized-bed reactor (FBR) system. The oxygen carrier is oxidized in the air reactor and is subsequently reduced in a separate fuel reactor before being recycled ("looped") back to the air reactor. By separating these two reactors and utilizing the oxidation/reduction characteristics of the oxygen carrier the gaseous oxygen in the air reactor is scavenged and then delivered as a metal oxide to the fuel reactor. By keeping the fuel and air separate a sequestration ready CO_2 stream is created in the effluent of the fuel reactor, once gaseous H_2O has been condensed and removed.

CLOU is a variant of CLC, which offers the promise of accelerating the rate of solid fuel combustion. The CLOU process also consists of two reactors − a fuel reactor and an air reactor. In the fuel reactor, solid carbonaceous fuel is burned by gaseous-phase oxygen released by the reduction of metal oxide. The reduced metal oxide is regenerated by reaction with air in the air reactor.

This topical report discusses the results of four complementary efforts: (1) the development of process and economic models to optimize important design considerations, such as oxygen carrier circulation rate, temperature, residence time; (2) the development of high-performance simulation capabilities for fluidized beds and the collection, parameter identification, and preliminary verification/uncertainty quantification; (3) the exploration of operating characteristics in the laboratory-scale bubbling bed reactor, with a focus on the oxygen carrier performance, including reactivity, oxygen carrying capacity, attrition resistance, resistance to deactivation, cost and availability; and (4) the identification of kinetic data for copper-based oxygen carriers as well as the development and analysis of supported copper oxygen carrier material.

Process and economic models. The detailed rate analysis for CLOU, utilizing reported experimental data for combustion of Mexican petcoke particles in the presence of a CuO/ZrO_2 oxygen carrier, found that the apparent activation energy for CuO decomposition reaction was 280 kJ/mol. Furthermore, the energy requirements to overcome the thermodynamic barrier for CuO decomposition are substantially larger than the kinetic barrier. The activation energy for petcoke oxidation was estimated to be 129 kJ/mol. The apparent kinetic rate constants for Cu_2O oxidation were also determined. This was achieved by applying the Law of Additive Reaction Times, which is used for analyzing the importance of porous solid reaction modulus in identifying the appropriate controlling regime (chemical reaction, internal/external mass transfer). The rate analysis of the experimental data will facilitate the pilot-scale development of CLOU process for solid carbonaceous fuels.

The kinetics of CuO reduction and petcoke oxidation determined from the rate analysis of CLOU process were utilized in developing a fluidized-bed model for the fuel reactor. The results showed a reasonable prediction of O_2 and CO_2 concentration trends with independently obtained experimental data on CLOU reported in literature.

ASPEN PLUS process models were developed for a solid-fuel based chemical-looping process development unit using a copper-based oxygen carrier for CLOU. An oxygen carrier circulation rate for CLOU of 129 kg oxygen carrier /kg coal with 40% CuO on ZrO_2 was determined based on an optimum conversion of 54% in the fuel reactor and 50% in the air reactor. The results of an ASPEN PLUS model for CLC based on the transition from Fe_2O_3 to Fe_3O_4 indicates a circulation rate of 98 kg oxygen carrier /kg coal for combustion with 60% Fe_2O_3 on Al_2O_3 oxygen carrier. The process model results for CLC underline the relevance of operating the air reactor at higher temperatures to supply energy for the endothermic metal-oxide reduction and fuel gasification reactions, as has also been suggested by other researchers. The results also indicate a larger pressure drop across the fuel reactor bed for CLC and a higher energy cost in fluidizing the particles as compared to the CLOU process for a 100 kg/hr coal feed rate (43 kW_{th} versus 5 kW_{th}) .

A relative economic analysis was performed between the CLOU process with a copper-based oxygen-carrier and CLC with an iron based oxygen-carrier. In the case of CLOU, optimizing the oxygen carrier loading is the key to take advantage of faster reaction rates for CuO to Cu_2O, which has the promise to lower the reactor volumes. Enhancing the stability of CuO-based oxygen carriers is an important variable owing to higher costs than iron-based oxygen carriers in CLC. For scaling the CLC process with iron-based oxygen carriers, the reduction of residence time in the fuel reactor is critical for future development as it impacts the energy associated with oxygen carrier fluidization and inventory.

Simulation of fluidized beds. This subtask included a sensitivity analysis for various parameters that feed into the simulation, namely CLC bed height, fluid velocity, and particle size for non-reacting CLC systems, as available from the literature. This topical report includes Computer Aided Design (CAD) and mesh details, the sensitivity analysis methodology and comparison of our simulation results with experimental results obtained from experiments conducted by Particulate Solid Research, Inc. (PSRI) in conjunction with the National Energy Technology Laboratory (NETL). The simulations are able to capture the general behavior of pressure drop profiles, as seen in the experiments. However, the non-universal character of calibration parameters, along with inherent accuracy of models, played a significant role in discrepancies between simulation and experimental results. Nonetheless, the simulations are able to capture and predict general trends related to fluidization dynamics.

Laboratory-scale studies. Oxygen carrier development is critical to the development and design of a commercial CLC system. Characteristics such as oxygen carrying capacity, reactivity, durability, attrition resistance, cost, availability, and fluidization quality are important. Of most practical interest for design of demonstration and full-scale systems is the rate of oxygen carrier oxidation and reduction as relates to temperature, conversion and gas environment. This subtask considered performance and evaluation of several copper-based CLOU carriers. The rates of carrier oxidation and oxygen liberation were evaluated under a variety of temperatures, reactor gas oxygen concentrations and degrees of conversion to quantify the influences of these variables and to develop mathematical models to describe conversion rates. Performance of the CLOU system for conversion of several solid fuels was evaluated, and the degree of oxygen carrier particle attrition was quantified.

CLC Kinetics. The spontaneous decomposition of the CuO/Cu_2O system on various support materials was investigated. Titania, alumina, sand, zirconia, celite, and silicon carbide were all screened for acceptable reactivity in multi cycle tests without fuel by thermogravimetric analysis (TGA) experiments. Silicon carbide showed the most promise as a support material based on its initial kinetic data and was investigated further. A novel method of preparing the oxygen carrier material that involves the use of rotary evaporation and multiple additions of copper was developed to improve the uniformity of the CuO deposited on the SiC support material. This also provided an oxygen carrier material that reacted faster than the material prepared by a simple wet impregnation method. While these CuO/SiC samples were successful in TGA experiments, the SiC did not have a high enough surface area to support a high load of CuO. The kinetics team then acquired and focused on β-SiC material with greater surface area, which allowed for higher CuO load capacity.

In initial TGA experiments, CuO/β-SiC material was found to be thermally unstable in oxidizing environments. In the literature, Moene et al. (1988) suggest that β-SiC calcines and converts to SiO_2 in oxidizing environments at temperatures above 800°C. The preparation method of the CuO onto the β-SiC support was altered to adapt to the new material. The modification includes calcining the β-SiC at 980°C until the material had converted to SiO_2. Samples that were first calcined and then coated with CuO performed well in TGA experiments but did not perform well in fluidized-bed experiments. Samples that were coated with CuO and then calcined showed slower rates of both oxidation and reduction in TGA experiments. Fluidized-bed experiments were satisfactory.

INTRODUCTION

CLC is a novel energy production technology currently under development. The main attraction of CLC is its ability to inherently separate oxygen from air with little energy penalty, thus allowing production of a nearly pure CO_2 stream suitable for sequestration with little additional processing. By utilizing the oxidation/reduction characteristics of a metal, or oxygen carrier, and its oxide, the oxidizing gas (typically air) and the fuel source may be kept separate. By scavenging the oxygen from the air and introducing only the metal oxide as the oxidizer to the fuel a nearly pure CO_2 effluent may be achieved. A typical CLC process schematic is presented in Figure 1.

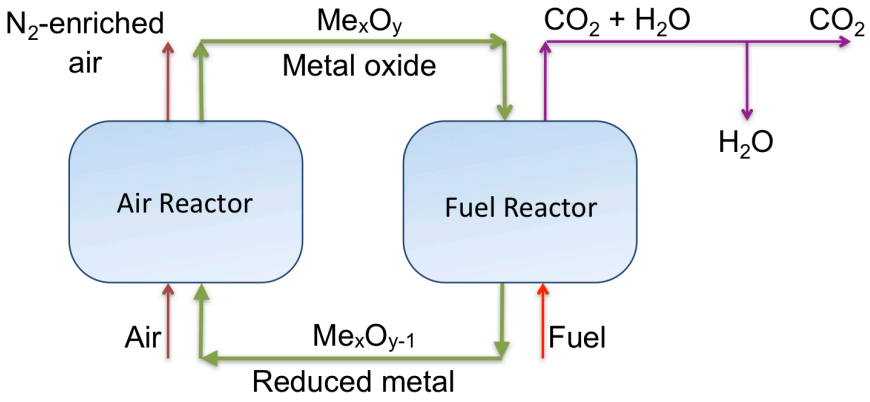

Figure 1. Schematic of CLC. A metal and its oxide are looped between the air reactor and the fuel reactor. By separating the air from the fuel a nearly pure CO_2 stream may be generated.

The key reactions for chemical looping, in general terms, are (Bergurand and Lyngfelt, 2009) reaction between the fuel and the metal oxide

$$(2n + m)Me_xO_y + C_nH_{2m} \rightarrow (2n + m)Me_xO_{y-1} + m\,H_2O + n\,CO_2$$

and the reaction between the air and the reduced metal

$$Me_xO_{y-1} + 0.5\,O_2 \rightarrow Me_xO_y$$

A schematic showing interconnection of two fluidized beds, proposed by Chalmers University in Sweden, is presented in Figure 2. The air reactor is designed as a transport reactor while the fuel reactor is designed as a bubbling fluidized bed.

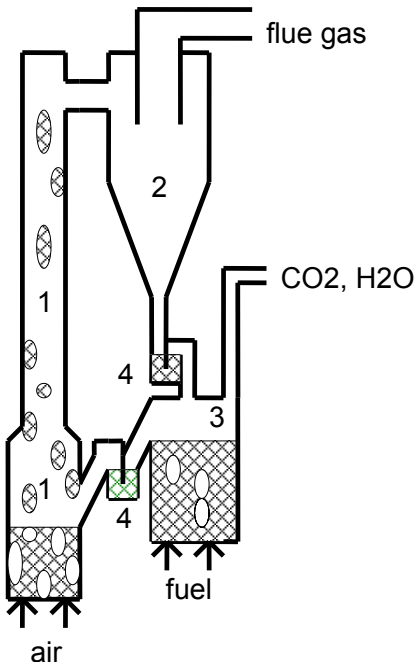

Figure 2. Design of a CLC reactor using natural gas proposed by Lyngfelt. Section 1: air reactor (AR)/riser. Section 2: cyclone to separate oxygen depleted air from the oxygen carrier. Section 3: fuel reactor (FR). Sections 4: loop seals. (Bergurand and Lyngfelt, 2009).

One particularly interesting variant of chemical looping is the so-called CLOU process. In CLOU systems, thermodynamics of the oxygen carrier are such that gaseous oxygen (O_2) is spontaneously released in the fuel reactor, which typically has low partial pressures of O_2. This allows solid fuels such as coal to be used in the fuel reactor, which greatly simplifies the CLC process. With conventional CLC, the fuel must be in gaseous form, for example natural gas or synthesis gas from coal gasification, in order to react with the solid metal oxide.

CLOU is the process of burning fuel in the presence of oxygen released by the decomposition of a metal oxide (e.g. CuO) in a fluidized-bed reactor system similar to CLC (Mattisson et al. 2009a,b). The promise offered by CLOU for facilitating CO_2 capture from solid fuels has led to the conceptualization (Eyring et al. 2011) and construction of a 150-200 kW_{th} CLOU unit (Process Development Unit or PDU) at the University of Utah, which initially will be operated for CLC (Lighty 2012, Whitty 2012). The design and fabrication of this PDU is being funded by the State of Wyoming and is not a part of this project.

METHODS

Subtask 5.1 – Process Modeling and Economics

Development of Kinetic Expressions for CLOU

The kinetic rate expressions for modeling the CLOU process were obtained from the rate analysis of reported experimental data on the CLOU combustion of Mexican Petcoke, reported in Sahir et al. (2012a).

The experimental data of Mattisson et al. (2009a,b) was analyzed to obtain the conversion versus time data for CuO decomposition, Cu_2O oxidation and C oxidation. The kinetics for the reactions occurring in the air reactor and fuel reactor of the CLOU process were subsequently obtained from the rate analysis.

The rate analysis utilizes the law of additive reaction times, whose application for CLC systems was reported by Sahir et al. (2011). The law of additive reaction times is a closed-form equation, which relates the conversion of solid reactant and time (Sohn, 1978). The law states that:

$$\begin{bmatrix}The\ time\ required\\ to\ attain\ a\ certain\\ conversion\end{bmatrix} \cong \begin{bmatrix}The\ time\ required\\ to\ attain\ the\ same\\ conversion\ under\ the\\ conditions\ of\ rapid\\ pore\\ diffusion\end{bmatrix} + \begin{bmatrix}The\ time\ required\\ to\ attain\ the\ same\\ conversion\ under\ the\\ rate\ control\ by\\ pore\\ diffusion\ and\ external\\ mass\ transfer\end{bmatrix} \begin{bmatrix}\text{Thetimerequired}\\ \text{toattainacertain}\\ \text{conversion}\end{bmatrix} \cong$$

$$\begin{bmatrix}\text{Thetimerequired}\\ \text{toattainthesame}\\ \text{conversionunderthe}\\ \text{conditionsofrapid}\\ \text{pore}\\ \text{diffusion}\end{bmatrix} + \begin{bmatrix}\text{Thetimerequired}\\ \text{toattainthesame}\\ \text{conversionunderthe}\\ \text{ratecontrolby}\\ \text{pore}\\ \text{diffusionandexternal}\\ \text{masstransfer}\end{bmatrix} \tag{5.1.1}$$

Mathematically, equation (5.1.1) is expressed as:

$$t_g^* \cong g_{F_g}(X) + \hat{\sigma}^2\left(p_{F_p}(X) + \frac{4X}{N_{Sh}{}^*}\right) \tag{5.1.2}$$

Equation (5.1.2) is a dimensionless relationship between conversion and time t_g^* expressed in terms of a conversion function for chemical reaction control, $g_{F_g}(X)$ a conversion function for pore diffusion control $p_{F_p}(X)$, a modified Sherwood Number $N_{Sh}{}^*$ and a porous solid reaction modulus $\hat{\sigma}^2$.

CuO Decomposition

The conversion versus time data for CuO decomposition was analyzed using a simplified fluidized-bed reactor, in which the solid particles are fully mixed and the gas is in a plug flow. The CuO decomposition has been analyzed by the following general form of the rate Equation (5.1.3). The effect of intra-particle diffusion and external mass transfer for CuO decomposition was investigated by applying the law of additive reaction times, and it was found that they do not have an effect on the reaction rate.

$$\frac{dX_{CuO}}{dt} = k_{CuO} f_1(p_{O_2}) f_2(X_{CuO}) \tag{5.1.3}$$

The rate of CuO decomposition was analyzed by taking into account the effect of the oxygen concentration by a function $f_1(p_{O_2})$ incorporating the equilibrium limitation for the decomposition

reaction, and a conversion function $f_2(X_{CuO})$ which considers the reaction mechanism and geometry change in solid as the reaction proceeds.

The rate analysis showed that the equilibrium limitation for the decomposition reaction, $f_1(p_{O_2})$ could be related to the enthalpy of a reaction. Thus, the temperature dependence for the CuO decomposition reaction primarily depends on two terms: the energy required to overcome the thermodynamic barrier for the CuO decomposition reaction, represented by $(-\Delta H^0)$, and the activation energy (E) to overcome the kinetic barrier.

The first-order conversion function for $f_2(X_{CuO})$ yielded a satisfactory representation of the experimental data:

$$f_2(X_{CuO}) = (1 - X_{CuO}) \tag{5.1.4}$$

The substitution of $f_1(p_{O_2})$ and $f_2(X_{CuO})$ in Equation (5.1.3) yields Equation (5.1.5)

$$\frac{dX_{CuO}}{dt} = k_{0,CuO} e^{\{-(E+\Delta H^0)/RT\}}(1 - X_{CuO}) \tag{5.1.5}$$

Cu_2O Oxidation

The law of additive reaction times was utilized to analyze the Cu_2O oxidation reaction. As structural data for grain dimensions was not available, an apparent rate constant for Cu_2O oxidation, $k_{Cu_2O,app}$ was determined by:

$$k_{Cu_2O,app} = \frac{k_g}{r_g} \tag{5.1.6}$$

The dimensionless time, t_g^*, in this case is defined as:

$$t_g^* = \frac{b k_{Cu_2O,app}}{\tilde{\rho}_{S,Cu_2O}} \overline{\left[\frac{p_{O_2}}{RT} - \frac{p_{O_2}^e}{RT}\right]_{avg}} \, t \tag{5.1.7}$$

$$\text{where } \left[\frac{p_{O_2}}{RT} - \frac{p_{O_2}^e}{RT}\right]_{avg} = \left[\left[\frac{p_{O_{2,in}}}{RT_{avg}} - \frac{p_{O_2}^e}{RT_{avg}}\right] + \left[\frac{p_{O_{2,out}}}{RT_{avg}} - \frac{p_{O_2}^e}{RT_{avg}}\right]\right]/2 \tag{5.1.8}$$

An average $\overline{\left[\frac{p_{O_2}}{RT} - \frac{p_{O_2}^e}{RT}\right]_{avg}}$ of the arithmetic mean of the measurements of the driving force due to the variation in oxygen concentration driving force $\left[\frac{p_{O_2}}{RT} - \frac{p_{O_2}^e}{RT}\right]_{avg}$ was evaluated with the help of reported experimental data of Mattisson et al. (2009a,b) for measured bed temperature, inlet O_2 concentration and measured exit O_2 concentration of 10% at 900°C and 950°C.

The choice of a spherical geometry for a grain was made after applying the conversion function for chemical reaction to various geometries, and identifying a suitable fit to the experimental data.

The conversion function for chemical reaction for a spherical grain is provided by Equation (5.1.9).

$$g_{F_g}(X) = 1 - (1 - X)^{1/3} \tag{5.1.9}$$

The conversion function for gas diffusion through pores for a spherical particle is provided by Equation (5.1.10).

$$p_{F_p}(X) = 1 - 3(1 - X)^{2/3} + 2(1 - X) \tag{5.1.10}$$

Applying the Equations (5.1.6-5.1.9) to Equation (5.1.2), Equation (5.1.11) can be formulated to represent the Cu_2O oxidation process as:

$$t \cong \left[\left(\frac{RT_{avg}\alpha_S\tilde{\rho}_{S,Cu_2O}}{2k_{Cu_2O,app}(p_{O_2} - p^e_{O_2})_{avg}}\right)\{1 - (1 - X)^{1/3}\}\right] + \left[\left(\frac{RT_{avg}\alpha_S\tilde{\rho}_{S,Cu_2O}r_p^2}{12D_e(p_{O_2} - p^e_{O_2})_{avg}}\right)\{1 - 3(1 - X)^{2/3} + 2(1 - X)\}\right] + \left[\left(\frac{RT_{avg}\alpha_S\tilde{\rho}_{S,Cu_2O}r_p^2}{3D_M N_{Sh}(p_{O_2} - p^e_{O_2})_{avg}}\right)X\right] \tag{5.1.11}$$

Mexican Petcoke Oxidation

The global reaction rate constant for petcoke oxidation was obtained by fitting the value of $k_{r,C}$ to the shrinking-sphere equation with a half-order dependence on partial pressure of oxygen (Hurt and Mitchell, 1992).

$$\frac{dr_C}{dt} = -\frac{k_{r,C}}{\rho_C} p^{1/2}_{O_2,avg} \tag{5.1.12}$$

The value of $p^{1/2}_{O_2,avg}$ was calculated by the following relation,

$$p^{1/2}_{O_2,avg} = \frac{p^{1/2}_{O_2,in} + p^{1/2}_{O_2,out}}{2} = \frac{p^{1/2}_{O_2,out}}{2} \quad , (\text{as } p_{O_2,in} = 0) \tag{5.1.13}$$

Development of a Custom Model for CLOU

The development of a custom model for CLOU was pursued by analyzing the fuel reactor stage in the batch fluidized-bed reactor experiment. In this stage, the fuel particles are introduced in the reactor and the combustion process is modeled. The CuO decomposition reaction to release oxygen and carbon oxidation reaction occur simultaneously. The oxygen concentration changes with respect to time and height. The following assumptions were made for modeling the experimental bench-scale CLOU batch

fluidized-bed reactor of Mattisson et al. (2009a,b):

- The solids are considered to be well mixed in the reactor.
- The gases (oxygen and carbon dioxide) are present in the emulsion and the bubble phase, and the process of interchange of gases occurs between the two phases.
- The solids are only in the emulsion phase, and the CuO decomposition and petcoke oxidation reactions occur in it.

Material balance equations were formulated for the bubble and emulsion phase for O_2 and CO_2

gases as represented by equations (5.1.14-5.1.17).

Bubble phase for oxygen:

$$\frac{f_{g,b}}{RT}\frac{\partial p_{O_2}{}^{bbl}}{\partial t} = \frac{f_{g,b}u_b}{RT}\frac{\partial p_{O_2}{}^{bbl}}{\partial z} + \frac{\delta K_{BE}}{RT}\left(p_{O_2}{}^{em} - p_{O_2}{}^{bbl}\right) \quad (5.1.14)$$

Emulsion phase for oxygen:

$$\frac{f_{g,e}}{RT}\frac{\partial p_{O_2}{}^{em}}{\partial t} = \frac{f_{g,e}u_e}{RT}\frac{\partial p_{O_2}{}^{em}}{\partial z} + \frac{\delta K_{BE}}{RT}\left(p_{O_2}{}^{bbl} - p_{O_2}{}^{em}\right) + \left(\frac{1}{4}\right)\frac{n_{CuO}(-r_{CuO})}{V_R} - \frac{n_C(-r_C)}{V_R} \quad (5.1.15)$$

Emulsion phase for carbon dioxide:

$$\frac{f_{g,e}}{RT}\frac{\partial p_{CO_2}{}^{em}}{\partial t} = \frac{f_{g,e}u_e}{RT}\frac{\partial p_{CO_2}{}^{em}}{\partial z} + \frac{\delta K_{BE}}{RT}\left(p_{CO_2}{}^{bbl} - p_{CO_2}{}^{em}\right) + \frac{n_C(-r_C)}{V_R} \quad (5.1.16)$$

Bubble phase for carbon dioxide:

$$\frac{f_{g,b}}{RT}\frac{\partial p_{CO_2}{}^{bbl}}{\partial t} = \frac{f_{g,b}u_b}{RT}\frac{\partial p_{CO_2}{}^{bbl}}{\partial z} + \frac{\delta K_{BE}}{RT}\left(p_{CO_2}{}^{em} - p_{CO_2}{}^{bbl}\right) \quad (5.1.17)$$

Table 1 lists the reactor dimensions and the particle properties utilized in the development of the model.

Table 1. Reactor dimensions (Mattisson et al. 2009 a).

Parameter	Value
Diameter of the fluidized bed, D_T	22 mm
Superficial Velocity, u_0	0.16 m/s
Temperature range of experiments, T	885-985°C
Density of CuO/ZrO_2 particle,ρ_S	2.145 g/cm^3
Average diameter of CuO/ZrO_2 particle (Size Range = 125-180 μm),d_p	152.5 μm
Density of fuel particle, ρ_C	1.02 g/cm^3
Average diameter of fuel particle(Size Range = 180-250 μm), d_C	215 μm

Table 2 lists the semi-empirical correlations utilized in the model for characterizing the batch fluidized-bed reactor. In this study, a design approximation proposed by Zenz (1978) was used to estimate the variation of bubble diameter with height in a bench-scale batch fluidized-bed (2.2 cm). The initial bubble size was estimated using the correlation reported by Mori and Wen (1975).

Table 2. Semi-empirical correlations and design relationships utilized for modeling.

Parameter	Semi-empirical correlation or design relationship
Minimum Fluidization Velocity (in m/s): u_{mf} (Richardson and Jeronimo, 1979)	$u_{mf} = \left(\frac{\mu}{d_p \rho_g}\right)\left[\left[(25.7)^2 + \left\{0.0365\left(\frac{d_p^3 \rho_g (\rho_S - \rho_g) g}{\mu^2}\right)\right\}\right]^{1/2} - 25.7\right]$
Voidage at minimum fluidization, ε_{mf}	0.427 (assuming that particles are spherical)
Rise velocity of emulsion through the bed: u_e (Kunii and Levenspiel, 1991)	$u_e = \left(\frac{u_{mf}}{\varepsilon_{mf}}\right) - \frac{\alpha \delta u_b}{(1 - \delta - \alpha\delta)}$
Fraction of bed volume occupied by bubbles: δ (Puettmann et al. 2012)	$\delta = 0.8\frac{(u_0 - u_{mf})}{u_b}$
Interchange coefficient for gas between bubble and emulsion phases based on bubble volume (1/s): K_{BE} (Sit and Grace, 1981)	$K_{BE} = 2\left(\frac{u_{mf}}{d_b}\right) + 12\left(\frac{\left(\mathcal{D}\varepsilon_{mf} u_b\right)^{1/2}}{\pi {d_b}^{3/2}}\right)$
Bubble diameter above porous plate distributor: d_{b0} (in cm.) (Mori and Wen,1975)	$d_{b0} = 0.00376\,(u_0 - u_{mf})^2$
Bubble diameter at a height h: d_b(in cm.) (Zenz, 1978)	$\left(\frac{d_b}{d_{bi}}\right) = 0.15\left(\frac{h}{d_{bi}}\right) + 0.85$
Bubble velocity(cm/s): u_b (Puettmann et al. 2012)	$u_b = 0.8(u_0 - u_{mf}) + (0.71)(1.18)(g d_b)^{0.5}$
Ratio of height of fluidized bed and height of minimum fluidized bed $\left(\frac{L_f}{L_{mf}}\right)$; (Babu et al. 1978)	$\frac{L_f}{L_{mf}} = 1 + \frac{0.762(u_0 - u_{mf})^{0.57} \rho_g^{0.083}}{\rho_s^{0.166} u_{mf}^{0.063} D_T^{0.445}}$
Fraction of fluidized bed volume occupied by gas in the emulsion , $f_{g,e}$	$f_{g,e} = (1 - \delta - \alpha\delta)\varepsilon_{mf}$
Fraction of fluidized bed volume occupied by gas in the bubble, $f_{g,b}$	$f_{g,b} = \delta(1 + \alpha\varepsilon_{mf})$

Development of ASPEN PLUS Process Models for CLOU and CLC

An ASPEN PLUS process model for the CLOU process was developed to evaluate material and energy balance scenarios. The purpose of these process models is to investigate options to support the development of a PDU at the University of Utah, which will be operated on PRB coal as an initial fuel. The scenarios for a PDU for CLOU employing a copper-based oxygen carrier and CLC employing an iron-based oxygen carrier were compared from a viewpoint of carbon capture.

In the ASPEN PLUS model, the mass flow rates of the inlet metal oxide stream to the fuel reactor and the outlet metal oxide stream from the air reactor model are equated to accomplish recirculation of metal oxide for chemical-looping combustion systems (CLOU or CLC) discussed in this report. The coal feed rate is 100 kg/h.

Table 3 and Table 4 represent the proximate and ultimate analysis of Wyoming PRB, Illinois#6 and Colombian coal.

Table 3. Proximate Analysis for fuels used for comparison (wt. %).

Coal	Moisture	Volatile Matter	Ash
Wyoming PRB (Sub-Bituminous)	23.7	49.8	6.5
Colombian Coal (Bituminous)	3.3	37.0	5.2
Illinois #6 (Bituminous)	6.7	39.4	10.4

Table 4. Ultimate Analysis for fuels used for comparison.

Coal	C(wt % d.a.f)	H (wt% d.a.f)	O(wt % d.a.f)	N(wt % d.a.f)	S(wt% d.a.f)	Heating Value (MJ/kg)
Wyoming PRB	75.3	5.0	18.3	1.1	0.3	27.7(dry basis)
Colombian Coal	80.7	5.5	11.5	1.5	0.6	29.1
Illinois#6 Coal	75.3	5.3	13.0	1.6	4.8	27.4 (dry basis)

d.a.f.: dry and ash-free

ASPEN PLUS Process Model for CLOU using a Copper-Based Oxygen Carrier

CuO decomposition and Cu_2O oxidation rate equations obtained from experimental data on CLOU combustion in a batch fluidized-bed (Mattisson et al. 2009a,b) were employed to determine the required conversion of CuO in the fuel reactor and Cu_2O in the air reactor (Sahir et al. 2012a). The oxygen carrier particles employed in the CLOU experiment were 40% CuO supported on ZrO_2 in the size range of 125-180 μm and were used for evaluating material and energy balances for the CLOU process. The kinetic data for the PRB coal char combustion was utilized for determining the char burnout times (Bartok and Sarofim, 1991).

The rate equations were employed to evaluate the residence times, which were consequently used to determine the mass of copper metal loading for both air and fuel reactors as a function of the mole ratio of CuO at the exit of the fuel reactor $X_{CuO,FR}$, and the difference of mole ratio between the air and fuel reactors, ΔX_S. The methodology and the derivation are detailed in Eyring et al. (2011). The results in Figure 3 indicate a minimum copper metal loading for both fuel and air reactor of 127 kg Cu/MW_{th} fuel (or 159 kg CuO/ MW_{th} fuel) for a $X_{CuO,FR}$ of 0.3 and ΔX_S of 0.35. The mole ratio of CuO at the exit of the fuel reactor, $X_{CuO,FR}$ of 0.3 and a difference in mole ratio ΔX_S of 0.35 translates to a stoichiometric conversion of 54% in the fuel reactor and 50% in the air reactor. The residence time in the fuel reactor is 35 seconds and in the air reactor is 42 seconds for the CLOU process, at these process conditions.

A plot of residence time with respect to temperature is shown in Figure 4. The time for a 54% reduction of CuO in the presence of fuel particles decreases with an increase in temperature from 138 seconds at 900°C to 19 seconds at 985 °C. However, in the air reactor, the time required to attain 50% conversion, with air as a reactant for Cu_2O oxidation, increases with increasing temperature, ranging from 30 seconds at 885°C to 132 seconds at 985°C. The air flow rate was established by considering a design outlet oxygen concentration of 5%, which corresponds to approximately 25% excess air and keeps the exhaust gas higher than the partial pressure of O_2 in a CuO-Cu_2O system at 935°C (~0.032 atm.) The coal char burnout occurs within approximately ten seconds. A temperature range of 920°C to 960°C was identified as a probable range of operation for CLOU where residence times for reactors are less than 100 seconds with a suitable energy differential represented by a 15°C temperature difference. The details of the analysis can be found in Sahir et al. (2012b).

Figure 5 represents a schematic of the ASPEN PLUS model developed for analyzing the CLOU process. The solid fuel combustion process is modeled with the combination of RYIELD and RGIBBS reactor models. The role of the RYIELD reactor is to decompose coal into its constituent elements, and the equilibrium reactor (RGIBBS) generates the synthesis gas at 950°C from the constituent elements. The oxygen for combusting coal is supplied by a stoichiometric reactor (RSTOIC) with a specified CuO conversion of 54%. The flue gas containing CO_2 and H_2O was cooled and re-circulated in the fuel reactor to fluidize the bed. The amount of CuO required for combustion takes into account a design factor of 15% excess oxygen in the fuel reactor. The air reactor was modeled with a Cu_2O conversion of 50% in the RSTOIC process model block, to regenerate the Cu_2O formed after CuO decomposition.

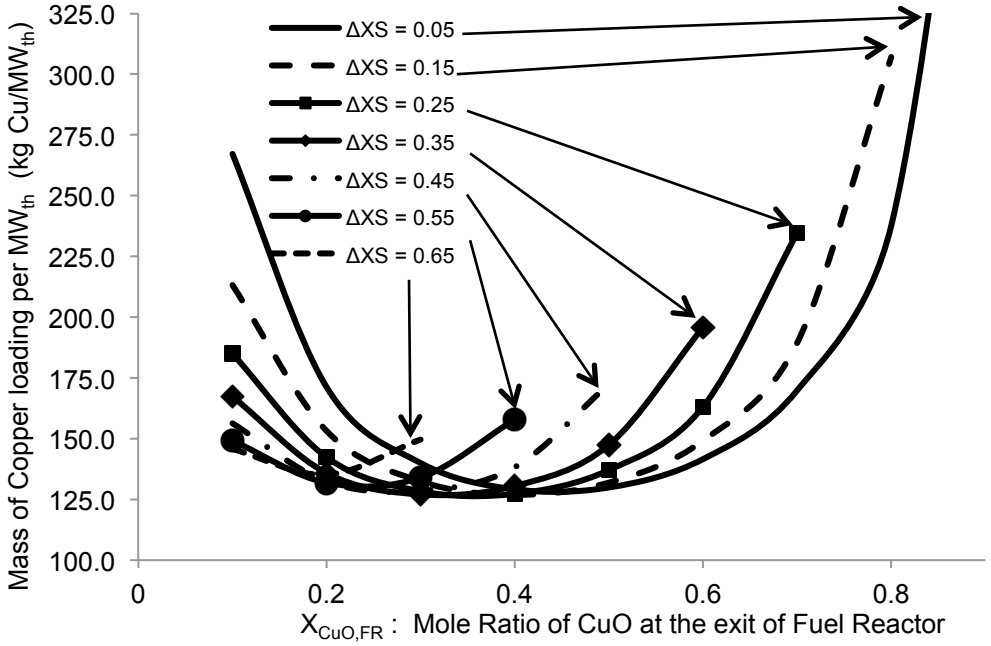

Figure 3. Mass of copper loading per MW_{th} vs mole ratio of CuO at the exit of fuel reactor for different values of ΔX_S.

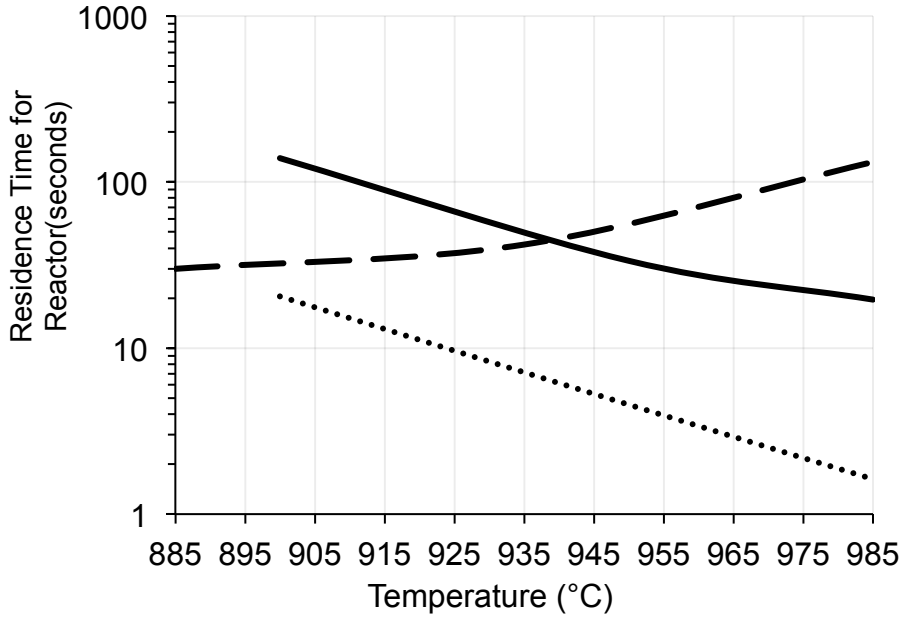

Figure 4. Residence time in a reactor (on logarithmic scale) versus temperature (─ CuO reduction, - - Cu_2O Oxidation, •• PRB coal char burnout).

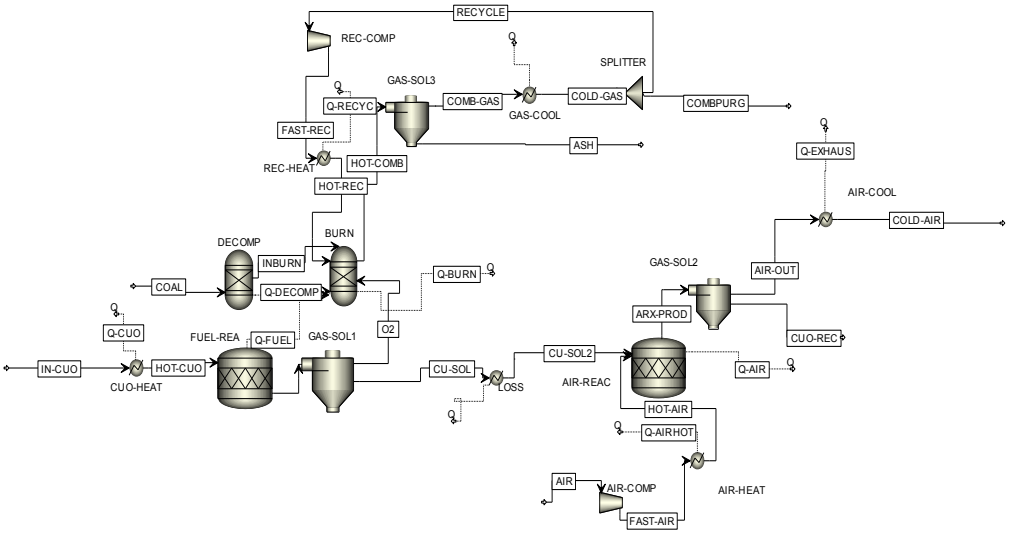

Figure 5. Schematic of ASPEN PLUS process model for CLOU with CuO-ZrO_2 as an oxygen carrier.

ASPEN PLUS Process Model for CLC Using an Iron-Based Oxygen Carrier

Oxygen carrier particles of Fe_2O_3 supported on Al_2O_3 were used for analyzing material and energy balance scenarios for the CLC process with PRB coal. To represent the fuel reactor in ASPEN PLUS, the coal is fed to the gasifier and then the resulting syngas reacts with the circulating oxygen carrier. The approach of modeling the fuel reactor as a series of reactors in ASPEN PLUS does not imply that a physical system would be built along similar lines.

The following reactions take place between syngas and the circulating metal oxide in the fuel reactor:

$$3Fe_2O_3\,(s) + CO\,(g) \rightarrow 2Fe_3O_4\,(s) + CO_2\,(g) \qquad (5.1.18)$$

$$3Fe_2O_3\,(s) + H_2\,(g) \rightarrow 2Fe_3O_4\,(s) + H_2O\,(g) \qquad (5.1.19)$$

The conversion of CO and H_2 is almost complete when Fe_2O_3 is converted to Fe_3O_4 with an equilibrium concentration of $CO/(CO_2 + CO) \sim 0.005\%$ and that of $H_2/(H_2 + H_2O) \sim 0.003\%$ at 900 °C (Xue et al. 2012). In this report, Al_2O_3 was considered as an inert to facilitate order of magnitude calculations, although the significance of the reaction of iron and Al_2O_3 through the formation of hercynite ($FeAl_2O_4$) has been demonstrated (Abad et al. 2007b, Kidambi et al. 2011).

In the air reactor, the oxidation reaction occurs by the following pathway:

$$2Fe_3O_4\,(s) + 1/2\,O_2(g) \rightarrow 3Fe_2O_3\,(s) \qquad (5.1.20)$$

The results of batch fluidized-bed oxidation experiments on natural hematite (α-Fe_2O_3) particles sized between 0.180 and 0.250 mm at 950°C indicate a high oxidation rate of 90% min^{-1} (Mattisson et al. 2001). Abad et al. (2007a) investigated the oxidation of 0.15 mm particles of 60% Fe_2O_3 supported on Al_2O_3

with 15% O_2. .Their results show that 80% oxidation was achieved in less than 10 seconds at 950°C in experiments conducted on a thermobalance. These studies were used to form a design basis for the CLC air reactor described subsequently.

An estimate of the gasification kinetics for the PRB coal was derived through comparisons with two coals, a Colombian coal and an Illinois #6 bituminous coal. The Colombian coal was recently tested in the 100 kW_{th} unit using ilmenite as an oxygen carrier at Chalmers (Markström et al. 2013a, b). The properties of the coals can be found in Table 3 and Table 4, which suggest that the Colombian and Illinois #6 coals are similar. In addition, experimental studies on entrained-flow gasification showed that the relative reactivity of a Wyoming PRB coal char was 1.17 times greater than that for Illinois #6. The findings in this report are based on the kinetic data from the Colombian coal, which is likely to be conservative in terms of gasification rates.

Leion et al. (2009) reported a rate of 9.6% min^{-1} at 970°C for 95% conversion for Colombian coal in CLC fluidized-bed experiments with Fe-based ilmenite as an oxygen carrier. Abad et al. (2007b) have reported syngas reduction rates of 8-30% min^{-1} for Fe_2O_3 supported on Al_2O_3 oxygen carriers. As the coal gasification reaction takes a longer time than the syngas reduction reaction, the fuel reactor was designed considering the coal gasification reaction as a rate-limiting step. Cuadrat et al. (2012) reported longer char conversion times in the presence of H_2O in TGA experiments. A residence time of 10 minutes was employed for designing the CLC fuel reactor, based on average literature values. Thus, the material and energy balance evaluation presented in the report, is a conservative estimate of the amount of oxygen-carrier material needed for the CLC process.

A preliminary estimate for an oxygen carrier inventory of 2000 kg/MW_{th} for CLC with petroleum coke with a 60% Fe_2O_3 supported on 40% inert $MgAl_2O_4$ as an oxygen carrier was reported by Leion et al., (2007). Their estimate for the oxygen carrier inventory is based on a fuel reactor residence time of 5 minutes, which could be achieved if the fuel conversion is conducted with steam, and accomplished with separation and recycling of significant amount of un-reacted char. The analysis conducted in this report uses a fuel reactor residence time of 10 minutes, based on experimental observation in batch fluidized-bed experiments (Leion et al., 2009). As more operational experience is gathered with CLC experiments with solid fuels on Fe_2O_3 based oxygen carriers in continuous units, this design assumption could be modified.

The CLC process with 60% Fe_2O_3 supported on Al_2O_3 was modeled in ASPEN PLUS to generate the material and energy balances. The process model flow sheet showing the various process model blocks is shown in Figure 6.

Fuel Reactor – The fuel reactor material and energy balances for the CLC process is handled in ASPEN PLUS by three process model blocks. The gasification process is modeled by a combination of RYIELD reactor with an equilibrium reactor (RGIBBS). Steam is used as an inlet stream, with a steam/carbon mole ratio of unity for the process model. The role of the RYIELD reactor is to decompose coal into its constituent elements, and the equilibrium reactor (RGIBBS) generates the synthesis gas from the constituent elements. The composition of the syngas at the outlet of the gasifier operating at 950°C, consists of 31.8% CO, 5.2% CO_2, 50.2% H_2 and 12.5% H_2O. A stoichiometric reactor (RSTOIC) then

converts the syngas to CO_2 and H_2O with a ~99.9% conversion of Fe_2O_3 to Fe_3O_4. The energy associated with the fuel reactor is evaluated by adding the contributions of RYIELD, RGIBBS and RSTOIC blocks.

Air Reactor – A stoichiometric reactor (RSTOIC) with an 80% conversion of Fe_3O_4 to Fe_2O_3, and a residence time of 90 seconds was used for the oxidation reaction of oxygen carrier in the air reactor. This is a conservative estimate for process design of CLC air reactor in light of the experimental studies on oxidation conducted on a batch-fluidized bed (Mattisson et al. 2001) and a thermobalance (Abad et al.2007a). The incomplete conversion of Fe_3O_4 in the air reactor requires 20% more material to be circulated than in the fuel reactor.

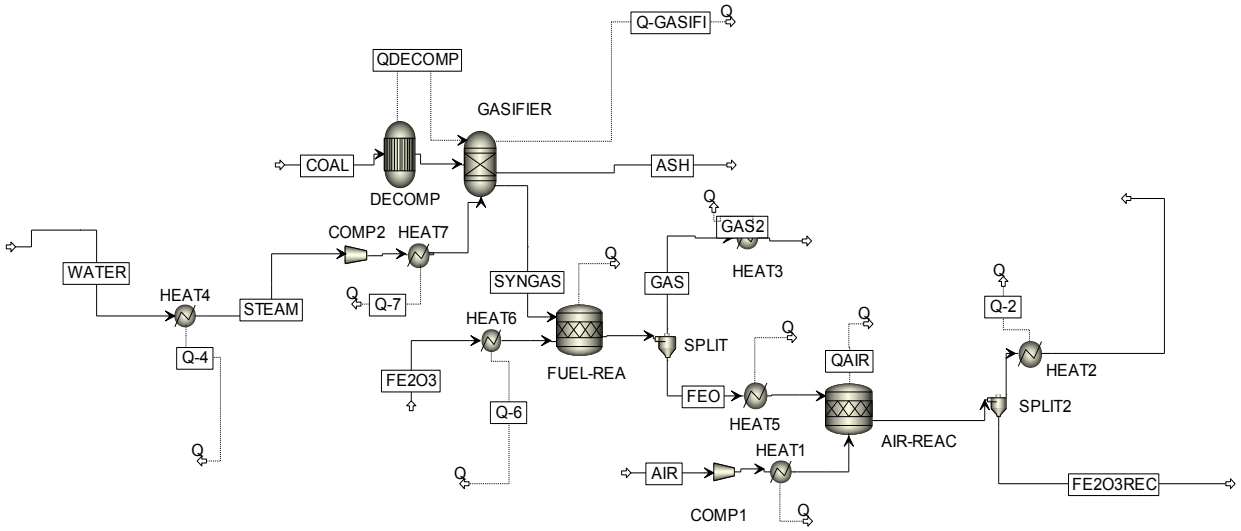

Figure 6. Schematic of ASPEN PLUS process model for CLC with Fe_2O_3-Al_2O_3 as an oxygen carrier.

Relative Economic Comparison between CLC and CLOU

Using the PDU as a basis, a relative economic comparison of the CLC and CLOU processes was performed at several scales (1, 10 and 100 MW_{th}, which was achieved by adjusting the coal thermal input). While the actual costs and the energy recovery strategy from the fuel and air reactors for CLC and CLOU are most likely different, the results are presented on a relative basis and are intended for comparison purposes. The assumptions include:

1. The air and fuel reactors were circulating fluidized-beds (CFB) with a bed voidage of 0.6. Both have a circular cross section.
2. A 3 MW/m^2 thermal energy per unit cross section area was used (Basu and Fraser, 1991).
3. A gas residence time of 2 seconds was considered based on design data from other laboratory-scale units (Fan, 2010), where velocities were calculated by the correlations utilized for CFB coal combustor designs. The superficial velocity was corrected by a factor of 2, as the core velocity may exceed greater than 50% (Basu and Fraser, 1991).
4. The cost of compressors includes the cost of equipment required to fluidize the oxygen carrier and fuel particles in the reactor vessels. The cost of compression required for CO_2 sequestration was not incorporated.

5. The number of process trains required for a particular energy output was based on the design principles for CFB coal combustors, namely heights in the range of 15-20 m with a bed depth not exceeding 5 m, and heights 20-30 m with a depth of 7.5 m (Basu and Fraser, 1991). If the height exceeded 15 m and the diameter exceeded 5 m, then the process was split into two trains. Table 5 represents the correlations utilized to perform the economic analysis.

Table 5. Correlations and relationships **used** to perform relative economic analysis**.**

Cost of copper-based oxygen carrier (Leion and Lighty, 2013)	€5000 per metric ton
Cost of iron-based oxygen carrier (Leion and Lighty, 2013)	€150 per metric ton
Attrition Rate of Carrier (Adanez et al. 2012)	0.05% per hour
Cost of electricity (Towler and Sinnott, 2007)	US$0.06 per kWh
Compressor Work, W (in kW) (Lyngfelt et al. 2001)	$W = \frac{n}{(n-1)} \frac{p_{inlet} v_{inlet} \dot{m}_{inlet}}{\eta_{fan}} \left[\left[\frac{p_{inlet} + \Delta p}{p_{inlet}} \right]^{(n-1)/n} - 1 \right]$
Capital Cost of Centrifugal Compressor (Towler and Sinnott, 2007)	580000+(20000*$W^{0.6}$)
Capital Cost of Cyclone (Mantripragada and Rubin, 2012)	0.05*(Capital Cost of the reactors)
Capital Cost of Reactor in US$ million (2000) per process train (Mantripragada and Rubin, 2012)	$16.15 \left(\frac{V_R}{180\ m^3} \right)^{0.6}$
Chemical Engineering Plant Cost Index for 2000 (Towler and Sinnott, 2007)	394.1
Chemical Engineering Plant Cost Index for 2010 (Chemical Engineering, 2012)	550.8

Subtask 5.2 – LES-DQMOM Simulation of a Pilot-Scale Fluidized Bed

Simulation of multiphase systems still presents a challenge in terms of representation of transport (diffusive and convective), mixing, mass transfer, chemical reactions and interaction of the dispersed phase. At this time, Large Eddy Simulation (LES) tools for multiphase systems are not sufficiently developed to represent the entire spectrum of phenomena necessary to describe a CLC system. Consequently our simulations use Reynolds-Averaged Navier-Stokes (RANS) equations to describe the gas phase, coupled with a laminar representation with kinetic theory-based closures for the dispersed phase. Although this is a common practice for monodisperse cases (only one particle size), several approaches are available for polydisperse mixtures. In particular, our simulations use Direct Quadrature Method of Moments (DQMOM) to describe polydispersity.

Dispersed-phase scalar characteristics such as size, composition, temperature, can be accounted for with the solution of a population balance equation. The population balance equation (PBE) describes the evolution of the number density function (NDF). NDF contains all possible information about the particle phase, since it represents an unequivocal description of particle properties distribution. A PBE for the NDF is represented by equation ((5.2.1):

$$\frac{\partial \mathrm{f}(\xi, \mathrm{u_p}; \mathrm{x}, \mathrm{t})}{\partial \mathrm{t}} + \frac{\partial \left[\mathrm{u}_{ip} \mathrm{f}(\xi, \mathrm{u_p}; \mathrm{x}, \mathrm{t})\right]}{\partial x_i} + \frac{\partial \left[\mathrm{F}_i \mathrm{f}(\xi, \mathrm{u_p}; \mathrm{x}, \mathrm{t})\right]}{\partial \mathrm{u}_{ip}} + \frac{\partial \left[\mathrm{G}_i \mathrm{f}(\xi, \mathrm{u_p}; \mathrm{x}, \mathrm{t})\right]}{\partial \xi_i} = \mathrm{h}(\xi, \mathrm{u_p}; \mathrm{x}, \mathrm{t}) \qquad (5.2.1)$$

Here, $\mathrm{f}(\xi, \mathrm{u_p}; \mathrm{x},\mathrm{t})$ is the NDF, ξ is a particular particle characteristic (e.g. size, temperature, or mass), u_i is the velocity of the disperse phase, F_i are the body forces over the disperse phase including gravity, G_i is the convection of the NDF in particle phase space, and $\mathrm{h}(\xi, \mathrm{u_p}; \mathrm{x}, \mathrm{t})$ is the collision term that accounts for the disperse phase interactions.

Modeling and simulation of the NDF through the use of PBE requires full discretization of the particle phase space, which, usually, is a highly dimensional space. Although full particle phase space discretization allows reconstructing the particle property distribution, it is expensive and is not suitable for Computational Fluid Dynamics (CFD) codes, in which variables are usually dependent on space and time only. Instead, the statistics (integer moments) of the NDF are meaningful enough to be used as field variables (variables that depend only on space and time) and to physically explain the behavior of the multiphase system.

The NDF can be approximated using delta Dirac functions:

$$f(\xi, \mathrm{u_p}; \mathrm{x}, t) = \sum_{\alpha=1}^{N} \omega_\alpha(\mathrm{x}, t)\delta\left[\xi - \xi_\alpha(\mathrm{x}, t)\right]\delta[\mathrm{u_p} - \mathrm{u_{p\alpha}}(\mathrm{x}, t)] \qquad (5.2.2)$$

in which $\omega_\alpha(\mathrm{x},t)$ are the weights of the delta function located at the characteristic velocity $\mathrm{u_{p\alpha}}(\mathrm{x},t)$ and at the particular particle scalar characteristic $\xi_\alpha(\mathrm{x},t)$. Replacing equation (5.2.2) and applying the moment transformation we obtain transport equations for the moments, equation (3), which reduce the high dimensionality of population balance equations to field variables that can be implemented in CFD codes.

$$M(i,j) = \int_{-\infty}^{\infty}\int_{0}^{\infty} \mathrm{u}_p^i \xi^j f\left(\xi, \mathrm{u_p}; \mathrm{x}, t\right) d\mathrm{u}_p d\xi \tag{5.2.3}$$

Based on the implementation of polydispersity, following the DQMOM technique, the investigators performed a sensitivity analysis to study effects of different particle sizes in the fluid dynamic behavior of the bed. They included effects of velocity and height in the analysis. The commercially available software, STAR-CCM+, was used in the simulations, and the results were compared to experimental data obtained by PSRI and NETL for the bubbling fluidized bed (BFB) reactor.

Kinetic Theory of Granular Flows

In order to simulate a multiphase system, it is necessary to account for the conservation equations describing the characteristics of the different phases involved. Generally, in multiphase systems, one phase is the continuous phase and other phases are the dispersed phases. Continuous and dispersed phases use an Eulerian description as the conservation equations. These descriptions assume that both phases coexist at the same location and occupy their respective portions of any specific volume. The ratio of volume occupancy is called volume fraction. The volume fraction appears in all transport equations for all phases as a main variable, since it essentially describes all the participating phases in the system.

Conservation equations require phase interaction terms that couple all phase phenomena at the phase interface (mass, momentum and heat transfer). These terms need closure terms that characterize different multiphase flow patterns; however, these terms are often not known. Furthermore, in cold-flow fluidized bed modeling, one of the main momentum interaction terms is the drag force. There are two kinds of drag force: the first kind is due to the continuous phase and second kind is due to the dispersed phase. The continuous drag force calculates force on a particle due to its velocity relative to the continuous phase. Analogously, the dispersed drag coefficient calculates the force due to its velocity relative to the disperse phase.

The kinetic theory of granular flows provides the framework to describe the particle-particle interactions in gas-solid systems when particles are in close proximity and when particles are freely moving with the fluid. For particles in close packing state, the motion is contact-dominated and the granular pressure model estimates the stresses of the solid phase based on a simplified version of the critical state theory. (Johnson, 1987) The stress tensor can be represented as:

$$\mathrm{F_{int,p}} = \nabla \cdot \overline{\mathrm{S_p}}$$

where the granular stress is defined as:

$$\overline{S_p} = \left[-P_p + \left(\xi_p - \frac{2}{3}\mu_p\right)\nabla \cdot u_p\right] I$$

where P_p is the solid pressure, μ_p the effective granular viscosity I and is the identity tensor.

For particles below the packing limit, moving freely with the fluid, and interacting with other particles, the motion is collision-dominated, and the granular temperature model calculates the collisions and the motion of particles in this regime. This quantity is a measure of the fluctuating kinetic energy of the particles:

$$\theta_p = \frac{1}{3}\langle v'_{pi} \cdot v'_{pi}\rangle$$

where v'_{pi} is the random fluctuating velocity of the particle phase and $\langle\cdot\rangle$ denotes ensemble averaging. In order to obtain the kinetic energy of particles, transport equations for θ_p are necessary, along with the information provided by equation for $\overline{S_p}$ and θ_p. Other particle properties can be calculated based on hypothesis analogous to the kinetic theory of gases.

Modeling Approach

Our original modeling effort was concentrated on performing simulations using the Large Eddy Simulation (LES) models. However, for the modeling framework approach, several difficulties surfaced when coupling the LES gas turbulence models available in STAR-CCM+ with the Kinetic Theory of Granular Flows (KTGF) for the description of the solid phase. For general multiphase flows, this coupling is already available for laminar and Reynolds-Averaged Navier-Stokes equations (RANS) models. STAR-CCM+ still uses critical assumptions regarding the turbulence in these kinds of systems, such as that the turbulence in the solid phase is represented by the random fluctuations of the granular temperature and the gas phase is taken as a laminar flow represented by the Navier-Stokes equations. To correct for this effect, other assumptions in the transport equations for the particle phase are necessary (CD-adapco 2013). Using STAR-CCM+ User Code capabilities, which were used to implement the solid-phase models, we have tried to account and implement assumptions appropriate for coupling LES with KTGF. However, given that STAR-CCM+ is a commercial software, only a limited set of tools were available, which, ultimately, did not allow for implementation of the necessary changes. Therefore, the solids modeling capabilities relied on the already existing framework inside STAR-CCM+, namely the RANS models.

There are many aspects that need to be considered when simulating fluidization systems. The predictive accuracy of simulations depends on the accuracy of modeling approaches. Our simulations used Gidaspow's (Bouillard et al. 1989) drag with a linearized drag coefficient, which reduces to the Wen and Yu model when the volume fraction is approaching one.

The particle dynamics in a fluidized bed requires description for two types of regimes. The first regime is the kinetic regime, which is characterized by frequent particle collisions. The theory to describe this

regime is analogous to the kinetic theory of gases, where an assumption on the velocity distribution is necessary to calculate particle properties. (Lun et al. 1984) The second, frictional, regime is needed to describe particle dynamics. This regime is dominated by particle contact. This type of dynamics is described by semi-empirical models. (Schaeffer 1987), (Johnson 1987) These two approaches combined account for the solids stresses necessary to describe the motion in the solids momentum equations.

Previously, we have briefly outlined some generalities of PBEs from which DQMOM transport equations can be derived, namely using equations (5.2.1) through (5.2.3). To further reduce the dimensionality of the NDF approximation, we use size-conditioned velocity (Fan et al. 2004), which allows using a momentum equation for the solid phase obtained from a regular Eulerian multiphase model. With the use of size-conditioned velocity approximation, equation (5.2.2) can be written as:

$$\bar{f}(\xi; \mathrm{x}, t) = \sum_{\alpha=1}^{N} \omega_\alpha(\mathrm{x}, t)\delta\left[\xi - \xi_\alpha(\mathrm{x}, t)\right] \tag{5.2.4}$$

Following (Fan et al. 2004), transport equations for weights and particle characteristics (abscissas) can be written as:

$$\frac{\partial \omega_\alpha}{\partial t} + \nabla \cdot (\mathrm{u}_{s\alpha}\omega_\alpha) = a_\alpha \tag{5.2.5}$$

$$\frac{\partial \omega_\alpha \xi_\alpha}{\partial t} + \nabla \cdot \left(\mathrm{u}_{s\alpha}\omega_\alpha \xi_\alpha\right) = b_\alpha \tag{5.2.6}$$

where a_α and b_α account for particle-fluid and particle-particle interactions. In this study, we assume that particles do not react, nucleate, aggregate, or break. For this specific case a_α and b_α coefficients become zero. If we consider ξ as the particle size, then the volume fraction and weights and abscissas can be related as:

$$\varepsilon_{s\alpha} = k_v \xi_\alpha^3 \omega_\alpha \tag{5.2.7}$$

where k_v is a constant related to the sphericity of particles. For spherical particles, $k_v = \pi/6$. By combining equations (5.2.5) through (5.2.7) and incorporating the previously mentioned assumptions, the final form of transport equations for the particle phase can be written as:

$$\frac{\partial \varepsilon_{s\alpha}\rho_{s\alpha}}{\partial t} + \nabla \cdot (\mathrm{u}_{s\alpha}\varepsilon_{s\alpha}\rho_{s\alpha}) = 0 \tag{5.2.8}$$

Further modeling details, such as discretization schemes and gradient computations, are not discussed in this report, but are thoroughly discussed in the CD-adapco software manual (CD-adapco, 2013).

To determine initial conditions for our simulations using DQMOM model, we need to evaluate the particle size distribution, which accounts for polydispersity, inside the BFB multiphase system. The

statistics of this distribution help us determine different mean diameters are required in the simulation set up. They are needed to prescribe an initial particle distribution throughout the computational domain. Figure 7 shows the experimental PSD for the BFB system, as obtained by PSRI. According to (Mazzei et al. 2010) experimental moments can be determined from the PSD with equation (5.2.9)

$$M_k = (1-\varepsilon)\sum_{i=1}^{n}\frac{w(d_{i-1},d_i)}{d_i - d_{i-1}}\frac{d_i^{k+1} - d_{i-1}^{k+1}}{k+1} \tag{5.2.9}$$

where n is the number of measurements, d is the diameter w corresponds to the mass fraction of material, ε is the solid volume fraction and k is the corresponding moment. Different moment ratios provide information about different diameters. For instance, the ratio of the first moment to the zeroth is the mean diameter. The ratio between the second moment and the first moment is the surface diameter. The ratio between the third moment and the second moment is the volume diameter or Sauter diameter. In this study, we have used the Sauter diameter as representative of the particle size throughout the simulations set up. Table 6 presents the different diameters calculated based on the experimental moments.

Table 6. Main moment ratios for the experimental distribution

	$D(1,0) = {M_1}/{M_0}$	$D(2,1) = {M_2}/{M_1}$	$D(3,2) = {M_3}/{M_2}$
Diameter (m)	$8.45\text{x}10^{-05}$	$9.371\text{x}10^{-05}$	$1.046\text{x}10^{-04}$

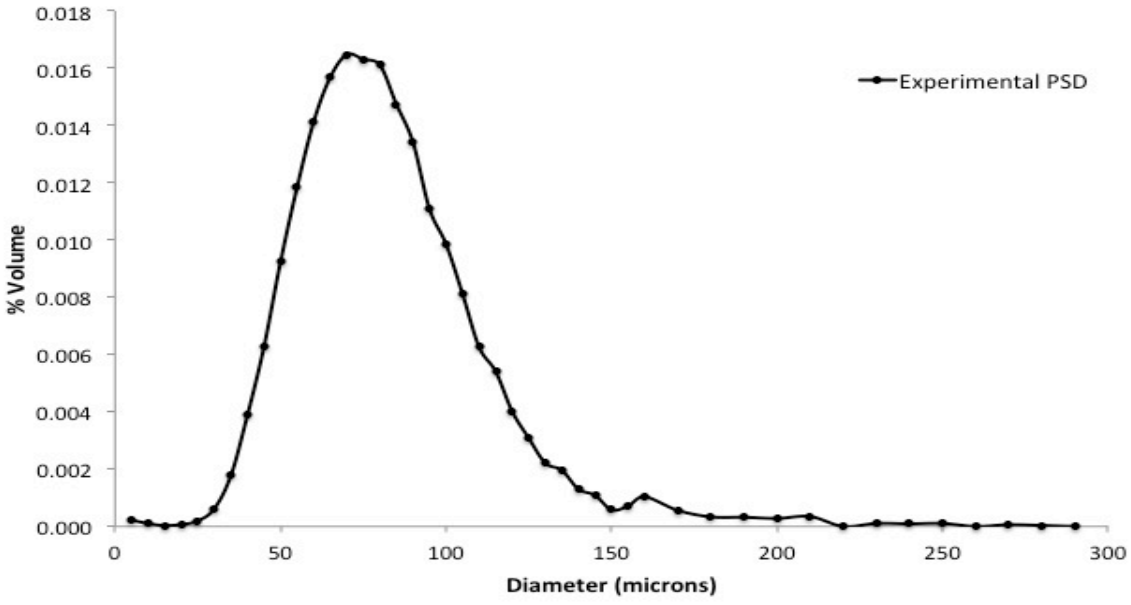

Figure 7. Experimental PSD.

Sensitivity Analysis

One of the key features that determines the fluid-dynamic behavior of any multiphase gas-solid system is its polydisperse character. Although this has been known since the development of the kinetic theory of granular flow (Sinclair and Jackson 1989), (Ding and Gidaspow 1990), only recent efforts towards the representation of this polydispersity character through modeling have been carried out (Fan and 2004), (Marchisio and Fox 2005), (Passalacqua and Fox 2010). Therefore, our sensitivity analysis study included the effect of numerical models to capture the polydisperse character of multiphase gas-solid systems, such as the BFB. The modeling parameters included three different models that track the solid distribution throughout the system: monodisperse model, DQMOM model with three classes of particles, and DQMOM model with five classes of particles.

In the monodispersity case, no particle size distribution (PSD) is taken into account, and the bed of particles is represented with one characteristic size (a mean diameter). For the polydispersity representation, a DQMOM formulation with either three or five classes was selected.

The sensitivity analysis of models, or modeling parameters, was conducted on the complete geometric representation of the BFB system. The complete BFB representation accounts for the fluidized bed reactor, cyclones, as well as interconnected pipes. It also included sensitivity analysis of physical parameters, namely the reactor height and superficial bed velocity. The sensitivity analysis for the physical space was carried out using reduced geometrical representation of the BFB system, which included only the fluidized bed reactor, but did not include the cyclones and interconnected pipes. The geometry differences are discussed in more detail further in the report. Table 7 highlights the sensitivity analysis space for both physical as well as modeling parameters.

Table 7. Sensitivity analysis.

	Physical Parameters		Modeling Parameters		
	BFB Height	*Superficial Bed Velocity*	*Monodisperse*	*DQMOM (3 classes)*	*DQMOM (5 classes)*
Fine Mesh (Complete Geometry)					
Case 1	2.44 m	0.3 m/s	✔	✔	✔
Coarse Mesh (Reduced Geometry)					
Case 2	3.66 m	0.3 m/s	✔	---	---
Case 3a	1.22 m	0.6 m/s	✔	---	---
Case 3b	1.22 m	0.3 m/s	✔	---	---

Geometry and Mesh Description

The fluidized bed system is a 0.895 m inner diameter, 6.1 m tall unit, as shown in Figure 8. An air sparger inside the bed provides sufficient pressure drop to ensure good air distribution. The system was intended for experiments at 0.3 m/s and 0.6 m/s fluidization velocities. For tests carried out at 0.3 m/s, a 0.76 m-PVC pipe manifold was used. For tests carried out at 0.6 m/s, a 0.102 m-PVC ring sparger shown in Figure 9 was used. The ring has 39, 0.0013 m nozzles facing downward 30º from the vertical. The

primary cyclone is a 0.2 m diameter dipleg that returns solids back onto the bed surface via an aerated trickle valve. The secondary cyclone has a 0.152 m diameter dipleg that returns solids to the bed via a butterfly valve. Neither valve was included in the CAD design for simplicity. After initial testing, the investigators simplified the geometric representation of the ring sparger due to difficulty of producing a high-quality mesh in the surrounding area. Instead, they imprinted nozzle outlets directly onto a face in the sparger and prescribed appropriate gas exit velocities and angular orientations, which, indirectly, account for the sparger nozzles. This change allows for better meshing control, yet it very closely resembles the same dynamic behavior of solids as in the experiment. This modification further allows for more computationally efficient simulations. Figure 10 shows the CAD geometry created in STAR-CCM+.

The simulations used two geometries. The first geometry included the entire BFB system, including the reactor, cyclones and the interconnected pipes is shown in Figure 10. The second geometry included only the reactor, without cyclones and interconnected pipes and is shown in Figure 11. The simulations of the first case, Case 1, were completed using geometric representation of the entire BFB system, while subsequent simulations of Case 2 and Case 3 were completed on the partial CAD representation of BFB system, which included only the reactor. For cases 2 and 3 geometry only included only the reactor, which decreased the computational effort required to complete the cases.

For Case 1, in order to resolve fine geometric features and limit stiffness of the solution equations, we have employed multiple levels of refinement to achieve moderate-quality cells. The mesh size was around 2.3 million cells (Figure 12). While not necessarily large for pure CFD computations, for simulations involving multiphase systems this translates to a significant computational effort. This fact led us to decrease the overall size of the CAD geometry for our subsequent simulations of Case 2 and Case 3. Therefore, the decreased the complexity of the CAD geometry reduced the computational cell count to 700,000. This mesh can be seen in Figure 13.

Because of variations in the size of the mesh, the average time step for the different simulations varied between $1x10^{-3}$ to $1x10^{-6}$ s. This ensured stability and proper convergence of all simulations.

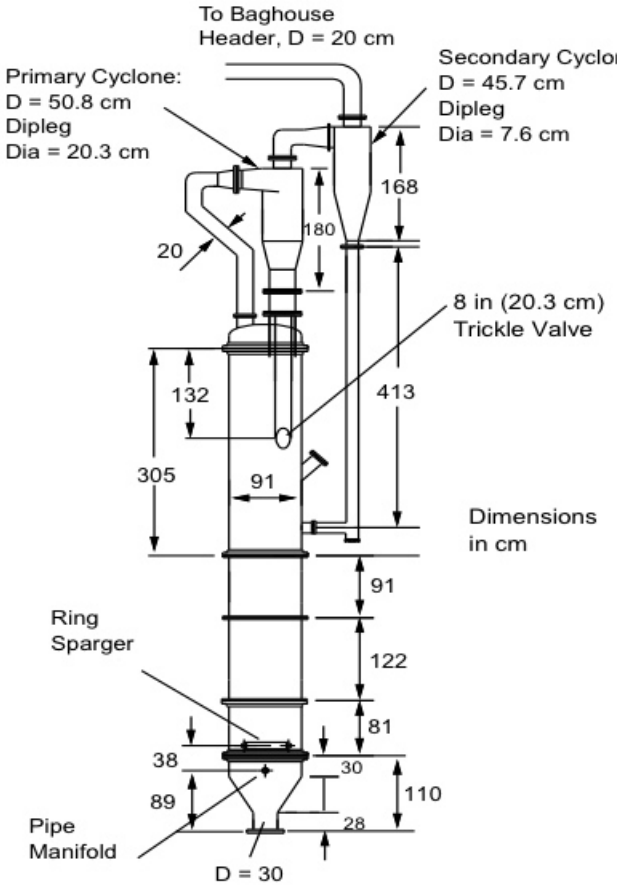

Figure 8. Schematic drawing of the bubbling fluidized bed unit.

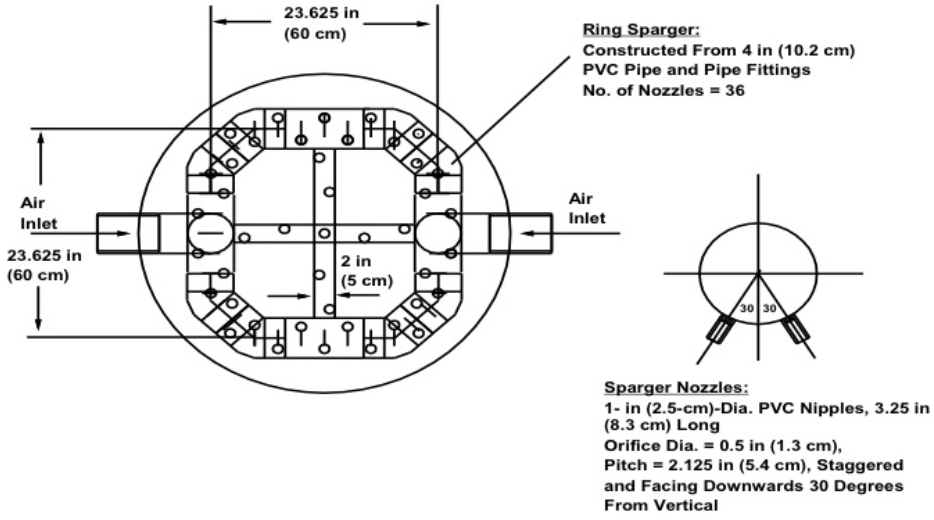

Figure 9. Ring sparger for air distribution inside the unit.

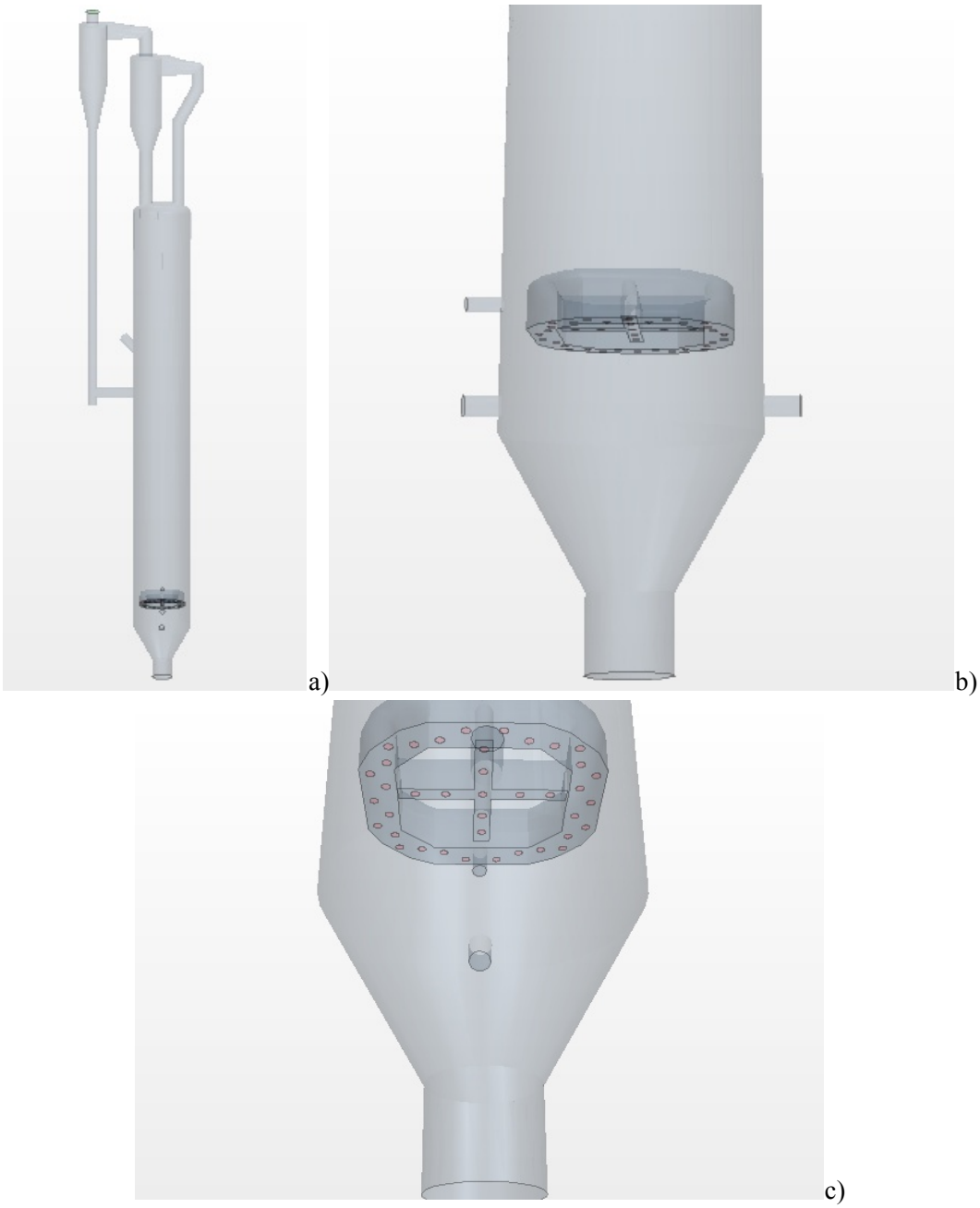

Figure 10. The complete BFB system created in STAR-CCM+. a) Entire unit. b) Ring sparger side view. c) Ring sparger bottom view.

Figure 11. Reduced geometrical representation of the BFB, containing only the fluidized bed.

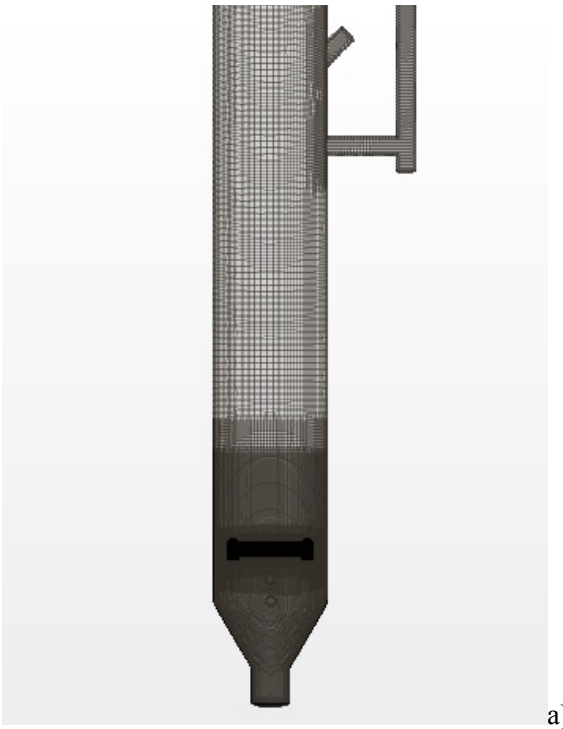
a)

b)
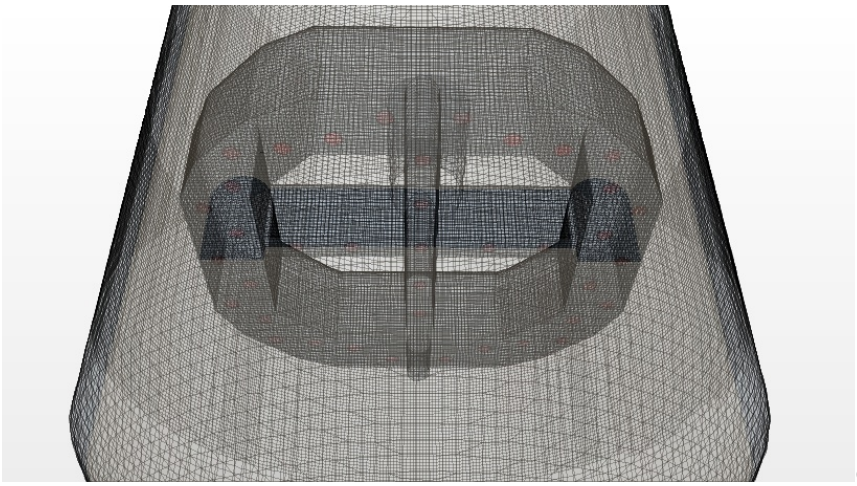
c)

Figure 12. Complete geometry mesh. a) Bottom half. b) Top half. c) Mesh refining around the ring sparger.

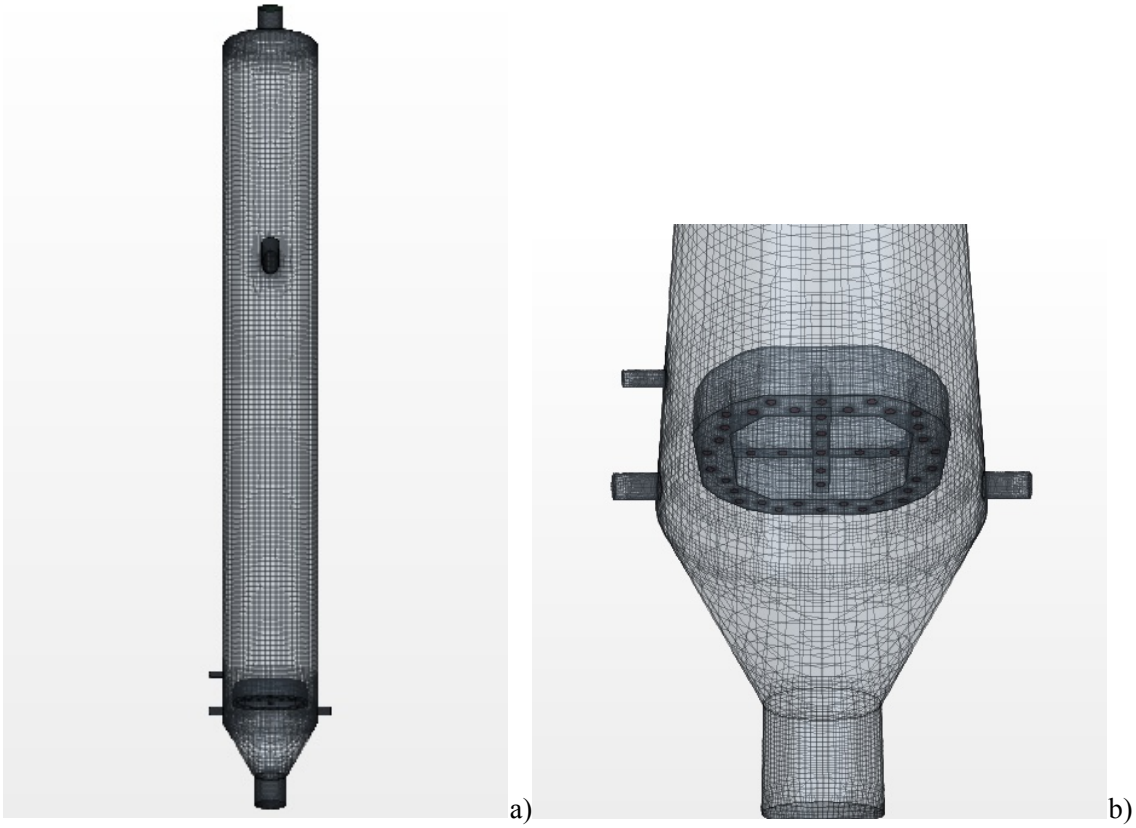

Figure 13. Mesh for the reduced geometry. a) Overall mesh. b) Sparger mesh detail.

Subtask 5.3 – Laboratory-Scale CLC Studies

This subtask focuses on the CLOU form of CLC, and in particular focuses on copper-based CLOU carriers. While much research on copper-based CLOU carriers has been reported, most focuses on physical performance of individual oxygen carriers. Presumably the mechanisms responsible for oxidation and reduction (oxygen release) are similar for all copper-based oxygen carriers. It was the goal of this study to develop a set of universal, carrier-independent expressions that would describe the rate of oxidation or reduction as a function of temperature, gas environment and particle conversion.

Oxygen Carriers

Experimental work focused solely on copper-based carriers and the CLOU process in which oxygen is spontaneously released in the fuel reactor as the carrier is reduced. Copper, while relatively costly, is especially reactive and well characterized. Because of its CLOU capabilities copper-based oxygen carriers may be utilized to directly combust coal without gasification either upstream or in-situ. Not only does gasification incur additional process complexities, but the kinetics of coal gasification are much slower than those of combustion. The rate of reduction of copper from CuO to Cu_2O is faster than coal

gasification rates at the same temperatures (Lewis et al., 1951), which makes copper-based oxygen carriers especially attractive.

For CLOU, looping of copper is between the CuO and Cu_2O states. The following equations represent the redox reactions of CuO/Cu_2O:

Reduction:	$4\ CuO \rightarrow 2\ Cu_2O + O_2$	$\Delta H_{850} = 263$ kJ/mol O_2
	$C + O_2 \rightarrow CO_2$	$\Delta H_{850} = -379$ kJ/mol O_2
	$4\ CuO + C \rightarrow 2\ Cu_2O + CO_2$	$\Delta H_{850} = -133$ kJ/mol O_2
Oxidation:	$2\ Cu_2O + O_2 \rightarrow 4\ CuO$	$\Delta H_{850} = -263$ kJ/mol O_2

Even though the reduction of CuO to Cu_2O is endothermic the combustion of carbon and oxygen is exothermic enough to generate an overall exothermic reaction.

In the studies reported here, several copper-based oxygen carriers were used. The carriers had different loadings of CuO and were manufactured by different techniques. The carriers are summarized in Table 8.

Table 8. Copper-based oxygen carriers used.

Carrier Code	Source	Production Method	Mass % CuO
12_Al2O3_IW	Sigma Aldrich, USA	Incipient Wetness	12
50_TiO2_MM	ICPC, Poland	Mechanical mixing	50
45_ZrO2_FG	Chalmers, Sweden	Freeze granulation	45
50_SiO2_IW	University of Utah	Incipient Wetness	50
70_SiO2_IW	University of Utah	Incipient Wetness	70
20_FeTiO2_IW	University of Utah	Incipient Wetness	20

Thermogravimetric Analyzer

A TA Instruments thermogravimetric analyzer (TGA) Q500 with a maximum operating temperature of 1000°C was used to study oxygen carrying capacity and reaction rates. Samples ranging from 10 to 50 mg were loaded into small sample pans made of platinum or quartz. In order to maximize gas-solid contact and minimize mass transfer effects, small diameter particles (< 45 μm) and a shallow layer of particles (nearly a monolayer in the bottom of the pan) was used. Approximately 150 ml/min of either air or nitrogen was fed into the TGA and changes in mass were analyzed to determine oxidation and reduction rates.

Lab-Scale Fluidized Bed Apparatus

The schematic in Figure 14 represents the lab-scale reaction system built at the University of Utah. Gases are metered and fed through mass flow controllers into a small quartz fluidized-bed reactor which is housed in a furance. Most tests were performed using a 2.5-cm diameter reactor. In order to simulate a dual-fluidized-bed reactor system a single bubbling bed is utilized, and is switched between oxidizing and reducing gases.

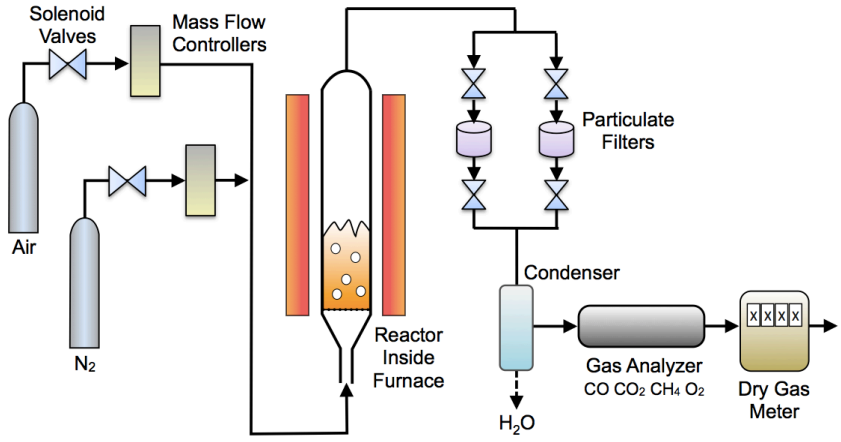

Figure 14. Schematic of the bubbling bed CLC reactor system at the University of Utah.

Tests were performed at several temperatures ranging from 650°C to 950°C. In order to achieve fluidized conditions gas flow rates ranged from 1.5 SLPM to 5 SLPM. These flow rates correlated to U/U_{mf} of 20-60 (where U is the superficial gas velocity and U_{mf} is the theoretical minimum fluidization velocity). For each test, 30 to 100 grams of carrier material was placed into the reactor. Enough material was used to fill the reactor to one diameter bed height when not fluidized. The reactor was then placed within the furnace where the temperature was ramped at 5°C per minute to the desired operating temperature.

Reacting gases are supplied from laboratory gas cylinders. The flow of each gas is controlled by a mass flow meter, which is also used to turn gas flow off if it is not needed for a particular cycle. The gases flow through the quartz reactor, which is housed within a clamshell furnace. Two type K thermocouples are located within the reactor to measure the temperature of gases at the reactor entrance, below the distributor plate, and the center of the reacting bed. Upon exiting the reactor a coil of metal tubing is used to cool the effluent and condense the moisture created in combustion. From the coil the gas enters a pair of parallel filters to capture any fractured carrier particles. The gases are then analyzed in a NDIR/O_2 analyzer which measures concentrations of CH_4, CO_2, CO, and O_2. After analysis the gases are exhausted.

The reactor itself is made from quartz. The main reactor section includes a sintered quartz disc which acts as a gas distributor. Above the bed, the diameter expands to slow the gas velocity thereby

minimizing the possibility of particulate carryover. The filter on the product gas line was weighed before and after each test to determine the degree of particle attrition.

Interpretation of data from the fluidized bed system involves deconvolution of the gas concentrations measured with the analyzer, then identification of rates and degrees of oxidation and reduction of the copper. These procedures were described in the previous topical report (Sarofim et al. 2011).

Subtask 5.4 – CLC Kinetics

Development of Supported Copper Oxide

Wet Impregnation Preparation Method

The support material and the appropriate amount of $Cu(NO_3)_2$ were mixed in solution. The literature suggests that multiple additions of the active CuO improved the performance of the oxygen carrier, so the samples were prepared by multiple CuO additions (Corbella et al. 2005). The amount of $Cu(NO_3)_2$ for each addition was calculated based on the total number of additions and the weight of support material being used to give a certain CuO% by weight. The materials were stirred with a magnetic stir bar for at least 4 hours submerged in the solution. After sufficient stirring, the sample was dried at 110^{o}C and then calcined at 180^{o}C overnight to promote the loss of all NO_x gasses leaving CuO on the support material. The temperature was selected because preliminary experiments showed that higher temperature calcinations (400°C) did not improve the performance of the material. Subsequent additions of $Cu(NO_3)_2$ then took place until the desired CuO% by weight was reached.

Preparation by Rotary Evaporator

Samples prepared by the rotary evaporation method were made similarly to wet impregnation samples. The support material and $Cu(NO_3)_2$ were mixed in solution; however, the evaporation of the solvent and the subsequent calcination occurred in one single apparatus: the rotary evaporator. The rotary evaporator promoted the rapid evaporation of the solvent, allowing for a more uniform deposition of $Cu(NO_3)_2$ onto the surface of the support material. Once the sample was dry, the temperature was increased at a rate of approximately 25°C/min to a final external temperature of about 350^{o}C. The sample was left rotating at that temperature until the sample had turned black and a brown gas had formed in the flask. The brown gas was the result of NO_x gasses being released from the sample leaving CuO on the support material surface. After the brown gas had left, the flask was removed and allowed to cool to room temperature. When the flask had cooled, the subsequent additions took place. After all the additions had been carried out, the samples were kept in an oven at 180^{o}C overnight.

β-SiC Support Preparation Method

Samples using β-SiC as support material were prepared using three methods. One of them is the same rotary evaporation method described above. The two other methods include two fundamental steps: the deposition of CuO and the calcination of the β-SiC support material to promote its conversion to SiO_2.

The only difference between these two methods is the order in which the two steps occur. For simplicity, these two methods will be referred to as the bake then coat, and the coat then bake methods.

For the bake then coat method, the β-SiC powder was first calcined in a muffle furnace at 980°C for seven days. After calcination, CuO was then deposited to the SiO_2 material by the rotary evaporation method.

For the coat and bake method, CuO was added to the β-SiC support material by the rotary evaporation method. The material was then calcined in a muffle furnace at 980°C for seven days. The resulting material was then crushed and sieved between 204 and 124μm.

TGA Experimental Setup

Each supported CuO sample was analyzed by TGA experiments to determine its reactivity in multicycle tests (for details see Sarofim et al. 2011). The TGA experiments were conducted in the TA Q600 and TA Q500 instruments. Rate constants were determined for experiments carried out under isothermal conditions at 935°C.This temperature was chosen to compare the results between the various supports used because both the oxidation and reduction reactions occur at a relatively fast rate. The sample was heated to the isothermal temperature in air. Once a steady temperature was reached, the air was replaced by N_2. This promoted the reduction of the CuO in the sample. To promote the oxidation of the Cu_2O, the air was switched back on.

For experiments using the Q600, the air flow consisted of 100 mL/min of N_2 and 100 mL/min of air. During the portions of the experiment in which the reduction occurred, the flow of N_2 was increased to 200mL/min. Thus, a total flow of 200mL/min was maintained throughout. Due to the design of the instrument, there is a time period required during which the gas is purged through the chamber. To achieve a more immediate change of gas compositions, the air was controlled manually by bypassing the built-in gas control.

TGA Analysis Procedure

Thermogravimetric analysis permits observation of mass change as a function of time and temperature. Utilizing TGA with gas changes allows for observation of CuO reduction and Cu_2O oxidation.

$$4CuO(s) \rightleftharpoons 2Cu_2O(s) + O_2(g) \tag{5.4.10}$$

Fractional completion, X, describes reaction progression. Fractional completion is defined in terms of mass at a given time (m_t), mass of the reduced sample, Cu_2O (m_{red}), and mass of fully oxidized CuO (m_{ox}). For oxidation, X_{ox}, and reduction, $X_{red,}$ are defined as follows:

$$X_{ox} = \frac{m_t - m_{red}}{m_{ox} - m_{red}} \tag{5.4.11}$$

$$X_{red} = \frac{m_t - m_{ox}}{m_{red} - m_{ox}} \quad (5.4.12)$$

The oxygen uncoupling experimental runs were treated according to a linear model. The experimental runs were trimmed from 1% to 90% in order to capture the linear portion of the reaction kinetics. The calculated regression slope would approximate the rate constant, dX_{red}/dt, in units of s^{-1}.

There have been inconsistencies in the models used to describe oxidation of cuprous oxide. Proposed models include the parabolic rate law, the cubic rate law, and the logarithmic rate law (Zhu et al. 2004). Oxidation mechanism of Cu_2O to CuO at 600-1050°C Initial analysis of each isotherm, suggested that the logarithmic rate model best fits each isotherm. Additionally, the logarithmic rate law assumes non-uniform properties such as would be given by copper oxide powder (Zhu et al. 2004). Thus, the oxidation data were treated according to the pseudo first order model:

$$X_{ox} = X_f - (X_f - X_i)e^{-k(t-t_o)} \quad (5.4.13)$$

Considering that all oxidation reactions were brought to completion for this study, experimental points were trimmed such that initial reaction completion (X_i) was 5% and final reaction completion (X_f) was 100%.

All reactions observed in the TGA experiments included an initial portion that did not conform to the models used for the oxidation and reduction reactions, and these were trimmed. This was due to instrumental variables including time requirements for oxygen to reach and penetrate the sample (oxidation) and leave the sample (reduction).

Particle Characterization

Promising oxygen carrier materials were imaged with a Hitachi S-300N scanning electron microscope (SEM) to permit visualization of the preparations on the scale of 10 μm to 1 mm. Energy dispersive X-ray spectroscopy (EDS) was carried out with an EDAX HIT S3000N 132-10 alongside the SEM images to confirm the appearance of and locate elemental silicon and copper.

The original scope of work included studying the reduction reactions with methane; however, the team focused on the spontaneous decomposition of the CuO/Cu_2O system on various support materials because it was more relevant to the other subtasks.

RESULTS AND DISCUSSION

Subtask 5.1 – Process Modeling and Economics

Development of kinetic expressions for CLOU

CuO Decomposition

The kinetics for CuO decomposition was determined for the regime where both fuel combustion and CuO decomposition occur. The slope of the curve, obtained by a plot between $-ln(1-X_{CuO})/(p_{O_{2,e}}-p_{O_2})_{avg}$ versus time yields the rate constant k_{CuO}. The rate constant for CuO decomposition k_{CuO} was calculated on the basis of these measurements. A plot of logarithm of k_{CuO} versus $1/T_{avg}$, according to the Arrhenius relation is shown in Figure 15. The fit yields the following equation for the reaction rate constant:

$$k_{CuO} = 3e^{(-2350/T)} \tag{5.1.21}$$

The activation energy from the first-order rate constant k_{CuO} of the data for CuO/ZrO_2 particles was calculated to be 20 kJ/mol. The largest error is likely to be in the outlet oxygen concentration since this was assumed as the local oxygen concentration prevailing in the reactor. This was further investigated mathematically by lowering the experimental outlet oxygen concentration by 50% and determining k_{CuO}. This resulted in approximately a 25% difference in the activation energy. Therefore, 20 kJ/mol +/- 5 kJ/mol is likely to be the range of activation energy of CuO, which represents the energy required to overcome the kinetic barrier.

The standard enthalpy of reaction at 1200 K (927°C) for the reaction $4CuO(s) \rightarrow 2Cu_2O(s)+O_2(g)$ is 261 kJ/mol (Pankrantz, 1982). The sum of the standard enthalpy of reaction and the activation energy obtained for CuO supported on ZrO_2 particles in the size range of 125-180 μm by analyzing batch fluidized bed data is 281 kJ/mol. The value is close to the reported activation energy values of 322 kJ/mol for pure unsupported 10 μm CuO particles (Chadda et al. 1989) and 327 kJ/mol for pure unsupported 1-10 μm CuO particles, which Eyring et al. (2011) obtained from TGA experiments on CuO decomposition. The experimental data obtained by TGA analysis (Chadda et al. 1989, Eyring et al. 2011) was modeled by a first-order CuO decomposition model and does not consider the separation of effects of chemical kinetics and partial pressure (thermodynamics). The above rate analysis, although it contains certain simplifying assumptions, is in excellent agreement with other independent measurements. It also indicates that the kinetic barrier is much smaller than the thermodynamic barrier for CuO decomposition, i.e. approximately 20 kJ/mol as compared with 260 kJ/mol. A comparison was made between the experimental data of CuO decomposition versus time and the rate equation represented by Equation (5.1.22):

$$\frac{dX_{CuO}}{dt} = k_{CuO}\overline{(p_{O_{2,e}}-p_{O_2})_{avg}}(1-X_{CuO}) \tag{5.1.22}$$

Figure 16 indicates that Equation 5.1.22 reasonably predicts the experimental data for CuO decomposition.

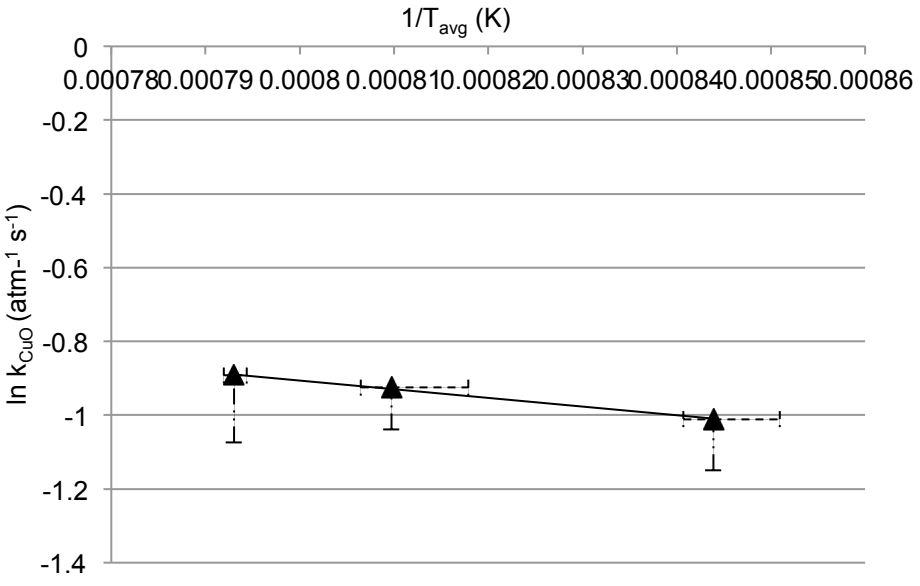

Figure 15. Logarithm of rate constant of CuO decomposition (ln k_{CuO}) versus $1/T_{avg}$ [▲ Experimental Data, − Equation Fit, - - Error Bar representing the temperature measurement range, − ·· − Error bar representing the scenario if the outlet partial pressure of O_2 is reduced by half.

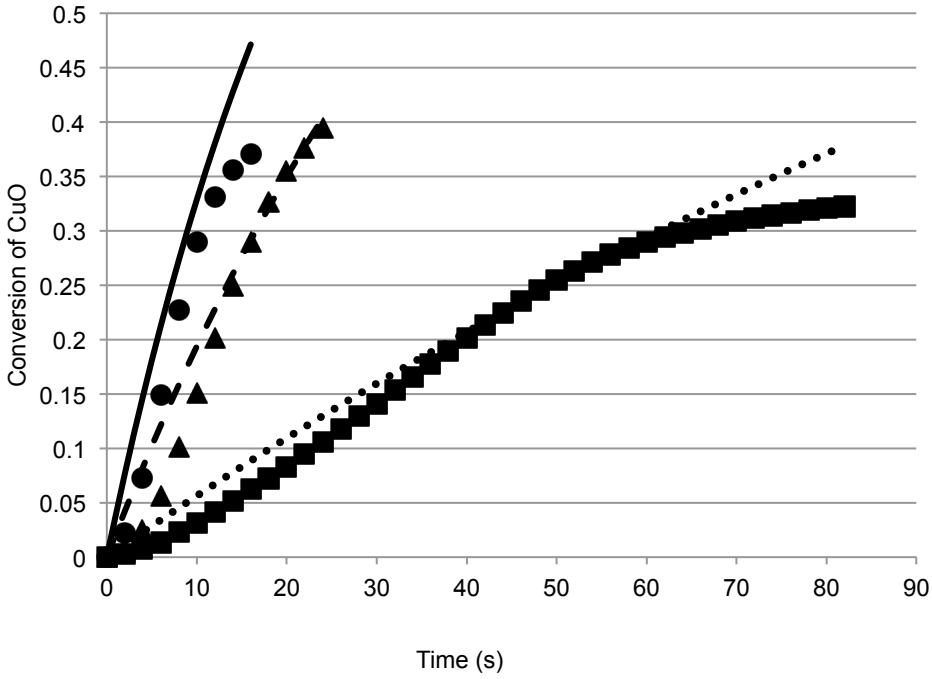

Figure 16. Comparison of experimental data and prediction from rate equation of CuO decomposition with time [■ Experimental Data: 900°C, ···· Prediction: 900°C , ▲ Experimental Data: 950°C, − − − Predictions:950°C, ● Experimental Data: 985°C, − Prediction:985°C].

Cu_2O Oxidation

Equation (5.1.11) relates the time required to achieve a certain conversion of Cu_2O to the sum of time required to attain the same conversion under chemical reaction control plus the time required to attain the same conversion under reaction rate control by gas pore diffusion and external mass transfer effects. The first term of the right hand side of equation (5.1.11) incorporating the $g_{F_g}(X)$ function represents the rate of the reaction of individual grains. At higher temperatures, the apparent rate constant $k_{Cu_2O,app}$ contained in this term may contain the effect of solid-state diffusion in CuO layer. At higher temperatures due to sintering, the CuO layer over the Cu_2O grain may become less porous or very dense (Priedsky and Vinogradov, 2004; Zhu et al. 2004). In such a case the Cu_2O oxidation could proceed through the solid state diffusion of species. The data is represented for 80% conversion, as for any gas-solid reaction, when the conversion versus time profile has a long tail, small differences in measured conversion over a long time interval become sensitive to error. Hence, inclusion of experimental data at higher conversions may not be representative of the driving force as described by Equation (5.1.11).

Figure 17 represents the comparison of experimental Cu_2O conversion versus time data at 950°C (at 10% O_2 inlet concentration) with Equation (5.1.11), where 80% conversion takes place at 290 seconds at 950°C. The value of $k_{Cu_2O,app}$ calculated for the oxidation experiment at 950°C is 18.6 s^{-1}. These apparent rate constants take into account the resistance to the O_2 diffusing through the non-porous and more dense CuO product layer around each grain of Cu_2O (Priedsky and Vinogradov 2004, Zhu et al. 2004). In the data analyzed, the gas pore diffusion through the particle from its outer surface to its interior and the external mass transfer were much faster than the reaction of each grain of Cu_2O distributed throughout the particle. Thus the overall rate for Cu_2O oxidation is controlled by the reaction of each Cu_2O grain. It was identified that the rate of Cu_2O oxidation becomes slower as the temperature increases due to the reason explained above.

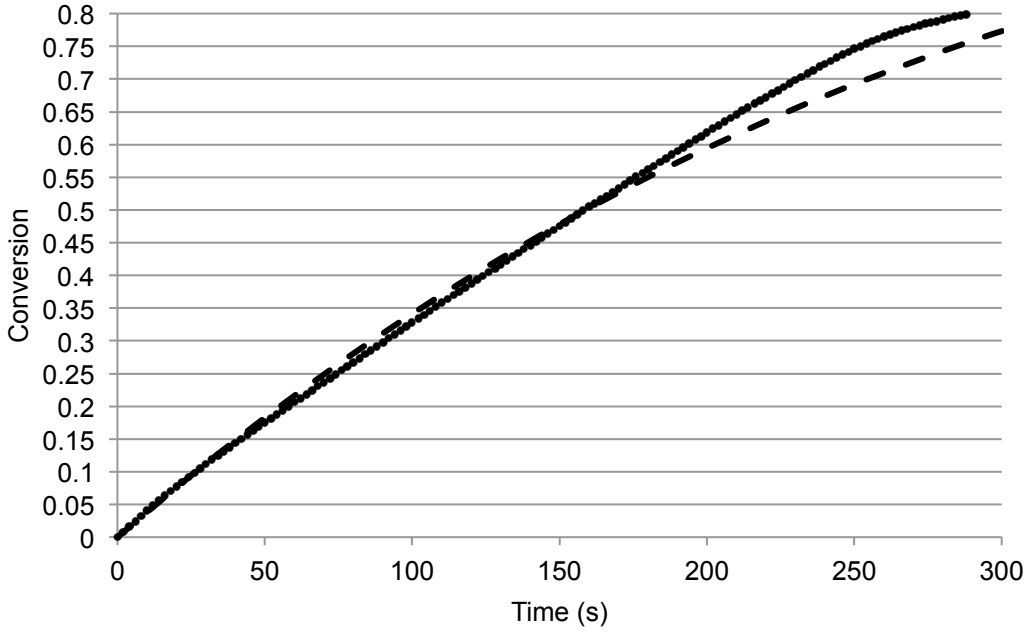

Figure 17. Comparison of experimental data for conversion of Cu_2O versus time at temperatures of 950°C (oxidation with 10% O_2 in N_2) with the Equation 5.1.11 derived by the law of additive reaction times for $k_{app,Cu2O} = 18.6\ s^{-1}$ (● experimental data points, - - - conversion for chemical reaction control).

Mexican Petcoke Oxidation

Figure 18 represents the logarithm of $k_{r,C}$ versus the inverse of the average temperature, T_{avg} which yielded the activation energy and pre-exponential factor. The reaction rate constant $k_{r,C}$ was investigated in the same temperature range as CuO decomposition. Thus,

$$k_{r,C} = 930e^{(-15500/T)} \quad (5.1.23)$$

The activation energy for the Mexican petcoke was calculated to be 129 kJ/mol by Equation. Hurt and Mitchell (1992) studied a variety of U.S. coals in the size range of 106-125 μm and in the temperature range of 1227-1427°C. They found that Pocahontas coal char, having comparable carbon content and heating value as compared to the petcoke, had an activation energy of 126 kJ/mol. The ultimate analysis of Pocahontas coal analyzed by Hurt and Mitchell (1992) and Mexican petcoke are compared in Table 9. The pre-exponential factors for the two solid fuels were 930 $g/cm^2atm^{0.5}s$ for Mexican petcoke versus 114 $g/cm^2atm^{0.5}s$ reported for Pocahontas coal char.

Table 9. Ultimate analysis for non-reactive coals used for comparison (Smith et al. 1994, Mattisson et al. 2009a).

Coal	C(wt% d.a.f)	H (wt% d.a.f)	O(wt% d.a.f)	N(wt% d.a.f)	S(wt% d.a.f)	Cl(wt % d.a.f)	Heating Value (MJ/kg)-as recd.
Mexican Petcoke	88.8	3.1	0.5	1.0	6.6	-	30.9
Pocahontas	91.48	4.38	2.30	1.10	0.69	0.06	33.4

Figure 19 shows the comparison of the experimental data with the kinetic equations and indicates the adequacy of the relationship utilized to predict the conversion of solid fuel used in the experimental study.

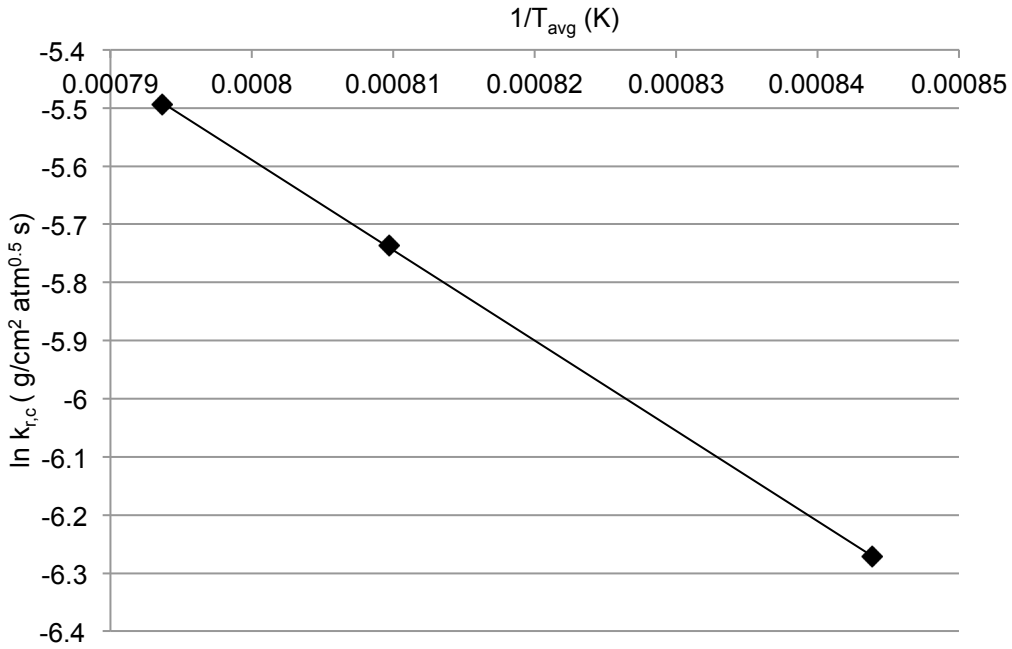

Figure 18. Logarithm of global reaction rate constant of Mexican petcoke oxidation (ln $k_{r,C}$) versus $1/T_{avg}$ [♦ experimental data, − equation fit].

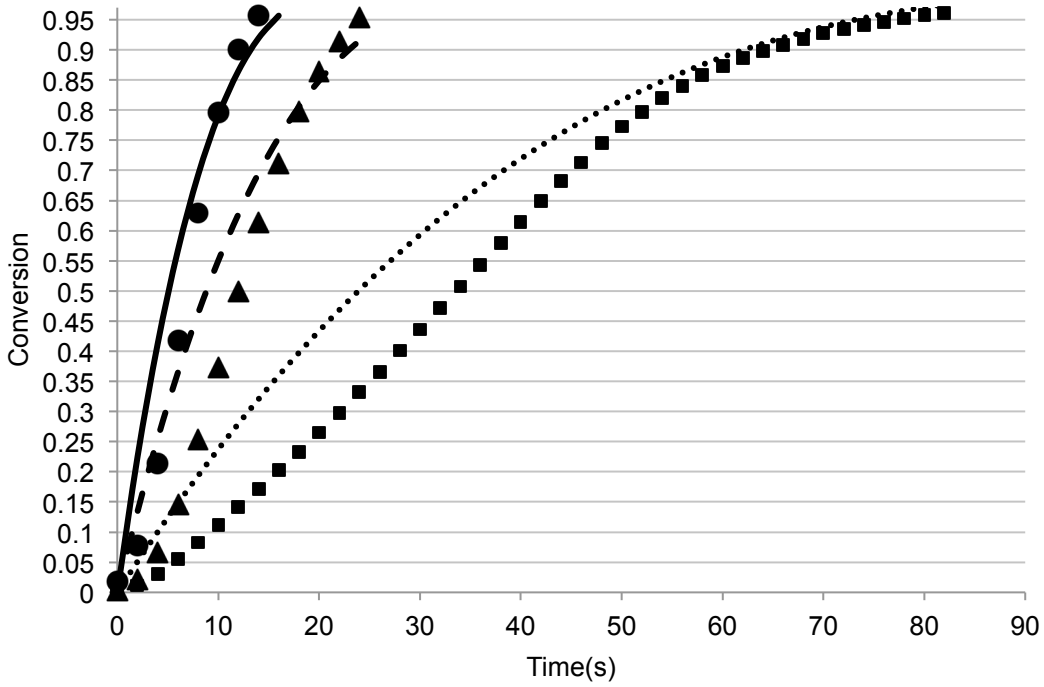

Figure 19. Comparison of experimental data and prediction by rate equation of Mexican Petcoke particles with time [■ experimental data: 900°C, ···· prediction: 900°C, ▲ experimental data: 950°C, – – – prediction: 950°C, ● experimental data: 985°C, −prediction: 985°C].

Development of a Custom Model for CLOU

The fluidized-bed reactor model was utilized to evaluate the O_2 concentration trends at the exit cell of the reactor with the help of Equation (5.1.24):

$$p_{O_2}{}^{exit} = \left[\frac{f_{g,b}p_{O_2}{}^{bbl} + f_{g,e}p_{O_2}{}^{em}}{(f_{g,b}+f_{g,e})}\right]_{exit} \tag{5.1.24}$$

The initial conditions for the concentration of O_2 are defined by the concentration prevailing in the system before the fuel particles are introduced in the fluidized bed. Figure 20 represents the comparison of O_2 concentration trends at 950°C. Similar results were also obtained for 885, 900, 935 and 985°C. The results indicate that the model reasonably predicts the oxygen concentration trends.

As the O_2 concentration data are primarily low in magnitude and may exhibit more uncertainty, CO_2 trends were also investigated. Figure 21 represents the comparison of CO_2 concentration trends at 950°C. Similar results were also obtained for 885, 900, 935 and 985°C. The results indicate that the model reasonably predicts the CO_2 concentration trend, with an error of 20%. The initial conditions for the concentration of CO_2 is zero at t=0 as no fuel particles have been introduced in the fluidized bed. The model predictions for CO_2 were evaluated at the exit cell of the reactor by:

$$p_{CO_2}{}^{exit} = \left[\frac{f_{g,b}p_{CO_2}{}^{bbl} + f_{g,e}p_{CO_2}{}^{em}}{(f_{g,b}+f_{g,e})}\right]_{exit} \quad (5.1.25)$$

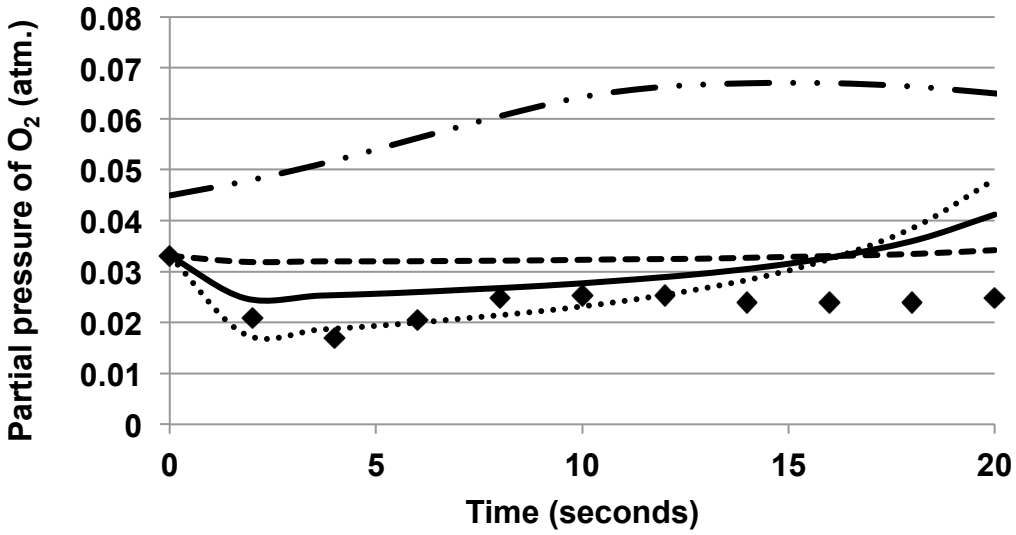

Figure 20. O_2 concentration trends at 950°C (♦ Experimental data, ─ ¨ ─ O_2 equilibrium concentration for the reaction $4CuO(s) \rightarrow 2Cu_2O(s)+O_2(g)$ determined from experimental temperature measurements, ── Model predictions of the O_2 concentration, - - Model predictions of the O_2 concentration in the bubble phase, ··· Model predictions of the O_2 concentration in the emulsion phase).

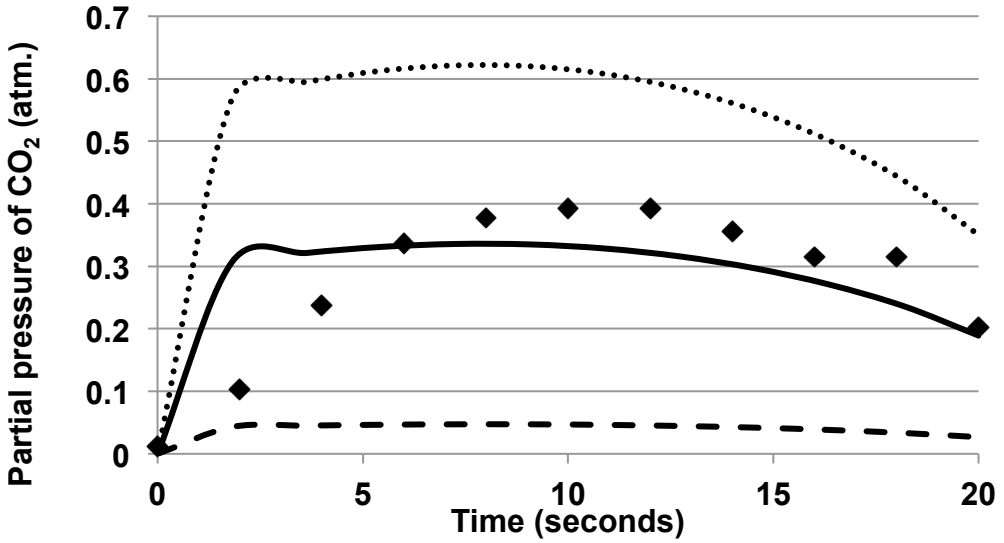

Figure 21. CO_2 concentration trends at 950°C (♦ Experimental data, ── Model predictions of the CO_2 concentration.··· Model predictions of the CO_2 concentration in the emulsion phase, - - Model predictions of the CO_2 concentration in the bubble phase)

Development of ASPEN PLUS Process Models for CLOU and CLC

ASPEN PLUS Process Model for CLOU using a Copper-Based Oxygen Carrier

Figure 5 represents a schematic of the ASPEN PLUS model developed for analyzing the CLOU process. Table 10 outlines the parameters for the ASPEN PLUS process model for CLOU. The energy contributions and requirements associated with the various process units in the ASPEN PLUS process model are detailed in Table 11.

The fuel reactor is at 950°C, and air reactor is at 935°C. In addition, the table indicates that both the fuel and air reactors are exothermic, indicating energy recovery is possible from both reactors. The energy which could be recovered in a CLOU unit is 513 kW_{th} with 5 kW_{th} consumption in energy requirements for fluidizing oxygen carriers. An oxygen carrier circulation rate for CLOU of 129 kg oxygen carrier/kg coal with 40% CuO on ZrO_2 was determined based on an optimum conversion of 54% in the fuel reactor and 50% in the air reactor.

Table 10. Parameters for ASPEN PLUS process model and pressure drop calculations for CLOU.

Air Flow Rate	986 kg/h
Temperature of Fuel Reactor investigated	950°C
Temperature of Air Reactor investigated	935°C
Mass flow rate of CuO at the inlet of the fuel reactor	3392 kg/h
Mass flow rate of Cu_2O at the inlet of the fuel reactor	1648 kg/h
Mass flow rate of CuO at the exit of the fuel reactor	1560 kg/h
Mass flow rate of Cu_2O at the exit of the fuel reactor	3295 kg/h
Amount of ZrO_2 circulating in the system	7836 kg/h
Fraction of flue gas stream recycled for fluidization for fuel reactor particles	0.69
Particle density	2140 kg/m^3
Design superficial velocity for fuel reactor calculated based on particle properties	2.1 m/s
Design superficial velocity for air reactor calculated based on particle properties	2.4 m/s

Table 11. Energy requirements and contributions (in kW_{th}) obtained from ASPEN PLUS process model for CLOU.

Fuel Reactor	Combustion of coal and reduction of metal oxide	109
	Energy required by oxygen carrier to attain fuel reactor operation temperature	(35)
	Total for fuel reactor	74
Air Reactor	Oxidation of oxygen carrier	394
	Energy provided by oxygen carrier to attain air reactor operation temperature	33
	Energy required for heating air from 25°C to air reactor temperature	(265)
	Total for air reactor	162
Energy required to heat recycled gas from 150°C to fuel reactor temperature for fluidization		(185)
Energy associated with cooling air reactor exhaust to 25°C		196
Energy associated with cooling flue gas from fuel reactor temperature to 150°C		271
Energy required for fluidizing the gas in the fuel and air reactors, and for compressing steam		(5)
TOTAL		513

ASPEN PLUS Process Model for CLC Using an Iron-Based Oxygen Carrier

The ASPEN PLUS process model for CLC was analyzed for two different temperatures. In the first scenario, the fuel reactor temperature was considered to be at 950°C and the air reactor temperature as 935°C. This estimate was based on the optimum temperature, which was found for the CLOU process as discussed in the earlier section. Another scenario for the CLC process was investigated based on the design temperatures of the 1 MW_{th} pilot at Technische Universität, Darmstadt, Germany. The design temperature of the fuel reactor is 970°C and for the air reactor is 1050°C (Orth et al. 2012).

For the CLC ASPEN PLUS model the pertinent parameters used for analyzing both scenarios are listed in Table 12. The results of an ASPEN PLUS models for CLC based on the transition from Fe_2O_3 to Fe_3O_4 indicates a circulation rate of 98 kg oxygen carrier/kg coal for combustion with 60% Fe_2O_3 on Al_2O_3 oxygen carrier.

Table 12. Parameters for ASPEN PLUS process model and pressure drop calculations for CLC.

Air Flow Rate	714 kg/h
Mass flow rate of Fe_2O_3 at the inlet of the fuel reactor	4740 kg/h
Mass flow rate of Fe_3O_4 at the inlet of the fuel reactor	1145 kg/h
Mass flow rate of Fe_2O_3 at the exit of the fuel reactor	0.02 kg/h
Mass flow rate of Fe_3O_4 at the exit of the fuel reactor	5728 kg/h
Amount of Al_2O_3 circulating in the system	3951 kg/h
Particle density	3200 kg/m^3
Design superficial velocity for fuel reactor at 950°C calculated based on particle properties	3.9 m/s
Design superficial velocity for air reactor at 935°C calculated based on particle properties	3.1 m/s
Design superficial velocity for fuel reactor at 970°C calculated based on particle properties	3.9 m/s
Design superficial velocity for air reactor at 1050°C calculated based on particle properties	3.3 m/s

Table 13 lists the energy requirements for various units and streams obtained from the ASPEN PLUS process model for both scenarios. The table also indicates that the fuel reactor requires energy if its temperature is greater than that of the air reactor. The endothermic gasification and metal oxide reduction requires 160 kW_{th}; 42 kW_{th} is required to heat the oxygen carrier from 935°C to 950°C for fuel reactor operation. Thus, 202 kW_{th} of energy has to be supplied to the fuel reactor. To avoid the addition of thermal energy to the fuel reactor, the temperature of the air reactor has to be higher than that of the fuel reactor. With the air reactor operating at a higher temperature of 1050°C (Scenario 2), it is possible to operate the fuel reactor in "auto-thermal" operation with a yield of 51 kW_{th}. Thermal energy could still be recovered from the air reactor, when the air reactor is operated at a higher temperature than the fuel reactor. The operation the air reactor at a higher temperature than the fuel reactor in CLC systems, which results in the oxygen carrier serving as a source of energy for the endothermic fuel gasification and metal oxide reduction reactions in the CLC fuel reactor. This mode of operation has also been discussed by Orth et al. (2012) and Markstrom et al. (2013a,b).

Table 13. Energy requirements and contributions (in kW_{th}) obtained from ASPEN PLUS process model for CLC.

		Scenario 1[1]	Scenario 2[2]
Fuel Reactor	Gasifying coal and reducing metal oxide	(160)	(161)
	Energy required/provided by oxygen carrier to attain fuel reactor operation temperature	(42)	212
	Total for fuel reactor	(202)	51
Air Reactor	Oxidation of oxygen carrier	663	658
	Energy provided/required by oxygen carrier to attain air reactor operation temperature	41	(205)
	Energy required for heating air from 25°C to air reactor temperature	(188)	(215)
	Total for air reactor	516	238
Energy required to heat steam from 150°C to fuel reactor temperature		(96)	(97)
Energy associated with cooling air reactor exhaust to 25°C		137	158
Energy associated with cooling flue gas from fuel reactor temperature to 150°C		117	121
Energy required for fluidizing the gas in the fuel and air reactors, and for compressing steam		(43)	(43)
TOTAL		429	428

1: Fuel reactor temperature = 950°C, air reactor temperature =935°C
2: Fuel reactor temperature = 970°C, air reactor temperature =1050°C.

Relative Economic Comparison between CLC and CLOU

Figure 22, Figure 23, Figure 24 represent the relative costs of CLC and CLOU processes for the 1, 10 and 100 MW_{th} scale, respectively. Comparing the capital costs of CLC relative to CLOU (i.e., values above 1 suggest CLC is more expensive, while values below 1 suggest CLOU is more expensive) revealed:

a) The cost of the reactor and the cyclone for CLC were greater than for CLOU due to the longer residence time associated with CLC reactions.
b) The longer residence times in the CLC fuel reactor, due to gasification reactions, and CLC air reactor result in higher compression costs.
c) CLC has a definite cost advantage in terms of the oxygen carrier (due to cost of iron versus copper based materials).
d) For the 100 MW_{th} scale, two process trains for the fuel reactor in CLC and CLOU were selected. There are also two process trains for the air reactor in the CLC process. In a CLC system, energy

can only be extracted from the air reactor in contrast to the CLOU process, which offers flexibility in extracting energy from both the fuel and air reactors. Thus for 100 MW_{th} scale, a single air reactor was used for the CLOU process, which reduced the capital costs. Thus, the possibility of extracting energy from the fuel and the air reactors could have a design implication in determining the number of process trains required at larger scale (~100 MW_{th}) if the CFB design criteria are utilized.

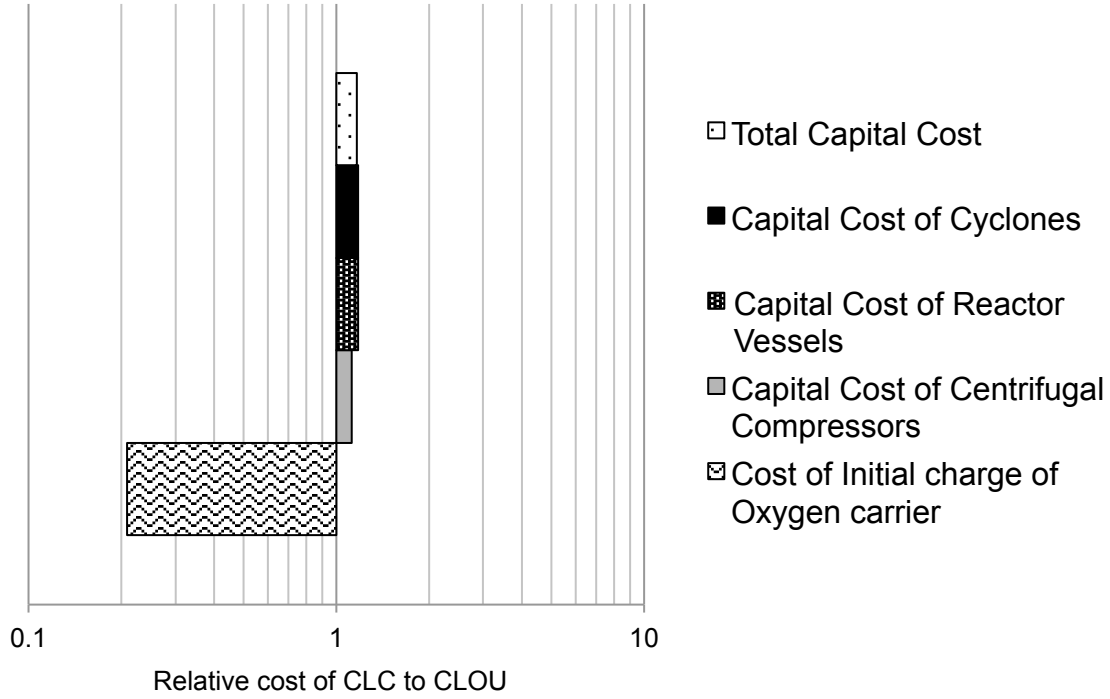

Figure 22. Relative capital costs of CLC and CLOU associated with 1 MW_{th} capacity.

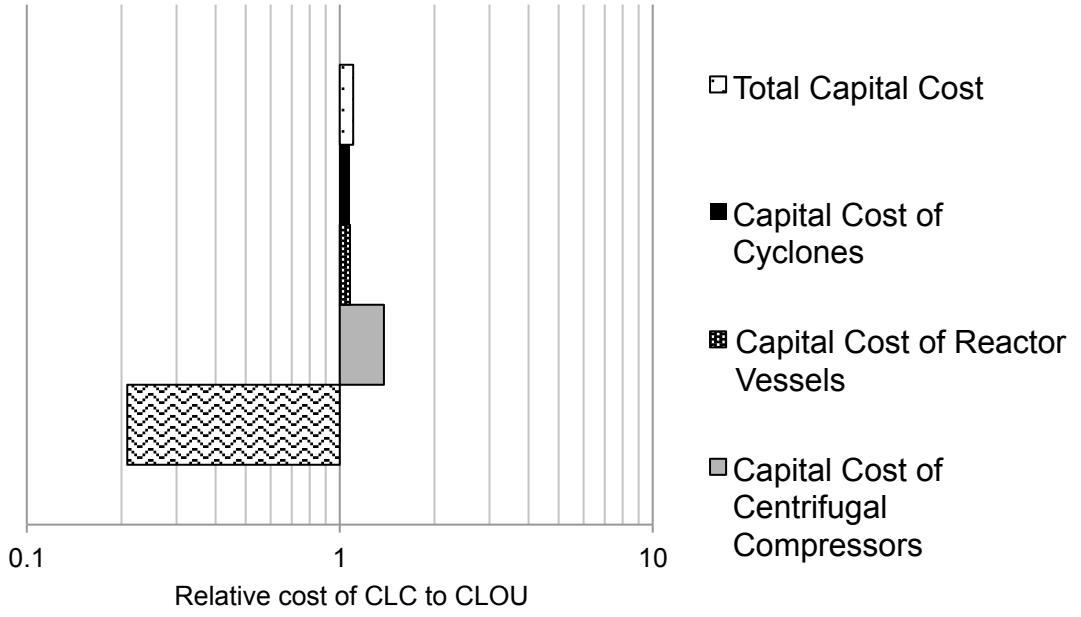

Figure 23. Relative capital costs of CLC and CLOU associated with 10 MW_{th} capacity.

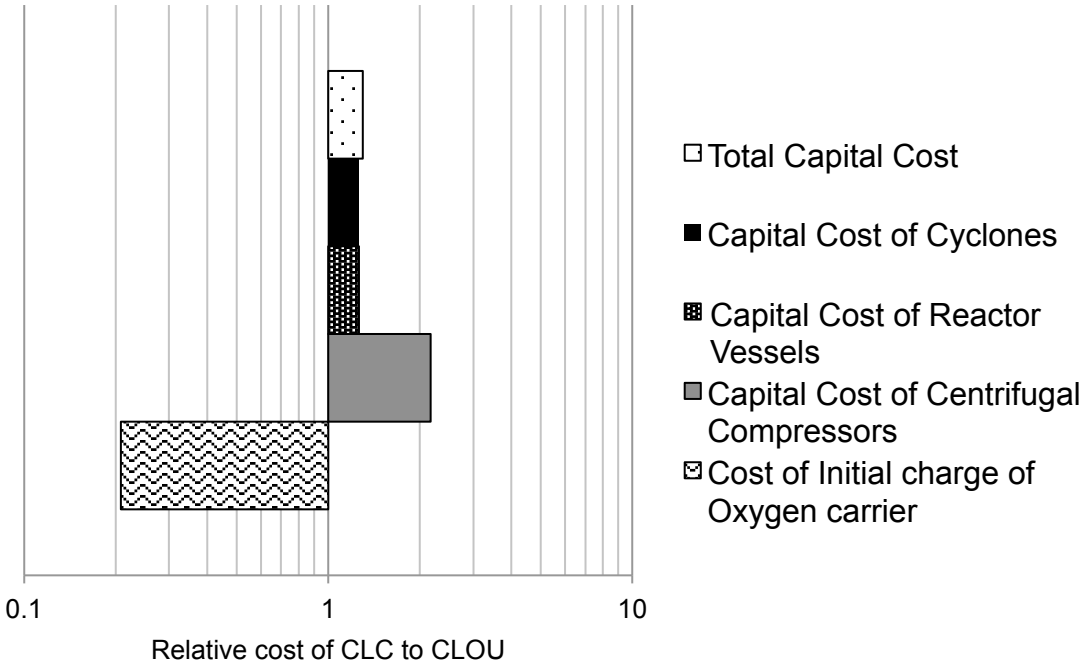

Figure 24. Relative capital costs of CLC and CLOU associated with 100 MW_{th} capacity.

The comparison of relative operating costs for the CLC and CLOU processes were identical for 1, 10 and 100 MW_{th} cases; therefore**,** Figure 25 illustrates all the operating costs. As seen in this figure, the total operating cost for CLC is at least twice as much as CLOU. This higher operating cost is attributed to the

energy requirements associated with fluidizing oxygen carriers owing to large residence times in the CLC fuel reactor.

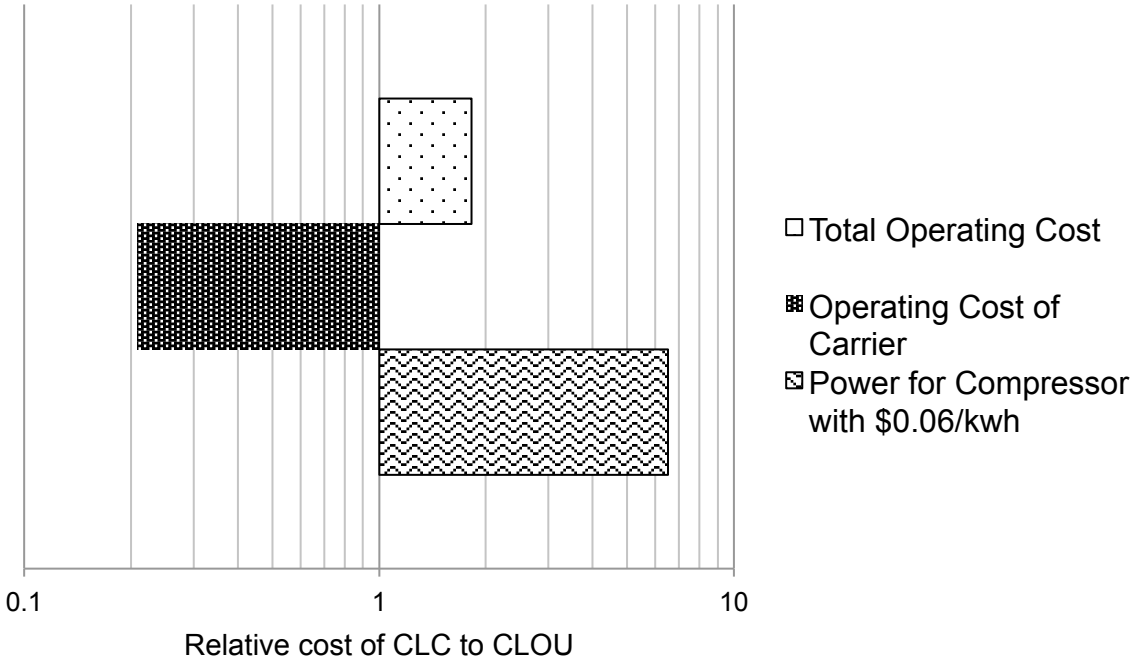

Figure 25. Relative operating costs of CLC and CLOU associated with 1, 10 and 100 MW_{th} capacity.

Subtask 5.2 – LES-DQMOM Simulation of a Pilot-Scale Fluidized Bed

This section compares the simulation results with the PSRI and NETL experimental data. We discuss the effects of the physical parameters, superficial bed velocity and bed height, on the dynamic behavior of the bed. The simulation results are time-averages of instantaneous pressure profiles collected at each time step after achieving statistically steady state. This section also discusses the modeling parameter space and effects of the particular model chosen, monodisperse, DQMOM with 3 classes, or DQMOM with 5 classes.

Case 1: Monodisperse Model Parameter

Figure 26, Figure 27 and Figure 28 show the volume fraction profiles for the monodisperse simulation for Case 1 (velocity at 0.3 m/s and height at 2.44 m) at different times. The profiles show that, as the time progresses, the bed of solids is pushed downward, decreasing its overall height and increasing the solid volume fraction near the bottom of the reactor. Figure 29 shows the comparison of experimental pressure profiles with pressure profiles obtained from simulation.

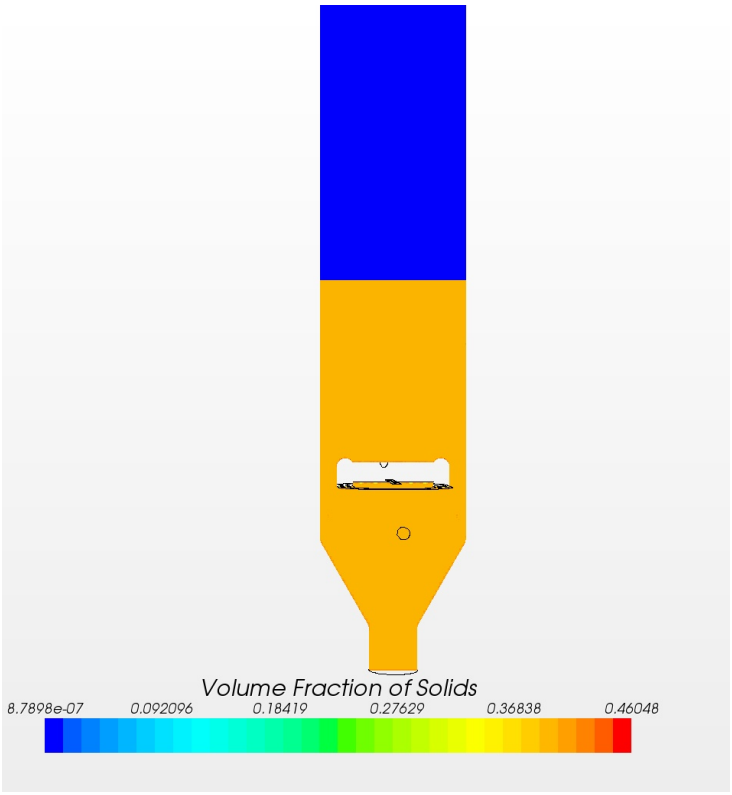

Figure 26. Volume fraction profiles for Case 1, monodisperse (v = 0.3 m/s, h = 2.44 m) at t = 0.0 s.

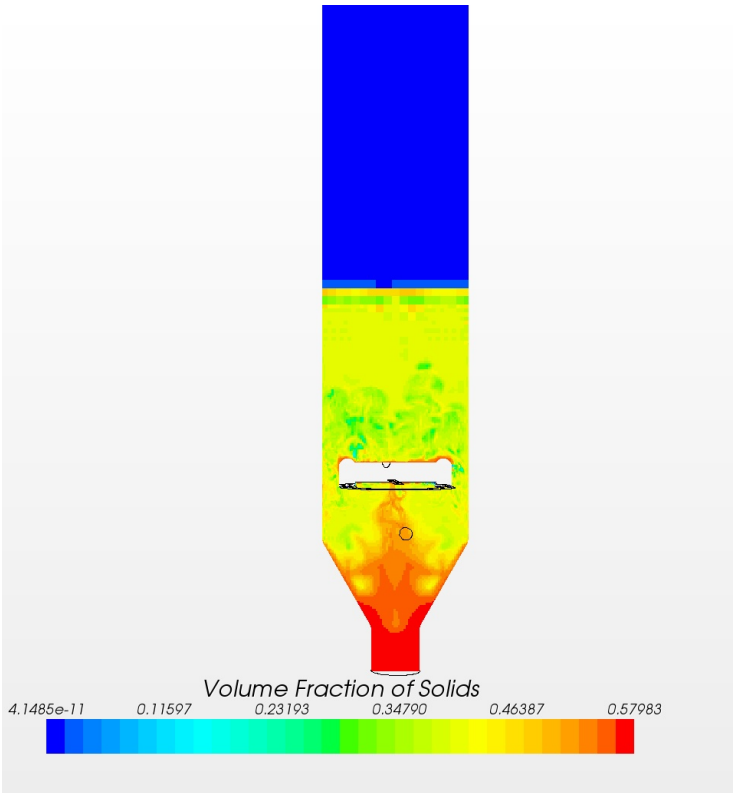

Figure 27. Volume fraction profiles for Case 1, monodisperse (v = 0.3 m/s, h = 2.44 m) at t = 2.4 s.

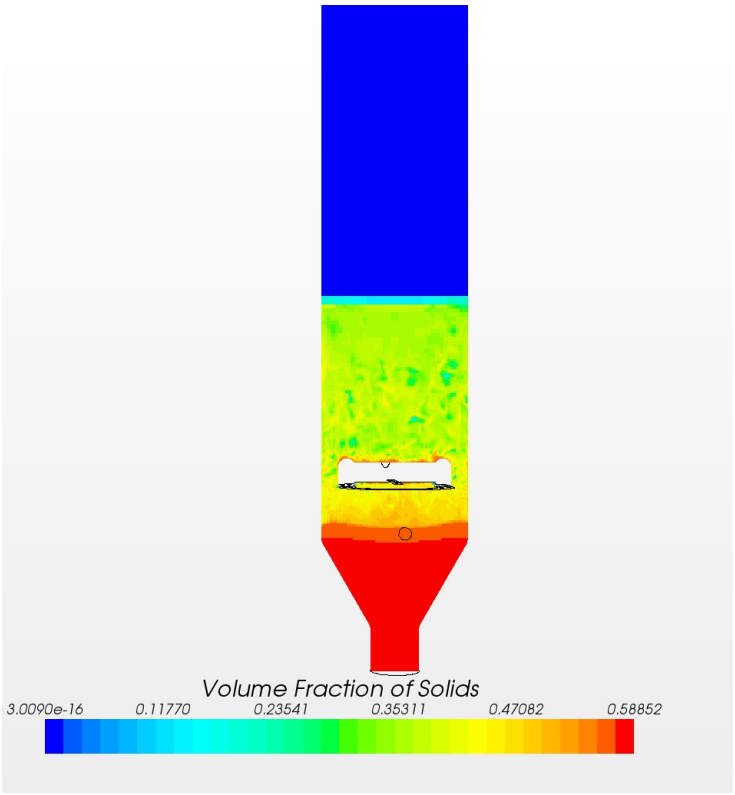

Figure 28. Volume fraction profiles for Case 1, monodisperse (v = 0.3 m/s, h = 2.44 m) t = 5.9 s.

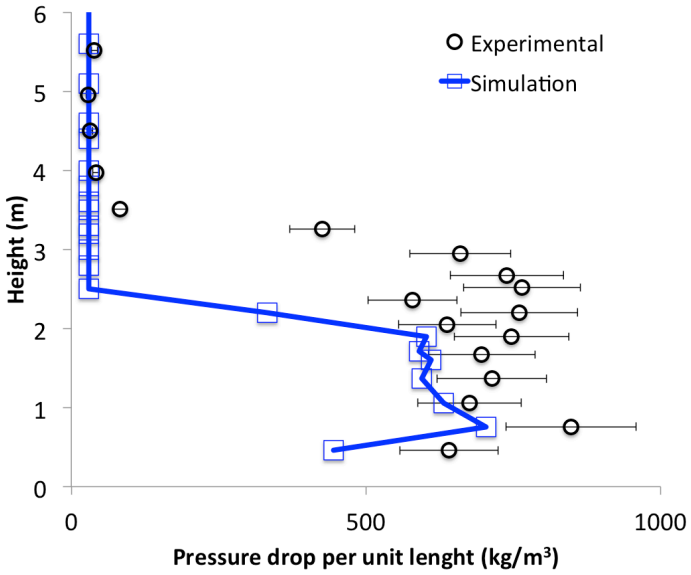

Figure 29. Time-averaged pressure drop profiles for Case 1 with monodisperse model during the first 6 seconds of the simulation.

Case 2: Monodisperse Model Parameter

Figure 30, Figure 31 and Figure 32 show the volume fraction profiles for monodisperse simulation for Case 2 (velocity at 0.3 m/s and height at 3.66 m) at different times. Once again, the majority of the particles are pushed downward as the time progresses, as in Case 1. Figure 33 shows a comparison of simulation and experimental results.

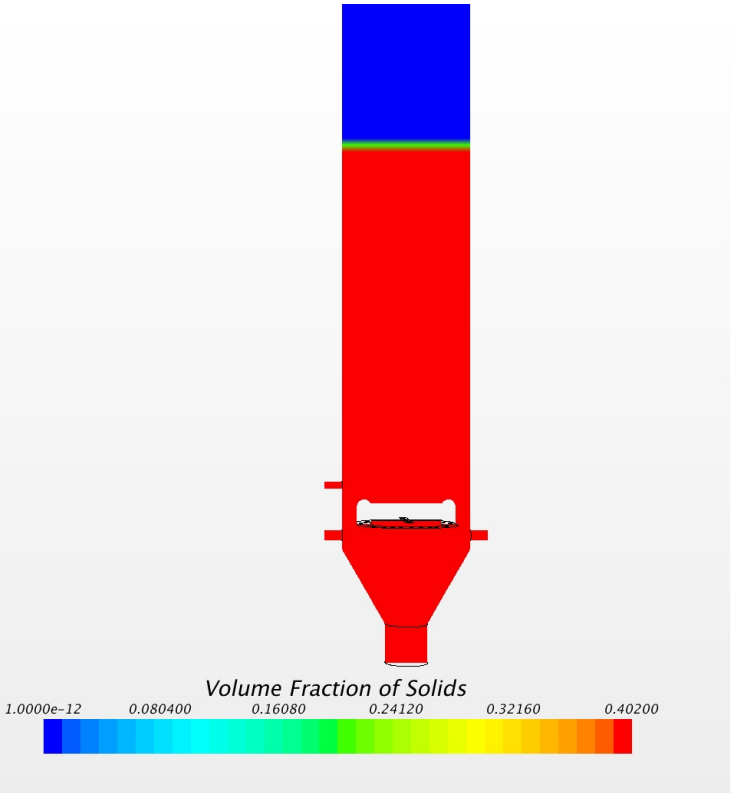

Figure 30. Volume fraction profiles for Case 2, monodisperse (v = 0.3 m/s, h = 3.66 m) t = 0.0 s.

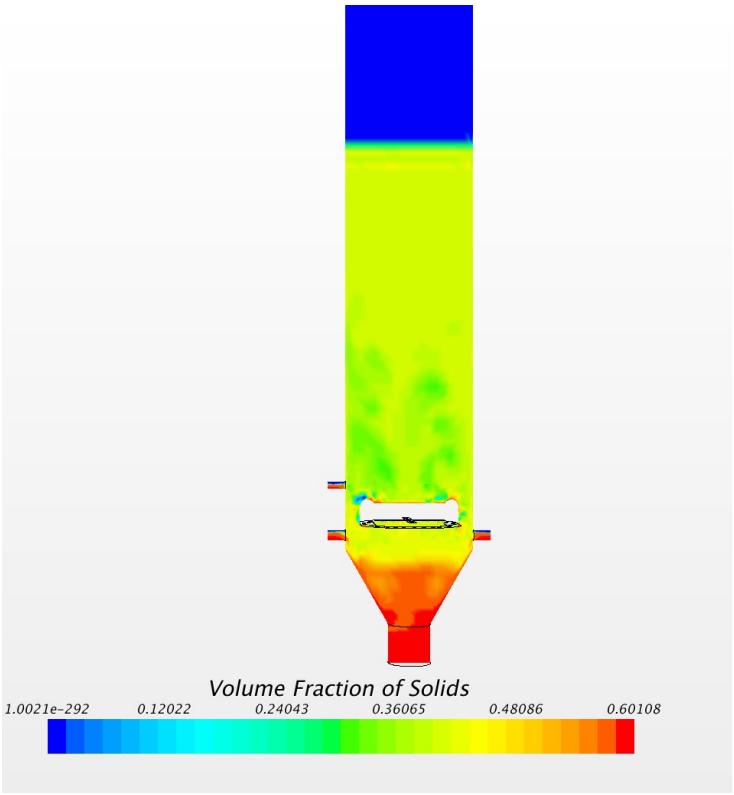

Figure 31. Volume fraction profiles for Case 2, monodisperse (v = 0.3 m/s, h = 3.66 m) t = 2.4 s.

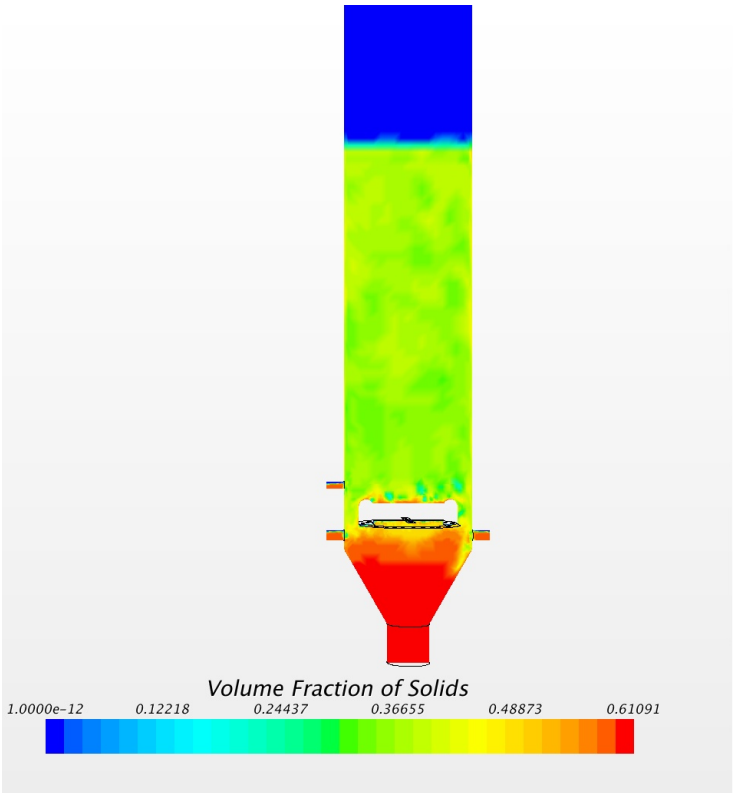

Figure 32. Volume fraction profiles for Case 2, monodisperse (v = 0.3 m/s, h = 3.66 m) t = 5.9 s.

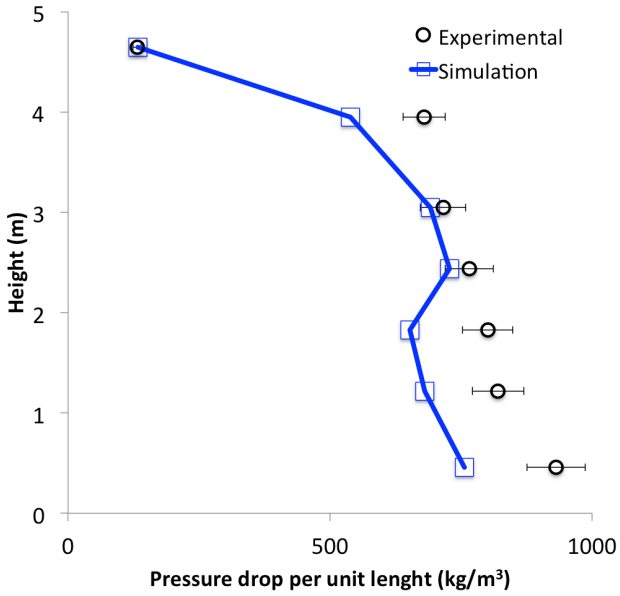

Figure 33. Time-averaged pressure drop profiles for Case 2 with monodisperse model for the first 6 seconds.

Case 3a: Monodisperse Model Parameter

Figure 34, Figure 35 and Figure 36 show the volume fraction profiles for monodisperse model simulation for Case 3a (velocity at 0.6 m/s and height at 1.22 m) at different times. The results show similar behavior as for cases 1 and 2 using the monodisperse model. Figure 37 shows the comparison of experimental and simulated pressure drop profiles.

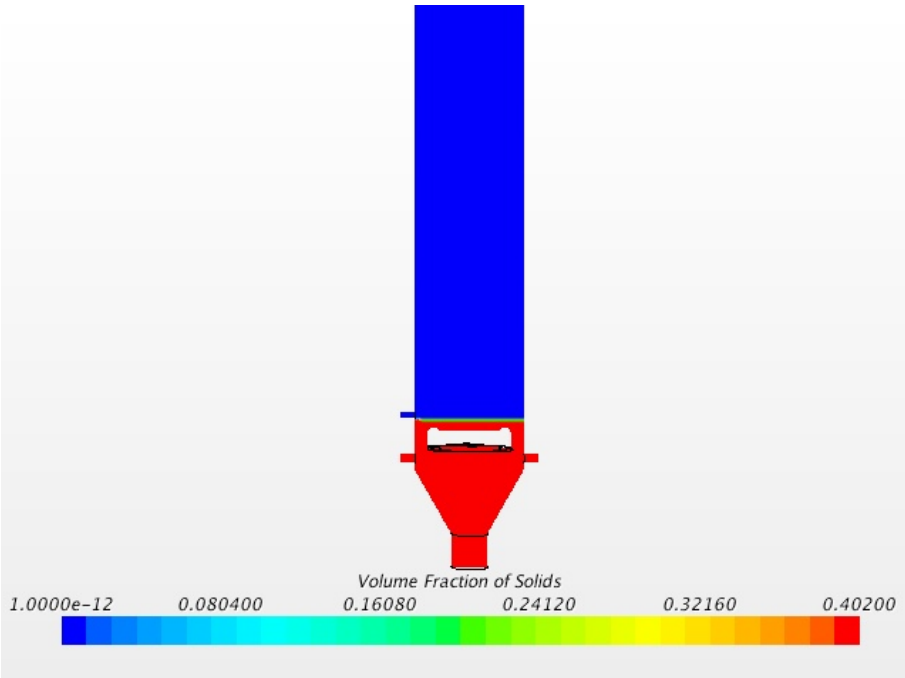

Figure 34. Volume fraction profiles for Case 3a, monodisperse (v = 0.6 m/s, h = 1.22 m) t = 0.0 seconds.

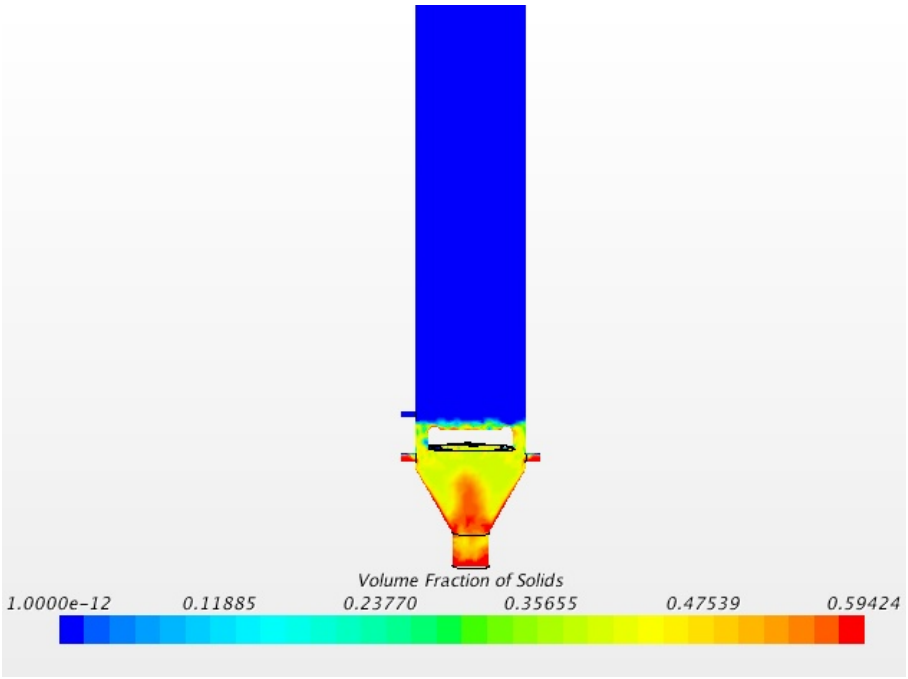

Figure 35. Volume fraction profiles for Case 3a, monodisperse (v = 0.6 m/s, h = 1.22 m) t = 1.3 seconds.

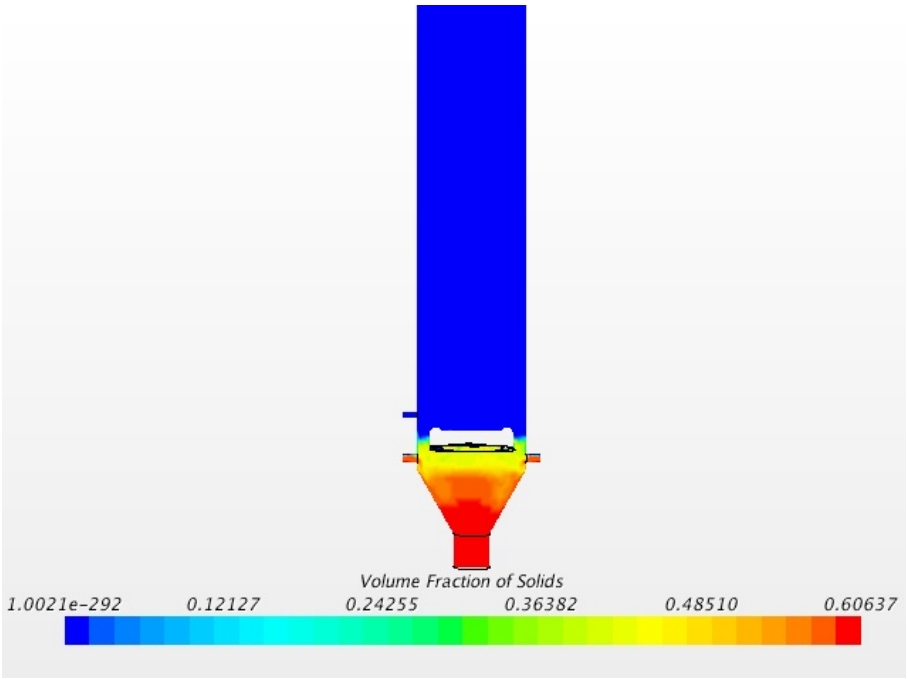

Figure 36. Volume fraction profiles for Case 3a, monodisperse (v = 0.6 m/s, h = 1.22 m) t = 4.0 seconds.

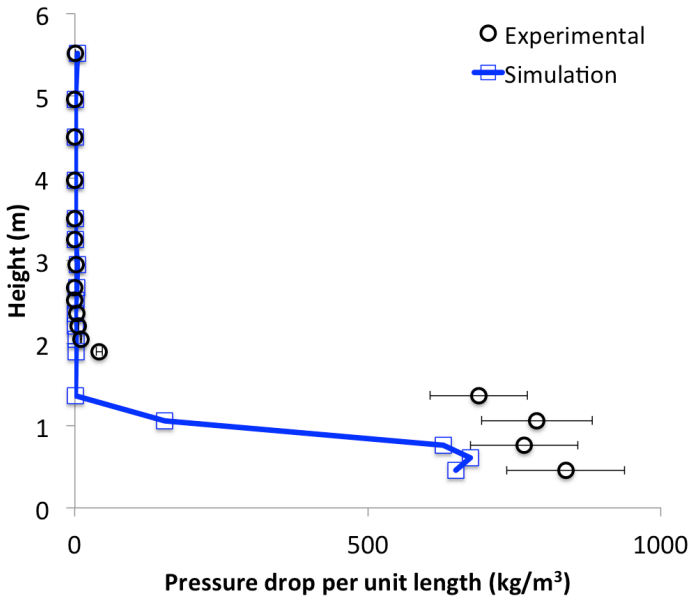

Figure 37. Time-averaged pressure drop profiles for Case 3a, monodisperse model for the first 4 seconds.

Case 3b: Monodisperse Model Parameter

Case 3b isolates the effects of superficial bed velocity. For this case, there are no experimental data available. However, decreasing the superficial bed velocity by a factor of two allows the isolation of this parameter's effects on the overall pressure drop distribution within the reactor. The results for this case, compared with Case 3a, are shown in Figure 39. It is clear that at fluidized bed height of 1.22 m, the effect of velocity on the pressure profile is negligible, at least for velocities within this range.

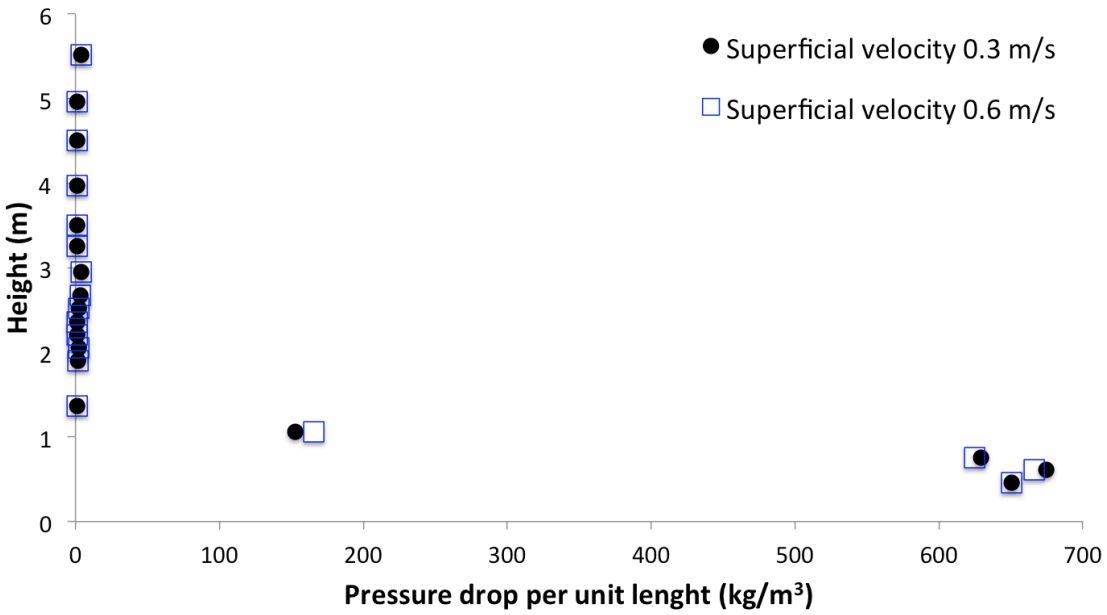

Figure 38. Effect of the superficial velocity in the fluidized bed

To analyze the effect of polydispersity and modeling parameter selection on the dynamic behavior of the fluidized bed, two scenarios are considered: the first scenario uses DQMOM case with 3 classes and the second scenario uses DQMOM technique with 5 classes as models for polydispersity. Both of these scenarios are compared to experimental Case 1.

Case 1: DQMOM Three Classes

Figure 39, Figure 40 and Figure 41 show volume fraction profiles at different times during the simulation. In these figures, the total volume fraction refers to the sum of volume fractions calculated for individual solid phases. In this case, three solid phases, or classes, contribute to the total solid fraction. Figure 42 shows the pressure drop profile compared to experimental results.

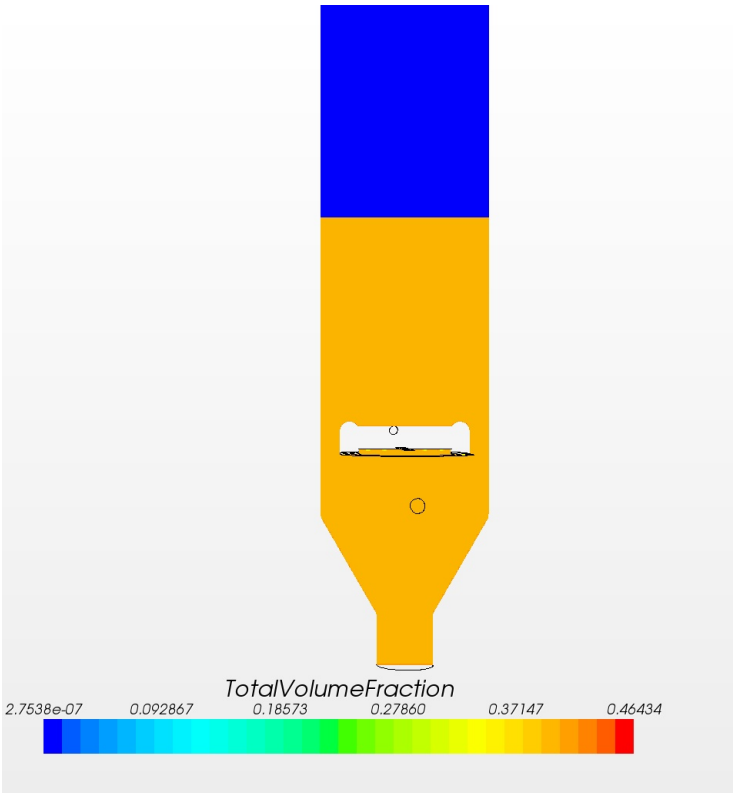

Figure 39. Volume fraction profiles, DQMOM 3 classes (v = 0.3 m/s, h = 2.44 m) t = 0.0 s.

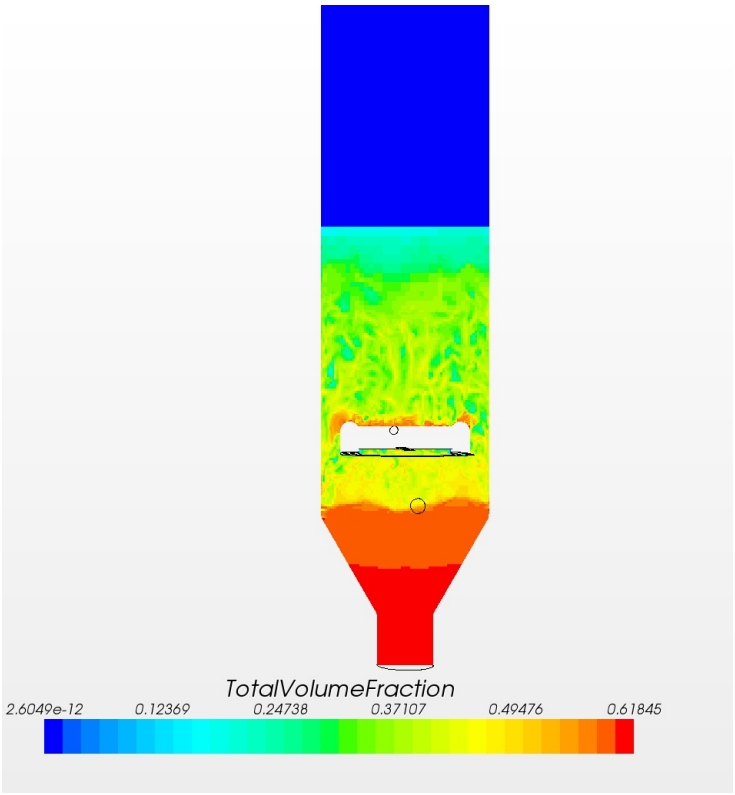

Figure 40. Volume fraction profiles DQMOM 3 classes (v = 0.3 m/s, h = 2.44 m) t = 2.0 s.

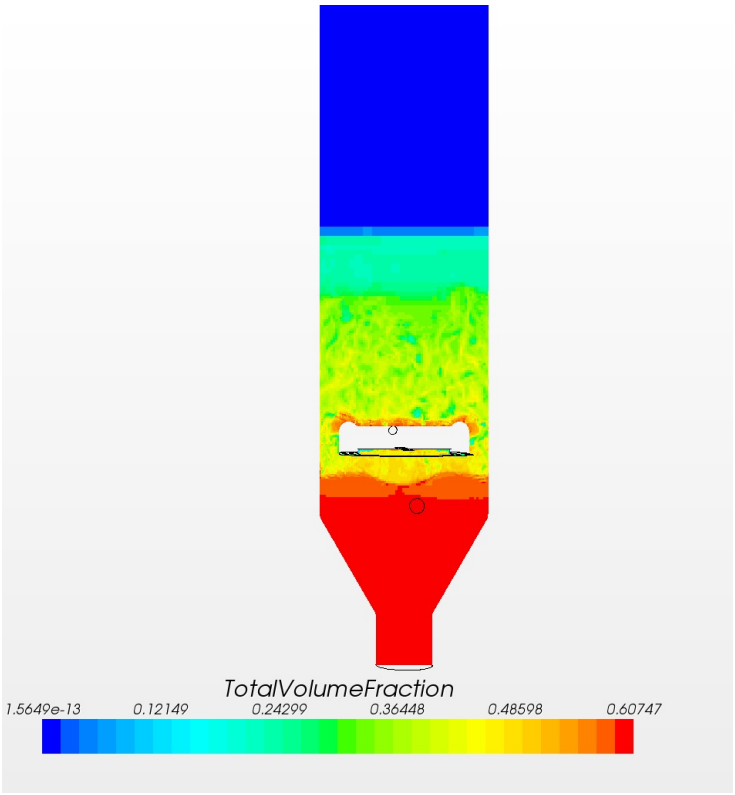

Figure 41. Volume fraction profiles DQMOM 3 classes (v = 0.3 m/s, h = 2.44 m) t = 5.7 s.

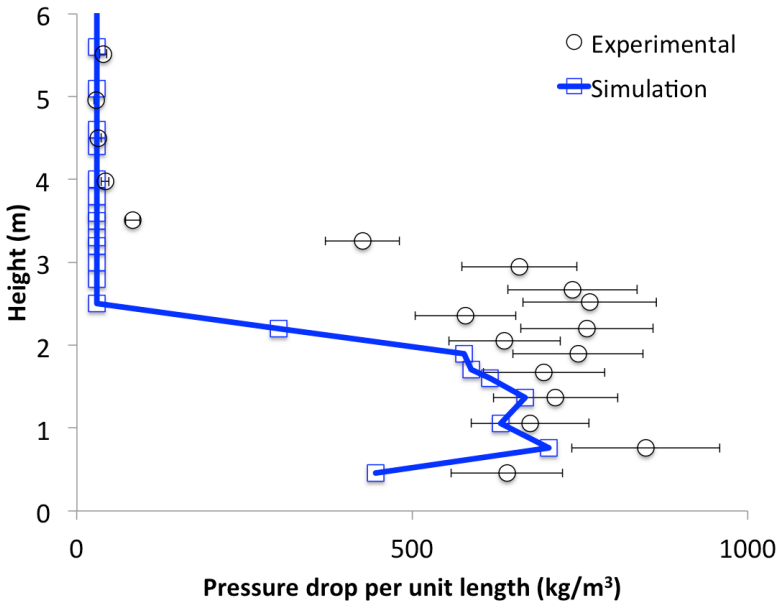

Figure 42. Time-averaged pressure drop profiles for simulation of Case 1 using DQMOM 3 classes during the first 5.7 seconds of the simulation.

Case 1: DQMOM Five Classes

Figure 43 and Figure 44 represent volume fraction profiles for the bed at different times. As before, the total volume fraction in the figures refers to the contribution of the individual phase volume fractions for each class. For this scenario, the total volume fraction is a sum of five individual volume fractions. Figure 45 shows the pressure drop behavior compared to experimental results for Case 1.

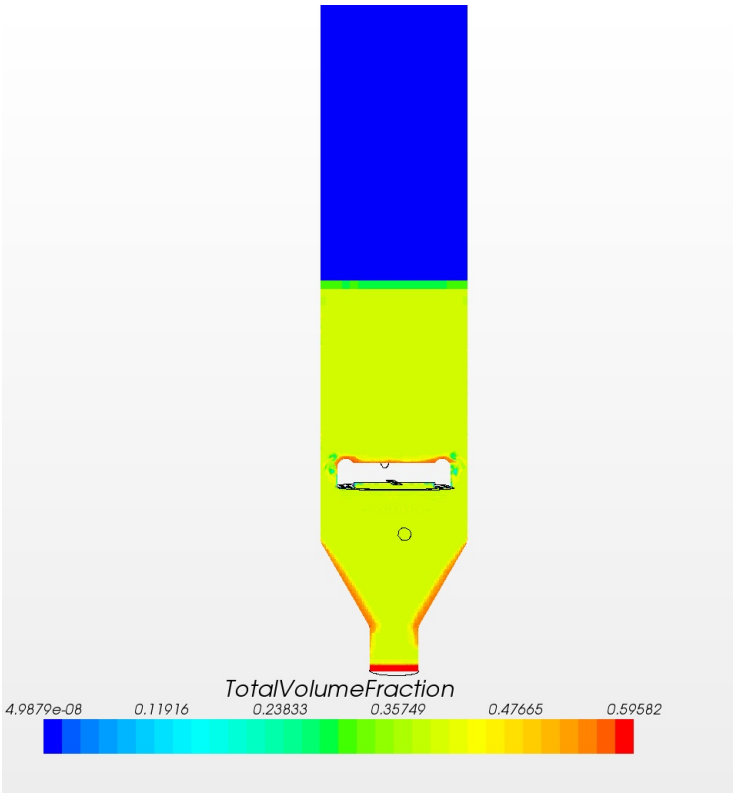

Figure 43. Volume fraction profiles DQMOM 5 classes (v = 0.3 m/s, h = 2.44 m) t = 0.1 s.

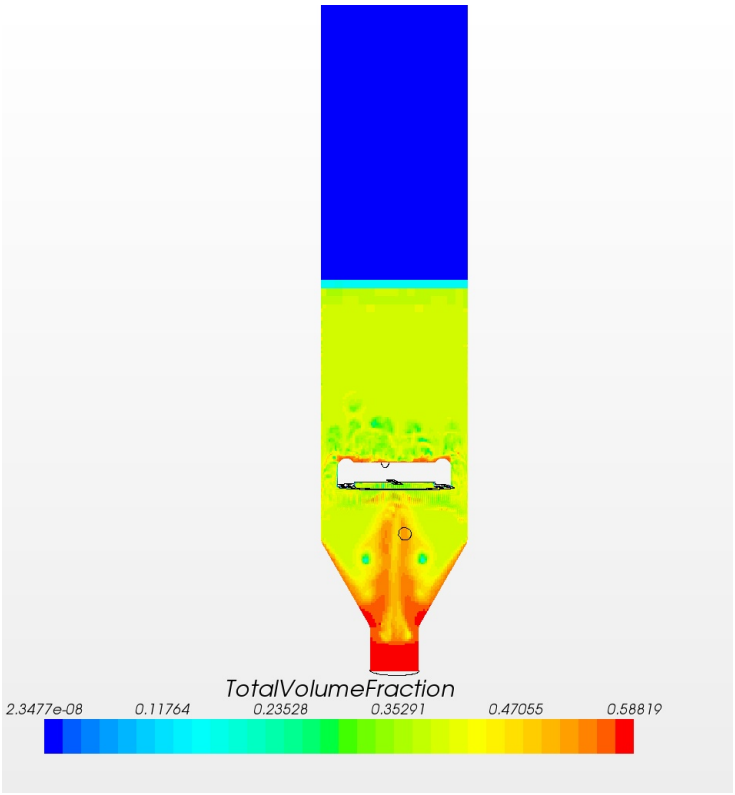

Figure 44. Volume fraction profiles DQMOM 5 classes (v = 0.3 m/s, h = 2.44 m) t = 1.6 s.

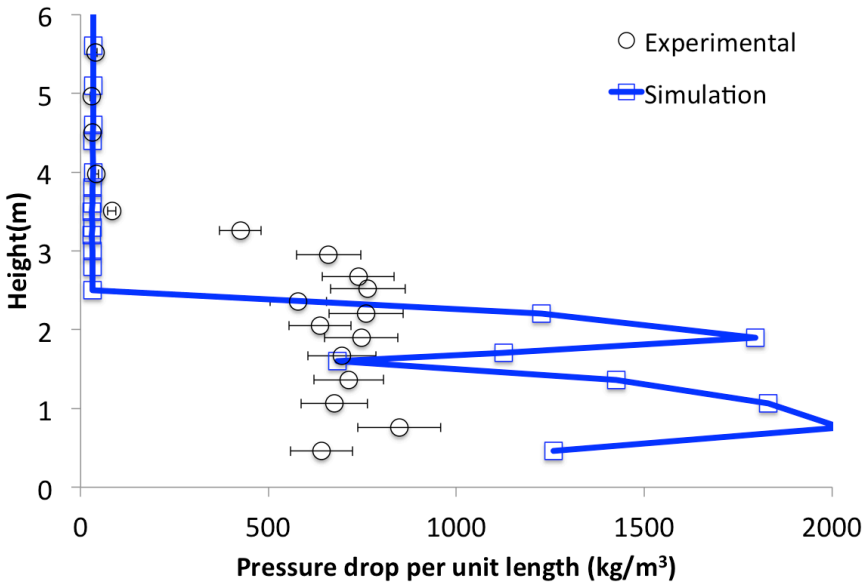

Figure 45. Time-averaged pressure drop profiles for DQMOM 5 classes, during the first 1.6 s.

General Analysis

For all scenarios using monodisperse models, trends captured by simulations agree with the experimental data. Simulations capture correct orders of magnitude, but, in general, our simulations under-predict the pressure drop profiles when compared to the experimental data, as can be seen in Figure 29, Figure 33 and Figure 37. There may be various reasons as to why our simulations do not replicate the experimental data. For instance, the drag models rely on calibration parameters, which are very hard to know a priori. Furthermore, these parameters change for different regimes of fluidization. However, it is possible to refine values for these parameters by using trial and error procedure. Restitution coefficients also represent a calibration parameter that, at best, can only be guessed from experimental data. Moreover, rotational effects were not taken into account, for which extra energy dissipation can occur in the frictional regime.

In the modeling parameter space, we observed that when we switched the model from monodisperse to DQMOM, we noticed several differences. While there was minimal difference between the monodisperse and the DQMOM model with 3 classes, there was a significant increase in pressure drop as predicted by simulation with DQMOM model with five classes. For the DQMOM model with three classes, the pressure drop in the reactor bed is under-predicted, while for DQMOM model with 5 classes, the pressure drop inside the reactor is over-predicted. This may signify a trade off between accuracy of the modeling approach (different drag model parameters for different phases) and number of solid stream classes. However, both DQMOM simulations are very computationally intensive, especially simulations using the DQMOM model with five classes. While these results were advanced as far as possible, there may be temporal effects, which were not resolved during the simulation time.

Previously computed simulations of the PSRI and NETL BFB as shown by Shadle et. al. (2011), serve as a good point of comparison. Figure 46, Figure 47 and Figure 48 show side-by-side comparisons of our results and modeling results presented by Shadle for Case 1, Case 2, and Case 3a, as described in Table 7. These figures show that our simulations perform very well in comparison to modeling work presented by Shadle. They clearly capture the proper general behavior of the fluidized bed and are able to capture more of the physical behavior seen in the experiments than most of the previous models. This especially applies to Case 2 and Case 3.

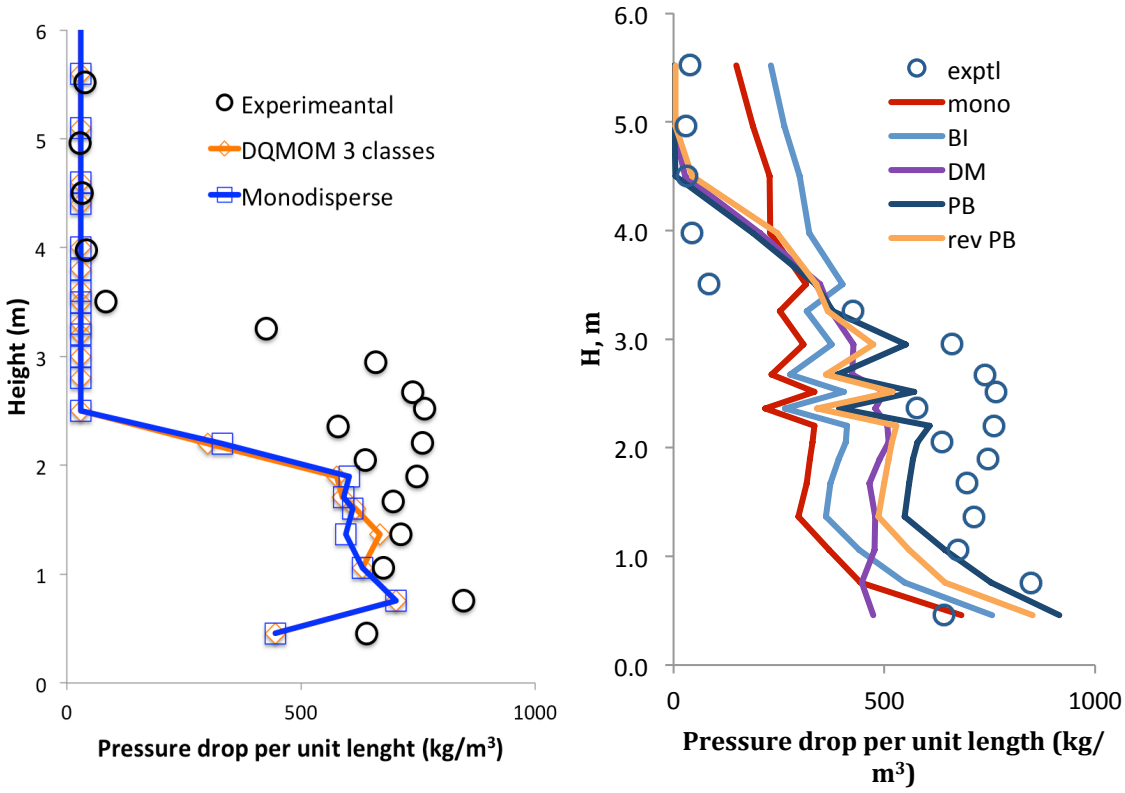

Figure 46. Direct comparison of simulation results carried out by PSRI-NETL (Shadle, et al. 2011) and simulation results in this study for Case 1 monodisperse and Case 1 DQMOM with 3 classes.

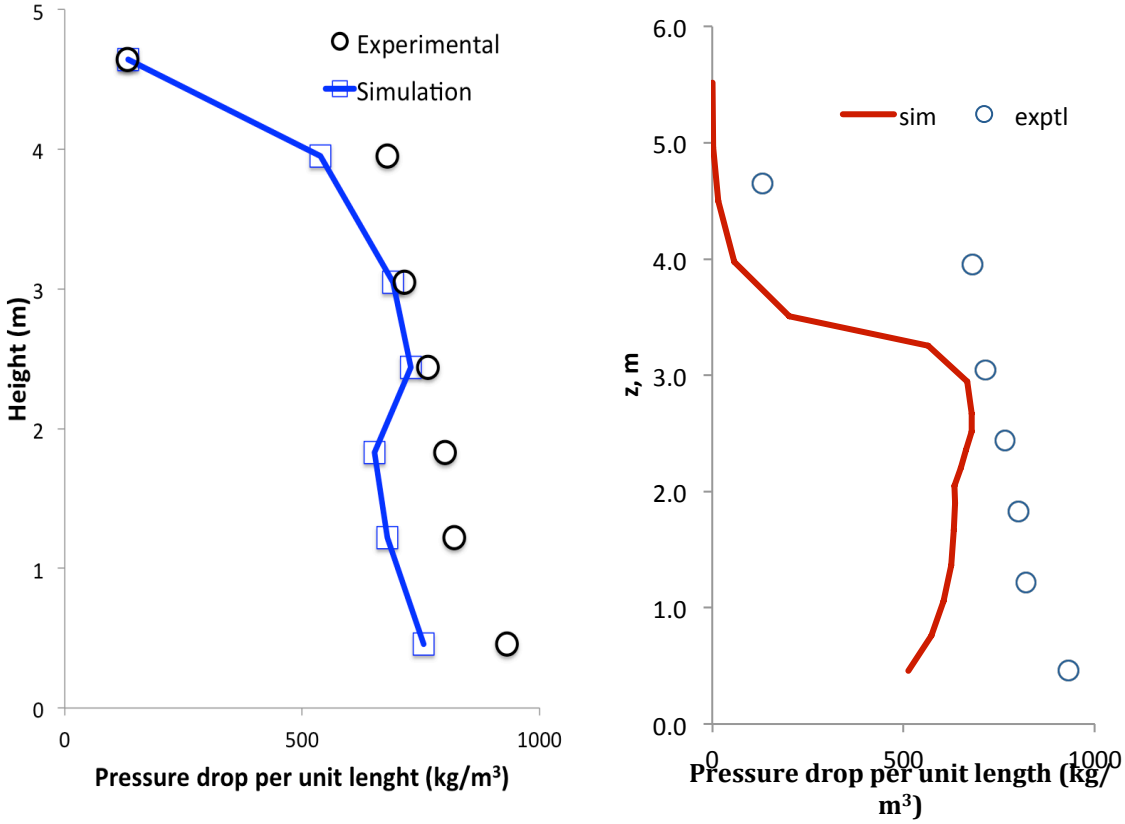

Figure 47. Direct comparison of simulation results carried out by PSRI-NETL (Shadle, et al. 2011) and simulation results in this study for Case 2 monodisperse.

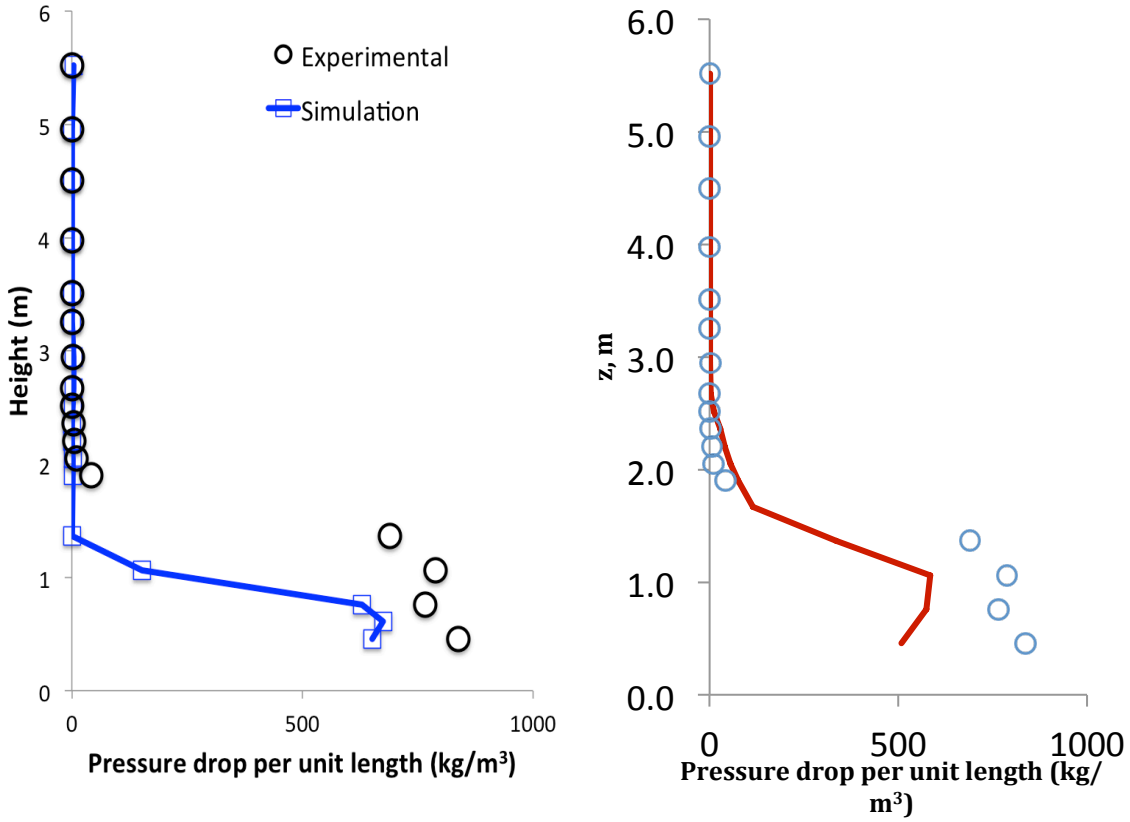

Figure 48. Direct comparison of simulation results carried out by PSRI-NETL (Shadle, et al. 2011) and simulation results in this study for Case 3a monodisperse.

Effects of Physical and Modeling Parameters

To evaluate the effects of variations in the physical parameter space on the pressure profile inside the reactor, simulations representing Case 1, Case 2, Case 3a and Case 3b were run while fixing the model parameter space to the monodisperse model. Although our simulation results using the monodisperse model compare well to the experimental data as well as previous modeling work, it is important to note that this also signifies that our simulations using the monodisperse model are able to capture temporal and spatial effects associated with evolution of the bubbling bed for different bed heights and different fluidization velocities.

The fluidization state happens when a stationary bed of solids is injected with fluidization gas with enough velocity to break up the bed. The stationary bed is dominated by gravity forces (particle weight and bed weight and height) that make the bed immobile. When a critical gas velocity is reached (minimum fluidization velocity), particles start floating and moving randomly, increasing the frequency of collisions, all while a fluidization state is reached. Further increase in the gas velocity increases movements of the bed and the mean distances between particles, but the pressure no longer increases, as graphically shown in Figure 49. Further increase in the gas velocity only transports particles along the

reactor length. When the minimum fluidization state is reached, there is a balance between drag forces and gravity forces acting on the particles.

This is shown in simulation results using the monodisperse model for Case 1 and Case 2. The only difference between the two cases is bed height; the superficial bed velocity is kept constant. As the bed height increases, this also changes the fluidization velocity. For Case 1, as shown in Figure 29, the pressure profile is very chaotic, while for Case 2, shown in Figure 33, the pressure drop profile is much smoother.

Previous studies, such as done by Mele (2011), have also studied the effect of bed height on the bed fluidization, quartz sand in this specific case. Figure 50 shows his results. For his case, around gas velocities of 4 m/s, the 65 mm bed is transitioning from stationary to a fluidized state characterized by chaotic random movement. At the same velocity of 4 m/s, the other two beds at larger bed heights, did not yet enter the transition state. For the experimental BFB cases we are simulating, this translates into a chaotic pressure profile for the lower bed height, Case 1, and smoother pressure profile for the taller bed height, Case 2.

On the other hand, when a fully fluidized stated is reached for the same respective bed height, increasing the velocity has little or no effect on the pressure drop profiles. For instance, for a bed height of 65 mm shown in Figure 50, the pressure drops stays nearly constant between gas velocities of 4 m/s and 6 m/s. Case 3b was added to our sensitivity analysis space to determine whether our simulations can capture this behavior. Comparing simulation results using the monodisperse model for Case 3a and Case 3b shows that our simulations predict almost identical pressure drops for the two different fluidization velocities. This agrees with data published in the literature for non-reactive cases.

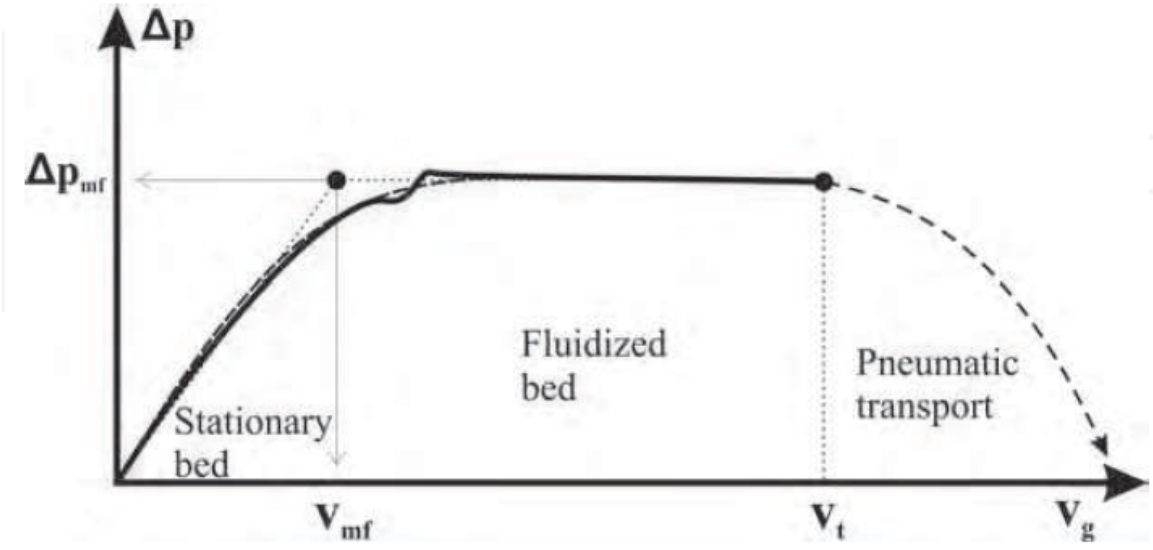

Figure 49. Relationship between pressure drop and gas velocity for a polydisperse bed (Kunii and Levenspiel 1991).

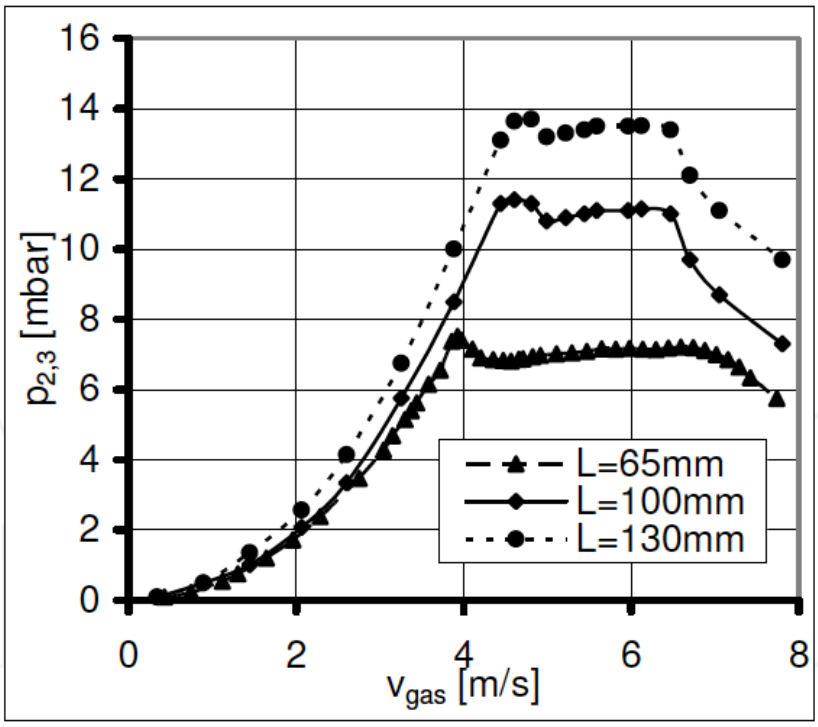

Figure 50. Effect of height for quartz sand fluidization (Mele, 2011).

Computational Costs

Computational effort required for each simulation case varied. Because of the simplicity of the model, simulations using the monodisperse model were the most computationally efficient, with simulation representing Case 1 with the complete geometry using the least amount of computational resources. For this case, it took about 15 hours of computational time on 48 cores to simulate 1 second of physical time. Even though the mesh cell count for Case 1 using the monodisperse model was larger than mesh cell count for cases 2, 3a, and 3b, 2.3 million versus 700,000, respectively, the required time step to achieve stable and well converged solution was two orders of magnitude smaller for the reduced geometry than for the complete geometry. This, ultimately, increased the computational effort required to complete simulations for cases 2, 3a and 3b. Initially, the investigators reduced the geometric representation of the system to decrease the computational effort, although, ultimately, the final result was the opposite of what was expected. Nonetheless, computational efforts required for simulations using the monodisperse model were very minimal in comparison to computational efforts required for simulations using the DQMOM model with three classes, and especially for simulations using the DQMOM model with five classes. The DQMOM model with five classes was the most computationally intensive job, with computational costs three orders of magnitude greater than computational costs required for simulations using the monodisperse model, all for simulations of Case 1 using the complete geometry. Simulations using the DQMOM model with 5 classes were run on anywhere between 480 and 600 computing cores, with computational times on the order of days to capture just 1 second of physical time.

Subtask 5.3 – Lab-Scale CLC Studies

This subtask focused on acquiring data in the laboratory that would useful for scale-up of CLC technology, in particular copper-based CLOU. This was achieved through four studies:

- Measurement and modeling of O_2 release rates by reduction of CuO in the fuel reactor
- Measurement and modeling of Cu_2O oxidation in the air reactor
- Evaluation of coal conversion by copper-based CLOU
- Evaluation of attrition rates for various copper-based carriers

Measurement and Modeling of O_2 Release by Reduction of CuO

The ambition with this study was to determine whether it is possible to describe O_2 release with a universal chemical kinetic expression of the conventional form:

$$rate = A\exp(-E_a/RT)[\mathrm{CuO}]^{\alpha}\left(P_{O_{2,eq}} - P_{O_2}\right)^{\beta}$$

where A is a preexponential factor, E_a is the activation energy, R is the gas constant, T is temperature, P_{O2} is the system's partial pressure of oxygen, $P_{O2,eq}$ is the equilibrium partial pressure of oxygen at the system's temperature and α and β are reaction orders. The objective was to determine the constants A, Ea, α and β. This is complicated by the fact that both the equilibrium oxygen partial pressure $PO_{2,eq}$ and the intrinsic reaction rate are affected by temperature. The equilibrium diagram for the Cu_2O/CuO system is shown in Figure 51.

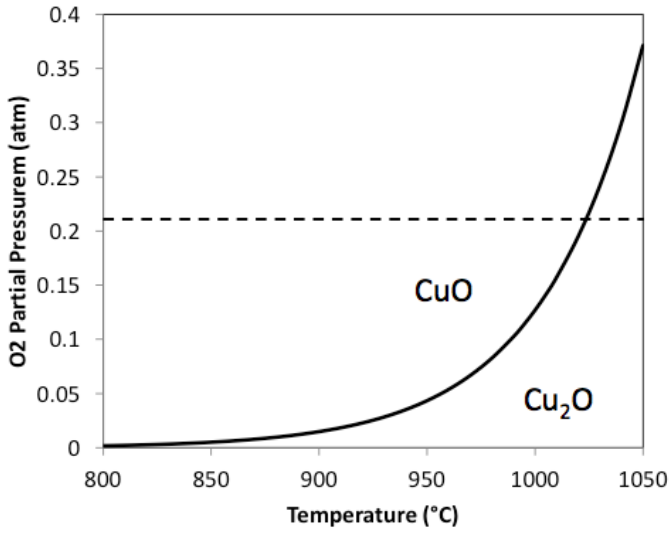

Figure 51. Equilibrium partial pressure of oxygen for the Cu_2O/CuO system. The partial pressure of oxygen in air is displayed with a dashed line.

Several series of experiments were performed using the TGA, in which the oxygen partial pressure and sample temperature can be precisely controlled. In one series of experiments, temperature was varied to determine the overall influence of temperature on reaction rate. In another, the supplied oxygen partial pressure was varied as well as temperature to keep the same thermodynamic driving force ($P_{O2,eq} - P_{O2}$) throughout the temperature range (Table 14).

Table 14. Experimental conditions for excluding the influence of oxygen driving force on the rate of reaction at different temperatures.

Experiment number	Temperature (°C)	Equilibrium O_2 part. press. (atm)	Supplied O_2 part. press. (atm)	O_2 "driving force" (atm)
1	785	0.0412	0.0012	0.040
2	855	0.0446	0.0056	0.040
3	885	0.051	0.011	0.040
4	923	0.064	0.024	0.040
5	976	0.116	0.076	0.040

The resulting conversion-versus-time curves for one of the carriers are presented in Figure 52. Similar curves were found for the other carriers tested.

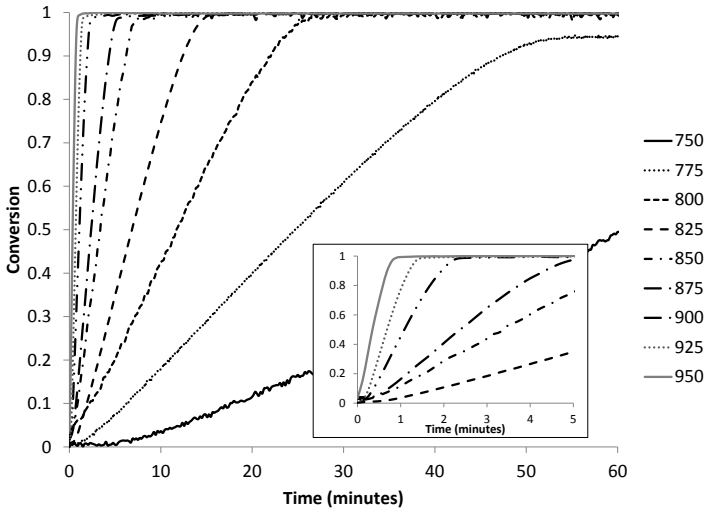

Figure 52. Conversion vs. time for the decomposition of CuO under an N_2 atmosphere in TGA at various temperatures using 45_CuO_ZrO2_FG. Inset shows blow-up of the time interval from 0 to 5 minutes.

The rate of oxygen release can be determined from the TGA data with the following expression.

$$r = -\frac{dm}{dt}\frac{1}{m_{Cu}}$$

where *dm/dt* is the rate of mass loss due to oxygen release. The rate is normalized by dividing by the mass of copper in the sample. Using the resulting rates of oxygen release at 50% conversion for experiments in pure nitrogen, an Arhennius plot was developed to determine the activation energy, E_a. The apparent activation energy varied from 264 to 284 kJ/mol. However, this resulted from a combination of the intrinsic rate and the influence of oxygen driving force on the rate. The measured activation energy resulting from the experiments in Table 14 was quite different, as seen in Figure 54. The resulting range, from 58 to 67 kJ/mol, is considered the intrinsic activation energy of CuO decomposition.

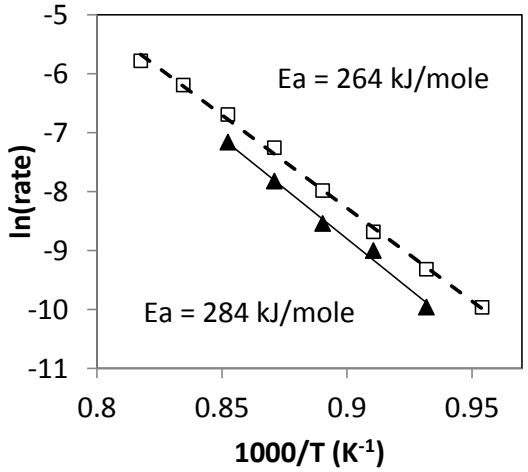

Figure 53. Arrhenius plot for decomposition of CuO in 45_ZrO2_FG and 50_TiO2_MM. The apparent activation energies are calculated to be 264 kJ/mole and 284 kJ/mole for the zirconia and titania-supported materials, respectively.

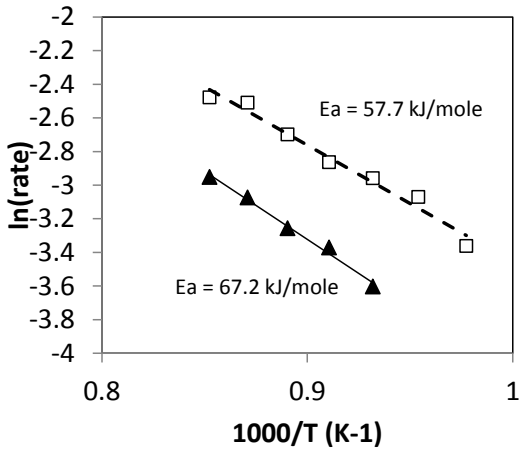

Figure 54. Arrhenius plot for the decomposition of 45_ZrO2_Fg and 50_TiO2_MM. This data attempts to separate the dual effect of temperature on the kinetic equation (i.e. influence on the activation energy and driving force) thereby generating the corrected activation energies for both materials.

Reaction Order with Respect to CuO. The order for cupric oxide, α, was determined by analyzing the shape of the mass loss curve. The reaction may be determined graphically to be either zero, first or second order in CuO by integrating the rate expressions and plotting the term for concentration of CuO of the integrated rate expression versus time and identifying if any yield a straight line. If the reaction were zero order in CuO concentration (represented by [CuO]), the rate of CuO consumption, d[CuO]/dt, would be constant, resulting in the following relation for [CuO] as a function of time:

$$[\mathrm{CuO}] = Ct$$

where C represents a constant. Thus, if the reaction were zero order in CuO, a plot of [CuO] versus time would yield a straight line. Similarly, the rate expressions for first and second order in CuO concentration,

$$\frac{d[\mathrm{CuO}]}{dt} = C[\mathrm{CuO}]$$

and

$$\frac{d[\mathrm{CuO}]}{dt} = C[\mathrm{CuO}]^2$$

respectively yield, upon rearrangement and integration,

$$\ln[\mathrm{CuO}] = Ct$$

and

$$\frac{1}{[\mathrm{CuO}]} = Ct$$

So a first-order reaction would yield a straight line if *ln*[CuO] were plotted versus time, and a second

order reaction would produce a straight line if 1/[CuO] were plotted versus time. The CuO concentration terms for zero, first and second order are [CuO], ln[CuO] or 1/[CuO], respectively. Data from the 800°C and 900°C tests is plotted as [CuO], ln[CuO] and 1/[CuO] in . As can be seen in the plots, the reaction order in CuO concentration appears to be approximately zero.

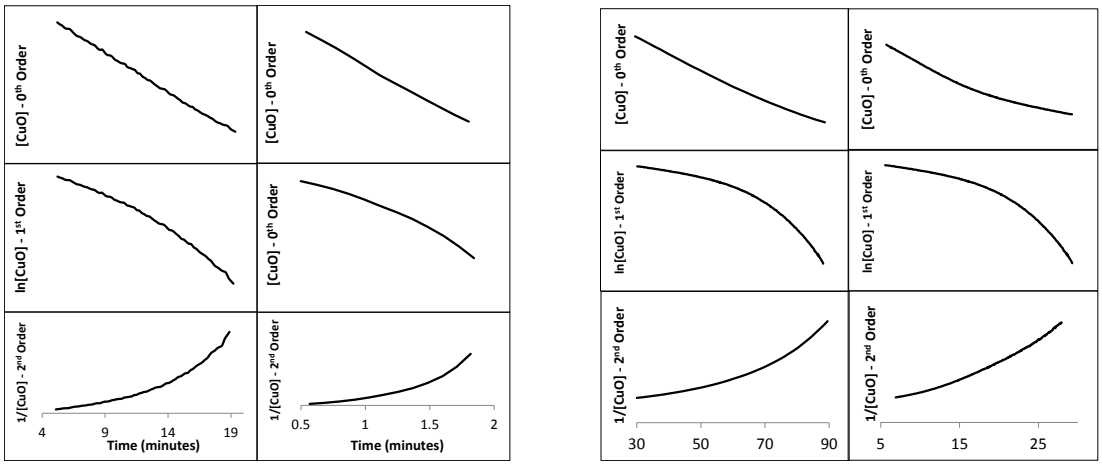

Figure 55. Plots to determine the order of reaction with respect to CuO for the 45_ZrO2_FG material (left pair) and 50_TiO2_MM (right pair). Within each pair the left figures are for 800°C and the right figures are for 900°C. Top to bottom represent zero, first and second order. The shapes suggest the reaction to be zero order in CuO.

Reaction Order with Respect to Oxygen Driving Force

In industrial-scale fuel reactors where the bed material may be several feet deep, oxygen released from the particles may create an appreciable oxygen partial pressure either locally or in regions of little fuel. This in turn will reduce the driving force for decomposition, which may slow the decomposition rate. The tests outlined in Table 15 were used to isolate the influence the oxygen driving force has on the decomposition reaction and to determine the reaction order with respect to oxygen partial pressure, β. By holding the temperature constant and supplying a partial pressure of oxygen lower than the equilibrium partial pressure, decomposition still proceeds from CuO to Cu_2O.

Table 15. Experiments to isolate the influence of O_2 "driving force" on kinetics of CuO decomposition.

Experiment number	Temperature (°C)	Equilibrium O_2 part. press. (atm)	Supplied O_2 part. press. (atm)	O_2 "driving force" (atm)
1	950	0.045	0.00	0.045
2	950	0.045	0.020	0.025
3	950	0.045	0.034	0.011

Using thermogravimetric analysis Wen et. al (2012) verified the equilibrium partial pressure of oxygen versus temperature for CuO/Cu_2O in the range of $600 < T < 950$°C calculated by performing a Gibb's energy minimization. An exponential regression curve was fit to the equation reported by Wen et. al. with a coefficient of determination (R^2) value of 0.999. The regression curve used in this work for the equilibrium partial pressure of oxygen was:

$$P_{O_2}(atm) = 6.057\times10^{-11}e^{0.02146\,T}$$

where *T* is in units of degrees Celsius. Figure 56 displays the decomposition of 45_ZrO2_FG as well as 50_TiO2_MM at 950°C under three different oxygen partial pressure atmospheres (0 atm, 0.020 atm and 0.034 atm). It is clear that as the supplied partial pressure of oxygen increases, thus reducing the thermodynamic driving force, both the reaction rate and extent of reaction decrease. The reaction rate was extracted from a portion of the curve where the reaction appears to be progressing most quickly from the data obtained with PO_2 of 0.020 atm. The order of reaction with respect to oxygen driving force was calculated to be 1.01 for 45_ZrO2_FG material. A similar analysis of the 50_TiO2_MM material resulted in an identical reaction order of 1.0. The reaction therefore appears to be first order in ($P_{O2,eq} - P_{O2}$).

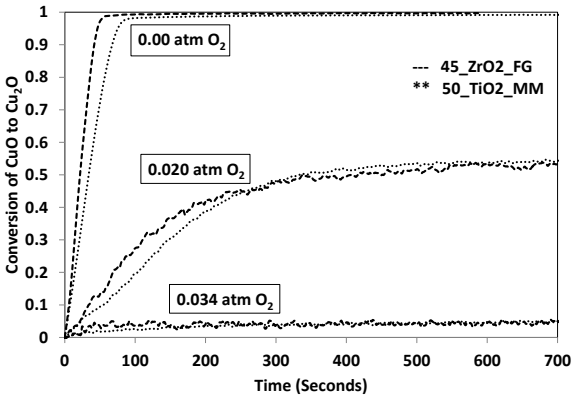

Figure 56. Decomposition of CuO at 950 °C under 3 different supplied oxygen pressures (0.00, 0.020 and 0.034 atm) for both the zirconia- (--) and titania-supported (**) carriers.

Preexponential Factor

After the other values had been determined the preexponential constant *A* was calculated. For the corrected activation energies it was determined to be 4.15×10^{-4} and 3.64×10^{-4} for the titania and zirconia materials, respectively. It was then determined that 3.90×10^{-4} gave the best fit to both sets of data.

Overall Expression for Rate of CuO Decomposition

Decomposition rates for the two materials were slightly different. Average values of the two materials were used to form a general rate expression, which predicts the mass release rate of oxygen, per mass of copper (Cu) in the carrier, as a function of temperature and oxygen partial pressure:

$$rate\left(\frac{g}{s}\frac{1}{g_{Cu}}\right) = 3.90 \times 10^{-4} \exp\left(-\frac{62000}{\mathrm{R}\times\mathrm{T}}\right)\left[p_{O_2,eq} - p_{O_2}\right]$$

where *T* is in units of Kelvin and pressure is in units of atmospheres.

The temperature dependency of $P_{O2,eq}$ modeled by the expression of Wen (2012) given above can be incorporated into this model to present an expression for rate solely as a function of temperature and surrounding O_2 partial pressure:

$$rate\left(\frac{g}{s}\frac{1}{g_{Cu}}\right) = 3.90 \times 10^{-4}\exp\left(-\frac{62000}{\mathrm{R}\times\mathrm{T}}\right)\left[6.057\times10^{-11}exp^{0.02146\times(T-273)} - p_{O_2}\right]$$

This expression represents the final product of this study. Figure 57 compares the model presented above with rates obtained from experimental data from the titania- and zirconia-supported oxygen carriers tested over the temperature range 800 to 950°C. It also compares models derived using the two different activation energies. The model clearly does a good job predicting the rate of decomposition, and is considered suitable for modeling and scaling the fuel reactor of a copper-based CLOU system.

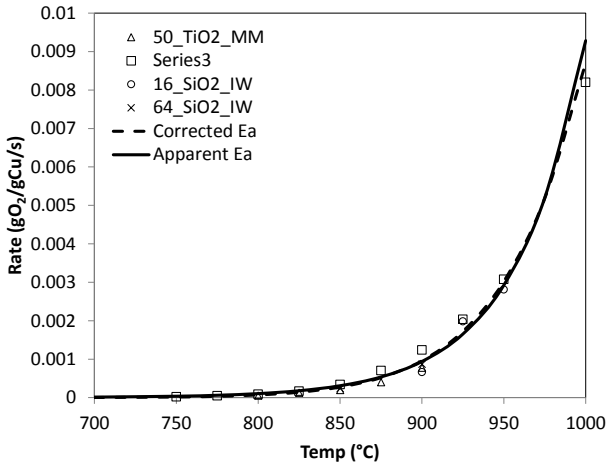

Figure 57. Reaction rate versus temperature for 4 different CuO-based oxygen carriers in TGA at four different temperatures along with the rates predicted by the rate expression determined in this study.

Measurement and Modeling of Oxidation of Cu_2O to CuO

Modeling the oxidation of Cu_2O to CuO (Cu_2O + ½ O_2 → 2 CuO) is challenging when trying to take into consideration all factors that influence the rate. As with the case of CuO decomposition described above, the dual influences of changing intrinsic kinetics and oxygen partial pressure driving force with temperature make experimentation and associated analysis challenging. The same type of approach of varying oxygen partial pressure simultaneously with temperature to maintain oxygen driving force was used for this study.

Influence of Oxygen Partial Pressure

Figure 58 represents the conversion profiles obtained during the oxidation of Cu_2O on the 45_ZrO2_FG material at 825°C and various oxygen partial pressures. This set of experiments was used to determine

the influence the partial pressure of oxygen has on the reaction kinetics of Cu_2O oxidation. If it is assumed that the function, $f(p_{O_2})$, assumes the following form (common among reversible reactions):

$$f(p_{O_2}) = (p_{O_2}^{\alpha} - p_{O_2,eq}^{\alpha})$$

then the result obtained from analysis of data used in Figure 58 yields α=1.3. That exponent is used in subsequent analysis of oxidation rates.

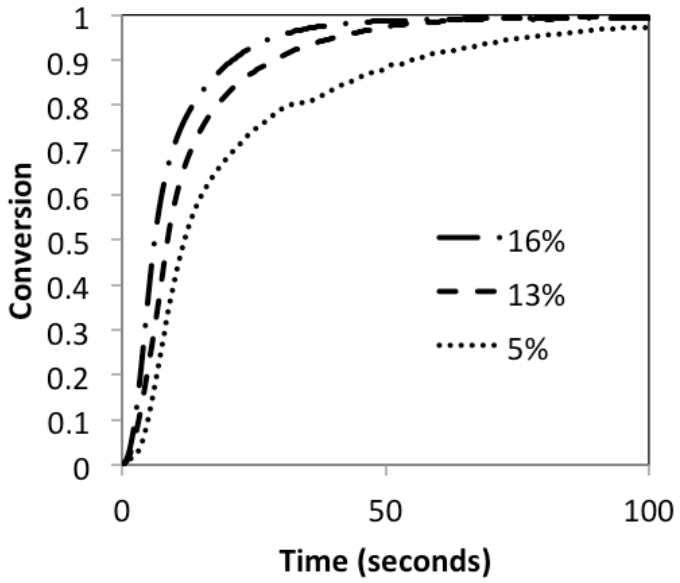

Figure 58. The influence, $f(p_{O_2})$, for the oxidation of Cu_2O powder is identified by varying the supplied partial pressure of oxygen during the oxidation cycle of chemical-looping using a zirconia-based supported oxygen carrier.

Influence of Degree of Conversion

For the oxidation of Cu_2O to CuO the conversion versus time profile is given in Figure 59. It has been determined that, especially at the lower temperatures, the data do not express well as any simple zero-, first- or second-order function.

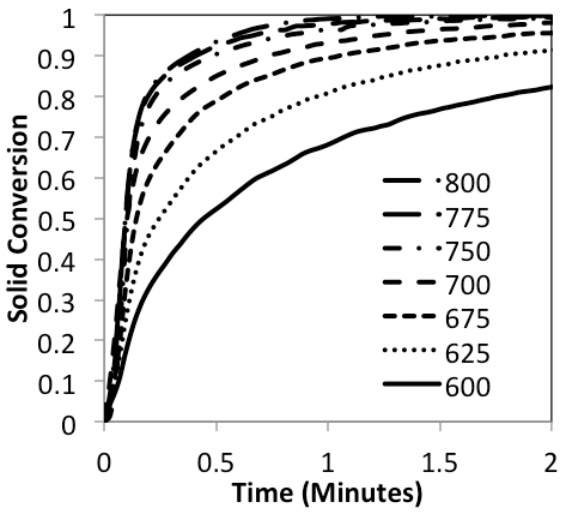

Figure 59. Conversion profile for oxidation of 45_ZrO2_FG material at temperatures from 600°C to 800°C.

Zhu et al. (2004) suggested that at low temperatures the oxidation of cuprous oxide followed a logarithmic rate law and the resulting activation energy was 38 kJ/mol which compares very well with the value reported here obtained using the constant driving force approach. These authors suggested that while the logarithmic rate law held true at low temperatures (up to 800°C), the apparent activation energy became very small or negative at higher temperatures. As has been reported earlier, this decrease in rate at high temperature is due to a decrease in oxidation driving force associated with lower equilibrium partial pressure of oxygen. During their discussion several theories for the logarithmic characteristics of the oxidation rate at low temperature were dismissed including (1) electric fields developed across oxide layers, (2) the tunneling of electrons, (3) and the possible nucleation and growth processes. They were able to describe the mechanism responsible for the apparent logarithmic nature of the reaction rate as a pore-blocking mechanism resulting from the 5% volume increase from Cu_2O to CuO. They recommended the use of the model described by Davies et al. (1954) as follows:

$$m = k_1 \ln(k_2 t + k_3)$$

where m represents the reacting species and k_1, k_2 and k_3 represent fitting constants, which may be thought of physically as relating to the number of open low-resistance pathways (e.g. pores, grain boundaries, cracks).

Evans (1960) developed a more easily understandable expression along these same lines. In the case of mutually blocking pores (blocking of neighboring pores through compression) the expression is given below and shows that conversion is a function of a blocking constant, λ, and a second constant, k_d.

$$X = \lambda \ln\left(1 + \frac{k_d t}{\lambda}\right)$$

Utilizing this method several groups were able to show that the effect of pore-blocking is commonly a function of temperature. Won and Sohn (1985) successfully accounted for the effect of pore-blocking, as did Sohn and Kim (2002) and Sohn et al. (2004) for very different types of materials. These groups were able to show that the pore-blocking influence may be readily recognized by two separate regimes of reaction rates: the first regime is characterized by quick initial rates and is followed quickly by the second as the reaction rate slows well before full conversion. This phenomenon may be seen in Figure 58 for the case of cuprous oxide oxidation.

It is important to note that while this effect is readily observed for the lower temperature regime, it is less obvious at temperatures above 700°C. Therefore another model must be employed for the characterization of the reaction kinetics at higher temperatures.

The low temperature activation energy may be determined when this pore-blocking effect is taken into account. By rearranging the equation above and plotting the left-hand side, exp(X/λ), against time the blocking constant is resolved by finding the value that gives the "best-fit" straight line using regression analysis at each temperature. Figure 60 displays the results of the pore-blocking analysis. The pore-blocking constant varies from 0.226 at 600°C to 0.182 at 700°C.

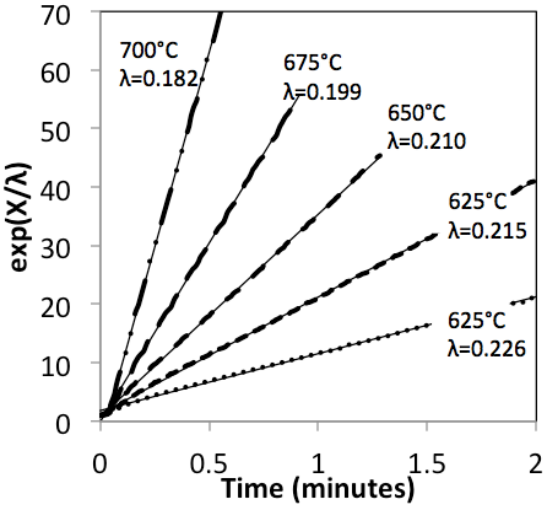

Figure 60. Pore-blocking kinetics for the low temperature oxidation of Cu_2O in 45_ZrO2_FG.

While the pore-blocking model describes well the observed kinetic behavior for the low-temperature oxidation of Cu_2O, it does not hold well above 700°C (Figure 59). While below 700°C the oxidation rates clearly change long before full conversion, the higher temperature rates actually approach close to full conversion before the effects of pore-blocking may be seen. This is especially true above 800°C.

For the case of high-temperature conversion of Cu_2O the nucleation/growth model by Avrami (1939) is used. While this model is generally used for modeling the start of reactions it may also be extended to reactions where the individual grain boundaries are small enough that nucleation must occur individually for each grain. Commonly, for metals and powders, Avrami expression is used to model the redox characteristics (Lin 2003; Prisedsky 2004). The expression is given by:

$$[-\ln(1-X)]^{1/n} = k_{app}t$$

where n represents a constant used to describe the type of nucleation and growth that is occurring. By rearranging:

$$ln[-\ln(1-X)] = n\ln(k_{app}) + n\ln(t)$$

The growth constant *n* was determined by a best-fit approach, plotting ln[–ln(1–*X*)] against *n*ln(*t*) and for both carriers it was determined that *n*=1 is matches the experimental data best.

In summary, two sets of models have been used to characterize the oxidation characteristics of Cu_2O in oxygen carriers. The first of these, pore-blocking kinetics, was used to model the kinetic observations of Cu_2O at and below 700°C, while the second model, Avrami-Erofeev, was used to model the oxidation of Cu_2O above 800°C. The influence of the solid on the reaction was identified in each of these cases and is shown in Table 16.

Table 16. Influence of temperature within the two different temperature regimes for the oxidation of Cu_2O within two different oxygen carriers.

Carrier Material	High Temperature		Low Temperature	
	f(X)	N	f(X)	λ
45_ZrO2_FG	1-X	n = 1	1/exp(X/ λ)	$\lambda = -4.16\times10^{-4}\times T + 0.48$
50_TiO2_MM	1-X	n = 1	1/exp(X/ λ)	$\lambda = -2.95\times10^{-4}\times T + 0.34$

Influence of Temperature on Oxidation Rate

Using the methods described above the function *f(T)*, or the temperature influence on the reaction, is uncovered by mathematic manipulation. If it is assumed that *f(T)* takes the form:

$$f(T) = A\times \exp\left(-\frac{E_a}{RT}\right)$$

Then the activation energy and pre-exponential factor are both solved for using the correct models associated with both the high- and low-temperature regimes. The activation energy calculated for the low-temperature regime is averaged to 168 kJ/mol between both materials and 69 kJ/mol at the higher temperature range. The resulting pre-exponential factors are given as 2.1×10^{12} (min^{-1}) for the lower temperature range and 7.9×10^{4} (min^{-1}) at the higher temperature range.

High Temperature Model Comparison

A summary of experimentally determined constants for the nucleation/growth kinetic expression is presented in Table 17.

Table 17. Model used to predict the conversion of Cu_2O in two different oxygen carriers using the nucleation/growth kinetics expression Avrami-Erofeev.

Influence	Model Values
$f(X)$	$1 - X$
$p_{O_2,eq}$	$P_{O_2}(atm) = 6.057\times10^{-11}e^{0.02146\,T(°C)}$
$f(p_{O_2})$: $(p_{O_2}^{\alpha} - p_{O_2,eq}^{\alpha})$	$\alpha = 1.3$
$f(T) = A\times exp\left(-\frac{E_a}{RT}\right)$	A = 7.90×10^{4} (min^{-1}); E_a = 69 (kJ/mole)

A comparison of the prediction against the conversion profiles for both materials at 800°C is presented in the left plot of Figure 61. The conversion of the titania material is much faster than the prediction. This may be explained by the change from the low temperature oxidation mechanism (pore-blocking kinetics) to the high temperature mechanism (nucleation and growth kinetics). There may be some transition period where neither completely accurately describes the true mechanism, but 800°C is lower than anticipated for operation of an industrial scale chemical-looping reactor. The higher temperatures are more likely to be seen in an industrial/commercial setting (temperatures above 900°C). The right plot of the figure displays the conversion profiles for the titania and zirconia materials along with the predicted values at 925°C. This figure shows the model is better at predicting the higher temperature conversion profiles.

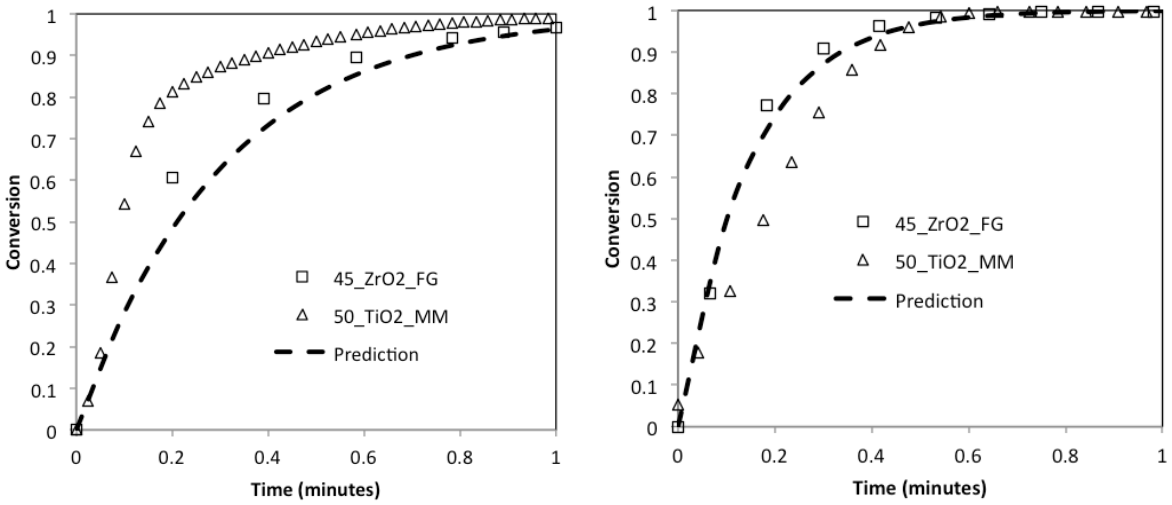

Figure 61. Conversion profiles for the oxidation of Cu_2O at 800°C (left) and 925°C (right) for 45_ZrO2_FG (□) and 50_TiO2_MM (Δ), compared against the model prediction (- - -).

Conversion of Solid Fuels with CLOU Carriers

In order to gauge performance of the studied CLOU carriers for converting solid fuels in a fluidized bed, tests were performed in which small batches of fuel were added while the bed was fluidized with nitrogen, allowing oxygen uncoupling. Three different fuels (Illinois #6 coal, Black Thunder coal from the Powder River Basin (PRB), and petroleum coke) were used for this study and were converted in the fluidized bed using two different oxygen carriers (50_TiO2_MM and 45_ZrO2_MM). Table 18 shows the analyses of the tested fuels.

Table 18. Analyses of solid fuels used in this study.

Fuel Type	Illinois #6 Bituminous	Black Thunder PRB Sub-bituminous	Green Coke Petroleum Coke
Proximate Analysis			
Moisture (wt% as received fuel)	2.54	21.30	0.4
Ash (wt% Dry)	12.33	6.46	0.39
Volatile matter (wt% dry)	39.40	54.26	11.03
Fixed carbon (wt% dry)	48.28	39.28	88.01
Ultimate Analysis (wt% dry ash-free)			
Carbon	78.91	74.73	89.21
Hydrogen	5.50	5.40	3.78
Nitrogen	1.38	1.00	1.73
Sulfur	4.00	0.51	5.82
Oxygen	10.09	18.27	4.41
Chlorine	0.11	0.08	-
Heating Value			
HHV, dry (Btu/lb)	12,233	12,815	15,622

The reactivity of the tested fuels, from low to high, is petcoke < Illinois #6 < Black Thunder PRB. Petcoke is stripped of most of the volatile content from the creation process and is less reactive than the coals studied. The PRB coal is a sub-bituminous and thus has a lower rank than the bituminous Illinois #6 coal. The lower rank coals generally have higher reactivities. This ordering may be observed in Figure 62 where the conversion of carbon versus time is displayed for the three fuels during combustion using 50_TiO2_MM material at 930°C. The PRB coal reacts very quickly reaching full conversion in just a few seconds. The Illinois #6 coal and petcoke, however, do not reach full conversion. From a stoichiometric standpoint, the oxygen supplied by the metal oxide carrier should be more than sufficient to fully combust all of the fuels. The amount of fuel supplied to the reactor was evaluated by determining the expected amount of oxygen released from the oxygen carrier bed between 20% and 80% conversion from CuO to Cu_2O. Therefore, the amount of oxygen released from the carrier should be 40% more than is necessary for complete carbon burnout of the fuel.

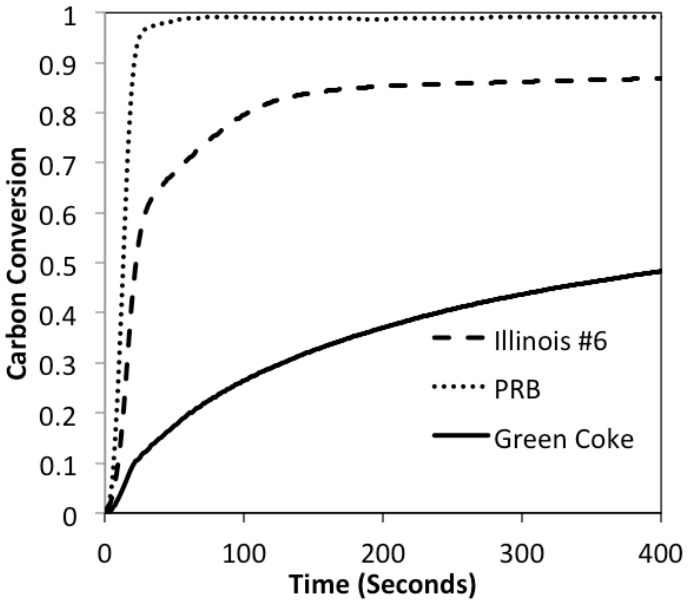

Figure 62. Conversion of three different fuels using 50_TiO2_MM material at 930°C. The conversion is calculated from the mass of carbon (as gas) analyzed and collected by infrared analyzer.

A simple explanation for the lack of full conversion could be that the unreacted fuel was simply blown out of the reactor before it could be consumed. If that is the case the ensuing oxidation cycle would yield no additional carbonaceous products, or at least it would not account for all of the missing carbon. The full conversion profile of the petcoke fuel during the "fuel reactor" cycle with N_2 as well as the "air reactor" cycle with air feed is given in Figure 63. Clearly, as the conversion approaches 50% the rate slows considerably and is near zero around 700 seconds of reaction. Air is once again cycled to the reactor around 700 seconds, and the missing carbon is burned off. It is clear from this figure that the fuel is not being ejected from the reactor, but is simply not completely reacted within the fluidized bed. The full reaction profile obtained during the combustion of Illinois #6 coal is very similar to the petcoke, in that, it is not fully combusted until the air is once again cycled through the reactor.

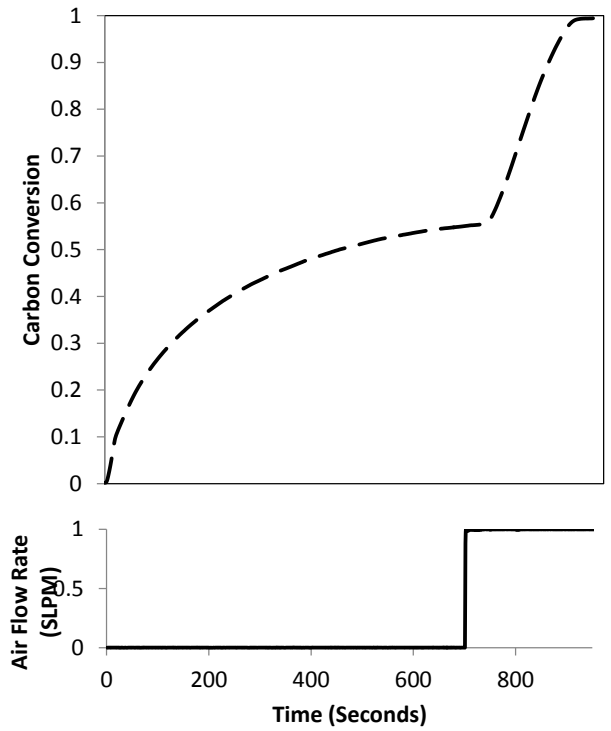

Figure 63. Conversion of carbon during combustion of green petcoke at 930°C using 50_TiO2_MM in a fluidized bed.

Once again, the incomplete combustion of these fuels is not a result of insufficient oxygen supply. Certainly, the fuel is oxygen starved, but it is due to the slow reactivity of the fuel and not due to an excessive charge of fuel to the reactor. This characteristic is accentuated and more easily understood by looking at the effects of increasing the fuel particle size.

The combustion of PRB particles ranging from 150 μm to 6,000 μm (0.3 cm) at 930°C using the 45_ZrO2_FG material is given in Figure 64. The three tests were performed by selecting particles that fit the desired size range while having a very similar combined mass. For example, the sample tested in the 6,000 μm range consisted of only one particle. This single particle had a mass very similar to the combined masses of the other two samples individually. While, once again, the combustion of the small particle size (150 μm) was completed very quickly (roughly one minute) the other two samples did not reach full conversion of the carbon even though the masses of each of the three samples was very nearly equal.

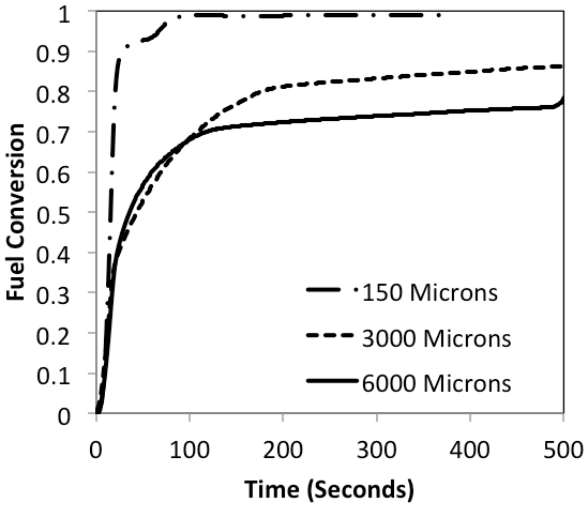

Figure 64. Carbon conversion is tracked during the combustion of PRB at 930°C using 45_ZrO2_FG in a fluidized bed.

Admittedly, it may be possible to achieve complete burnout of the larger fuel particles if the amount of oxygen carrier is increased. However, it is likely the complete burnout will not be due to the increased amount of available oxygen, but instead due to an increase in the reaction time due to a deeper particle bed. The slower decomposition rates may be achieved by the oxygen carrier simply due to an increased oxygen partial pressure. The increase in the oxygen partial pressure effectively decreases the driving force for decomposition.

Even for a more reactive fuel, like PRB coal, a fuel particle size threshold may exist above which a particular oxygen carrier may be ineffective, not because it releases oxygen too slowly, but because it releases oxygen more quickly than it can be consumed by the large particle. The higher rates of oxygen release then produce oxygen that is unreacted and dilutes the fuel reactor product stream. In such a case, "gas polishing" by addition of natural gas to consume the oxygen, may be necessary.

The left plot in Figure 65 shows the conversion of the solid oxygen carrier from CuO to Cu_2O during the combustion of large petcoke particles (roughly 3,000 μm) using 45_ZrO2_FG at 930°C and 960°C. The conversion of the solid oxygen carrier material at 960°C is shown as well. At roughly 200 seconds the oxygen carrier is nearly completely spent and the rate of decomposition slows, essentially to zero. In both cases, the fuel is incompletely combusted and stops as the oxygen is no longer devolved. Due to the increased reactivity of the petcoke at 960°C the conversion profile for that temperature is extended. Once again, while the amount of oxygen is sufficient for the combustion of this fuel, it is simply released and swept away too quickly to react with the remaining petcoke.

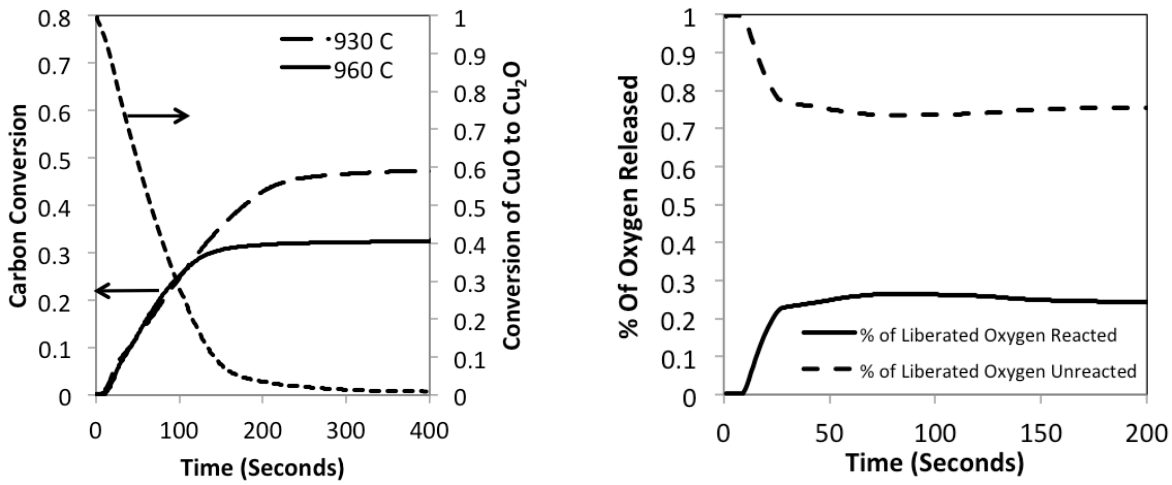

Figure 65. Conversion of carbon (left) and oxygen liberation (right) during the combustion of petcoke particles with a diameter of roughly 3,000 μm at two temperatures using the 45_ZrO2_FG material.

The right plot in the figure suggests that the oxygen contained within carbonaceous gas evolved during the combustion of the large petcoke particles accounted for only about 25% of the total evolved oxygen. The remaining 75% of the liberated oxygen was swept through the outlet as unreacted oxygen. This number actually speaks well to the performance of the oxygen carrier, and is undoubtedly a consequence of the relatively shallow bed employed in these tests.

Evaluation of Attrition Rates for Various Copper-based Carriers

Attrition rates of four different CuO-based oxygen carriers were measured in the lab-scale fluidized bed system. The four carriers were the 50_TiO2_MM, 45_ZrO2_FG, 50_SiO2_IW and 70_SiO2_IW shown in Table 8.

To measure attrition, the mass of fine material resulting from abrasion/attrition of carrier particles in the fluidized bed system was measured by capturing the elutriated particles on a filter downstream of the fluidized bed. The filters are shown on the schematic of the experimental apparatus presented in Figure 14.

Oxygen carrier attrition testing began with sieving the selected material to the desired particle size range. Table 19 lists the particle size range and reactor conditions employed in each test. It should be noted that the 45_ZrO2/MgO_FG (same as 45_ZrO2_FG in Table 8), 50_SiO2_IW and 70_SiO2_IW samples were not "fresh" materials; they had been oxidized and reduced a small number of cycles prior to the attrition study. It should also be noted that due to the limited supply of 50_SiO2_IW and 70_SiO2_IW samples, a larger particle size range was necessary to acquire sufficient bed material. Once an adequate amount of material was obtained from sieving the sample was weighed and deposited into the top of the quartz reactor tube. Initial bed weight was recorded.

Table 19. Experimental conditions for attrition study. U/Umf represents the ratio of actual gas velocity to calculated minimum fluidization velocity.

Test #	Sample Name	Oxidizer	Reducer	U/Umf	Particle Diameter, μ	Temp, °C	Oxidation Time, Min	Reduction Time, Min	Number of Loops
1	50_TiO2_MM	Air	N2	5	75 – 105	800	30	30	3
2	50_TiO2_MM	Air	N2	10	75 – 105	900	30	30	3
3	50_TiO2_MM	Air	N2	5	75 – 105	900	30	30	3
4	50_TiO2_MM	Air	N2	10	45 – 75	900	30	30	3
5	45_ZrO2/MgO_FG **	Air	N2	5	75 – 105	800	30	30	3
6	45_ZrO2/MgO_FG **	Air	N2	10	75 – 105	900	30	30	3
7	45_ZrO2/MgO_FG **	Air	N2	5	75 – 105	900	30	30	3
8	45_ZrO2/MgO_FG **	Air	N2	10	45 - 75	900	30	30	3
9	50_SiO2_IW **	Air	N2	5	106 – 250*	800	30	30	3
10	50_SiO2_IW **	Air	N2	10	106 – 250*	900	30	30	3
11	50_SiO2_IW **	Air	N2	5	106 – 250*	900	30	30	3
12	50_SiO2_IW **	Air	N2	10	45 – 150*	900	30	30	3
13	70_SiO2_IW **	Air	N2	5	106 – 250*	800	30	30	3
14	70_SiO2_IW **	Air	N2	10	106 – 250*	900	30	30	3
15	70_SiO2_IW **	Air	N2	5	106 – 250*	900	30	30	3
16	70_SiO2_IW **	Air	N2	10	45 – 150*	900	30	30	3

* A larger particle size range was used for testing do to the limited supply of the oxygen carrier sample.
** Samples are not "fresh" materials. They have been oxidized and reduced a small number of cycles prior to the attrition study.

Table 20 provides the filter number, filter holder designation, time interval and a description of the test segment for which the filter was utilized in attrition testing. 25 mm Teflon membrane filters (PTFE filters on polypropylene support) with a pore size of 1 μm were found to perform best for the study. Initial tests using glass fiber filters resulted in partial ripping of the filter, which would adhere to the filter holder resulting in mass loss. Filters 1.1 and 2.1 were weighed on a tared watch glass in a microbalance after the bed material had been added to the reactor. Initial filter weights were recorded, then the filters were placed in the designated filter holder. Gas velocities were calculated in order to achieve the proper ratio of fluidizing velocity to minimum fluidization velocity (u/u_{mf}) and the gas was initiated in the reactor control system. The system was monitored for proper "bubbling" fluidization and gas leaks. Ball valves were set to direct gas flow through filter holder #1, then the furnace was allowed to begin warming. Furnace temperature was automatically increased slowly at an approximate rate of seven degrees per minute so as to not shock the bed material, which could potentially fracture the oxygen carrier particles as a result of rapid expansion. Filter 1.1 was employed for the warming segment after which the direction of gas flow was switched to filter holder #2. Filter 1.1 was then carefully removed on to a tared watch glass, weighed and recorded. This procedure was repeated following the filter schedule of Table 20 until completion of the test run, switching back and forth between holder one and two as per the schedule. In the event of a large difference in initial to final weighing the filter would be collected in a sample vial for further testing of its contents. When the reactor bed material had sufficiently cooled the final bed weight was determined and recorded.

Table 20. Filter schedule utilized in attrition tests.

Filter Number	Filter Holder	Time (hrs.)	Test Segment
1.1	1	2	Warming
2.1	2	1.5	Loop 1
1.2	1	1.5	Loop 2
2.2	2	1.5	Loop 3
1.3	1	2	Cooling

The amount of material collected on the filter during each hour was calculated in terms of the total mass of carrier material in the bed to yield the fraction of bed lost per hour. A summary of all conditions tested is presented in Figure 66, which shows average loss per hour for the different carriers. Several interesting observations can be made. First, the 50_TiO2_MM material clearly showed much worse loss due to attrition than the other three carriers. This is particularly apparent during the first two hours of testing. There are a number of reasons for this. First, the 50_TiO2_MM was produced by mechanical mixing of fine powders (~2-5 micron) to a paste, followed by extrusion and calcining. The 45_ZrO2/MgO_FG was formed by freeze granulation (similar to spray drying) and the SiO2-based materials were formed by incipient wetness using pre-manufactured support material. SEM microscopy shows the heterogeneous nature of the 50_TiO2_MM material, and individual particles of CuO and TiO2 can be observed. Even by visual inspection it appears that the material would easily break down through attrition in a turbulent bed environment. Secondly, the 50_TiO2_MM material had never been processed in a fluidized bed, so there was initial "break in" period of high particle loss during the first two hours, after which attrition decreased notably. However even after the materials had been exposed for 6 or more hours, the 50_TiO2_MM material showed comparatively high attrition rates.

The second conclusion from the figure is that attrition rates decrease over time, even for the three carrier materials that had previously undergone several oxidation/reduction cycles in the fluidized bed. Considering just the final hours of testing, the 50_TiO2_MM lost an average of 0.0032% of the bed mass per hour over the range of conditions studied. The best performing material, the 45_ZrO2/MgO_FG lost just 0.0008% per hour during the final hours of testing.

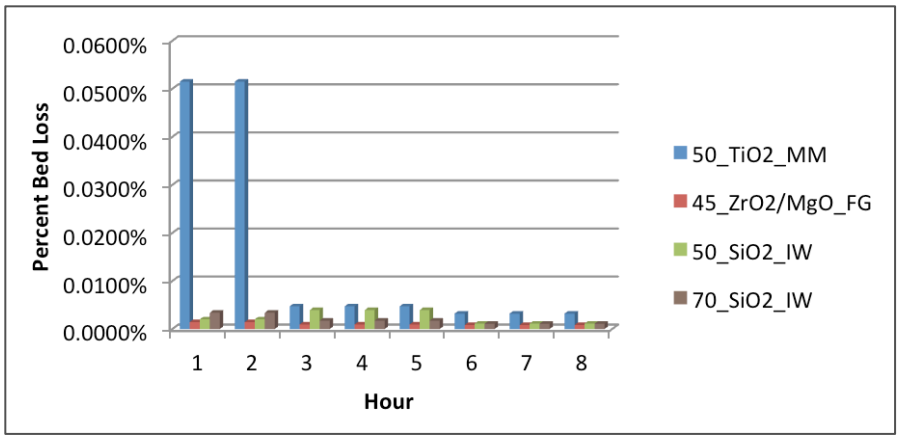

Figure 66. Measured mass loss per hour as a result of carrier attrition for the four carriers tested.

Additional tests explored the influence of carrier particle size, bed temperature and fluidizing velocity. Measured bed material loss was higher for smaller particles, presumably because the attritted particles become small enough to be elutriated from the bed. Bed temperature (900 versus 800°C) showed no systematic effect. Increasing fluidizing velocity (10 versus 5 times the minimum fluidizing velocity) caused more bed loss, a result of both increased turbulence in the bed and a high propensity for elutriation due to the higher velocity.

A comprehensive report describing the attrition measurement method, results and analysis under a range of temperatures with various carriers, is available as an undergraduate thesis (Allen 2013).

Subtask 5.4 – CLC Kinetics

Support Material Results and Selection of Silicon Carbide

Copper-based oxygen carrier materials supported on alumina, titania, zirconia, silicon carbide, sand, and celite were investigated. A summary of the results, including representative rate constant values calculated in TGA experiments without the use of fuel and other comments, can be found Table 21. The principle criterion used to compare the performance of each support material was the oxidation and reduction reaction rates and the ability for the sample to reduce and oxidize consistently over multiple cycles. Support materials that did not allow for the oxidation and reduction reactions to occur in a timely manner and consistently over time were rejected. Based on the TGA experiments alone, various support materials could have been investigated further; however, all of the materials that showed potential for use in CLOU had some deficiency in some other area. For silicon carbide and sand, their low surface areas (less than $1 m^2/g$) limited the CuO carrying capacity. Celite was investigated because of it high surface area, but it lacks the mechanical strength needed to resist attrition in fluidized-bed environments.

Table 21. Average oxidation and reduction rate constants of copper oxide supported on various materials. All samples were 20% CuO by weight except for Polish Titania (50%) and sand (10%). The results are for the 4th loop of fresh samples. Note that the initial loops consistently differ from later loops.

Support Material	Oxidation Rate Constants at 935°C ($s^{-1} \times 10^4$)	Reduction Rate Constants at 935°C ($s^{-1} \times 10^4$)	Comments
Alumina (Baker)	309	200	Becomes less reactive with each loop
Alumina (Sigma-Aldrich)	20	5	Not reactive in TGA
Polish Titania	96	67	Low mechanical strength
Titania	171	152	Initially oxidizes; performs well afterward
Zirconia	33	163	Incomplete oxidation
Sand*	105	116	Low surface area
Celite	208	157	Low mechanical strength
Silicon Carbide (Sigma- Aldrich)	-	-	No reactivity in TGA
Silicon Carbide (Pfaltz & Bauer)	365	131	Low surface area
SiO_2 (from β-SiC) Bake then coat	288	170	Sinters in fluidized-bed reactor
SiO_2(from β-SiC) Coat then bake	32	101	Slow Oxidation, no agglomeration

A new material with a higher surface area and the mechanical strength necessary to resist agglomeration and attrition in fluidized-bed environments was needed. Material with those qualities, β-SiC ($25 m^2/g$ surface area, 150μm diameter spheres), was acquired from SICAT. This material could support a load of 42% CuO by weight and undergo fluidized-bed experiments without showing signs of agglomeration or attrition.

Wet Impregnation vs. Rotary Evaporation Method

Oxygen carrier materials prepared by the wet impregnation method provided were noticeably heterogeneous. The support material and the fine CuO powder were easily distinguished. A new method of preparation that yielded a homogeneous material was developed. The rotary evaporator method improved the uniformity of the deposition of CuO onto the support material. While the material made by wet impregnation was a heterogeneous mixture of support material and CuO, the rotary evaporation method gave a material that appeared homogeneous even at a microscopic level. As seen in Figure 67, the SiC particles are uniformly covered by CuO.

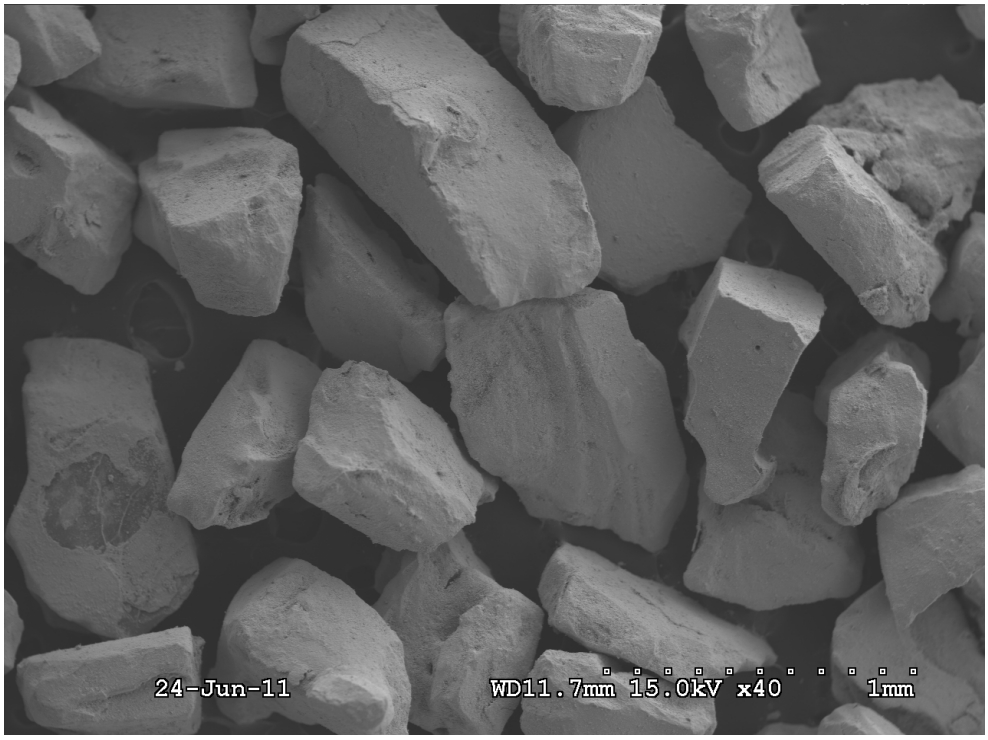

Figure 67. SEM image of 20% CuO by weight on SiC (Pfaltz & Bauer) prepared by rotary evaporation method and 8 additions of CuO.

Not only did the new rotary evaporation method improve the uniformity of the CuO coating of the support material, it also improved the kinetics of both the oxidation and reduction reactions of the oxygen carrying material. Figure 68 and Figure 69 show box and whisker charts of all the calculated rate constants for the oxidation and reduction reactions, respectively. All of the values come from TGA experiments performed with 20% CuO by weight on SiC material prepared by each method. The figures for both the oxidation and reduction reactions show that the samples prepared by the rotary evaporation method react at a faster rate than those prepared by the wet impregnation method. Once this was discovered, all subsequent samples were prepared via the rotary evaporation method.

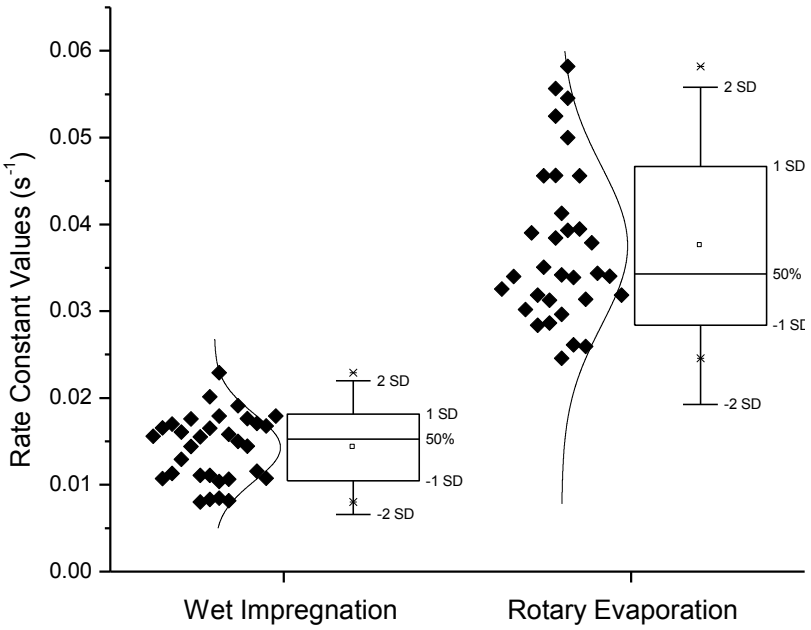

Figure 68. Box and whisker plot of all k values of the oxidation reactions calculated for 20% CuO by weight on SiC (Pfaltz & Bauer).

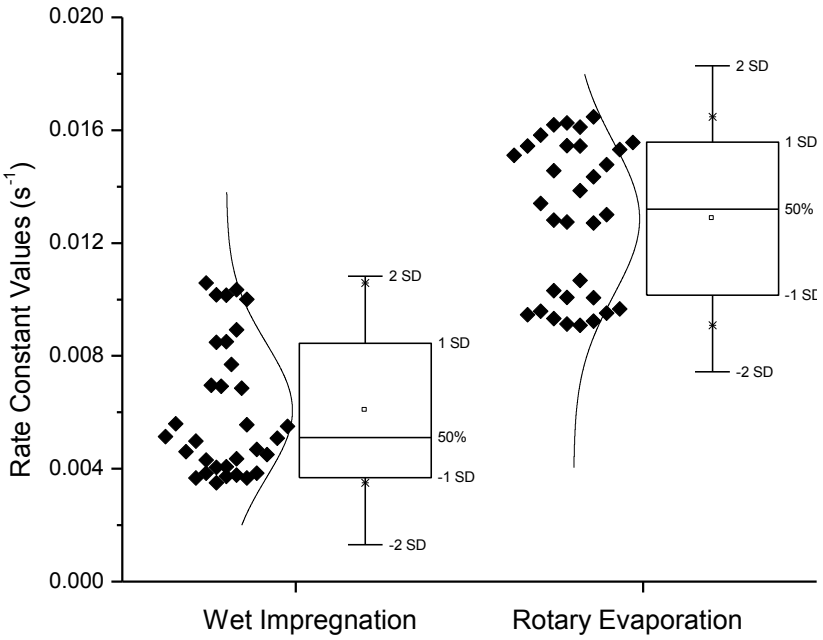

Figure 69. Box and whisker plot of all k values of the reduction reactions calculated for 20% CuO by weight on SiC (Pfaltz & Bauer).

Oxygen Carrier with β-SiC Support Material Development

The surface area of the β-SiC before the addition of CuO was determined by BET experiments to be 25m^2/g. Initial TGA experiments revealed that the β-SiC as a support for CuO was not stable in air during TGA experiments and did not allow for the oxidation/reduction reactions to occur. Moene et al. (1998) reported that high surface area silicon carbide sinters and converts to SiO_2 in oxidizing environments over 800°C.

$$SiC(s) + 2O_2(g) \rightleftharpoons SiO_2 + CO_2 \qquad (5.4.14)$$

This was confirmed to be the case with this material when the β-SiC was calcined in a muffle furnace at 980°C for a week. The SiO_2 was analyzed by BET, and the surface area had decreased from 25m^2/g to 11m^2/g. The surface area of the SiO_2 material is still much larger per gram than the other promising support materials, such as sand and SiC.

The preparation method of CuO/β-SiC material was altered to solve the problems created by its instability. The first method that was attempted was the bake and coat method. The β-SiC was first calcined and allowed to convert to SiO_2. CuO was then deposited on the SiO_2 by the rotary evaporation method. This material performed very well in TGA experiments; however, in fluidized-bed testing the samples showed signs of agglomeration and were rejected.

A second variation, named the coat then bake method, involved the same concept as the bake and coat method except the order of the baking and coating was reversed. The principal concept in this method assumes that as the β-SiC converts to SiO_2 the material sinters, and the CuO that is deposited on the support material will then be lodged inside the particle. TGA experiments with the coat then bake method were satisfactory and the fluidized-bed experiments were also successful.

After the coat then bake method was determined to create a material suitable for fluidized-bed experiments, the CuO capacity of the β-SiC material was investigated. Samples with 20, 50, and 70% by weight CuO were prepared. The percent of CuO was calculated based on the β-SiC material. After baking, the SiO_2 material accounts for more mass in the sample so the adjusted CuO loads were calculated to be 16, 42, and 62%, respectively.

The 16 and 42% CuO samples were tested in fluidized-bed experiments up to 1000°C and showed no signs of agglomeration. The 62% CuO sample showed signs of agglomeration at 900°C and was rejected. The CuO capacity for the β-SiC support material using the coat and bake method is somewhere between 42 and 62%.

TGA Results

TGA experiments were performed to analyze the oxygen carrying capacity of the 42% load sample (Figure 70). The results showed that the percent weight change between the oxidized and reduced sample was 4.1%; this value corresponds fairly close to the theoretical value of 4.2%. The oxidation reaction required more than 90 min to reach completion (Figure 71). However, Figure 72 shows that the 80% oxidation was reached in 4.75 min. The reduction reaction (Figure 73) reaches completion in less than 9 min.

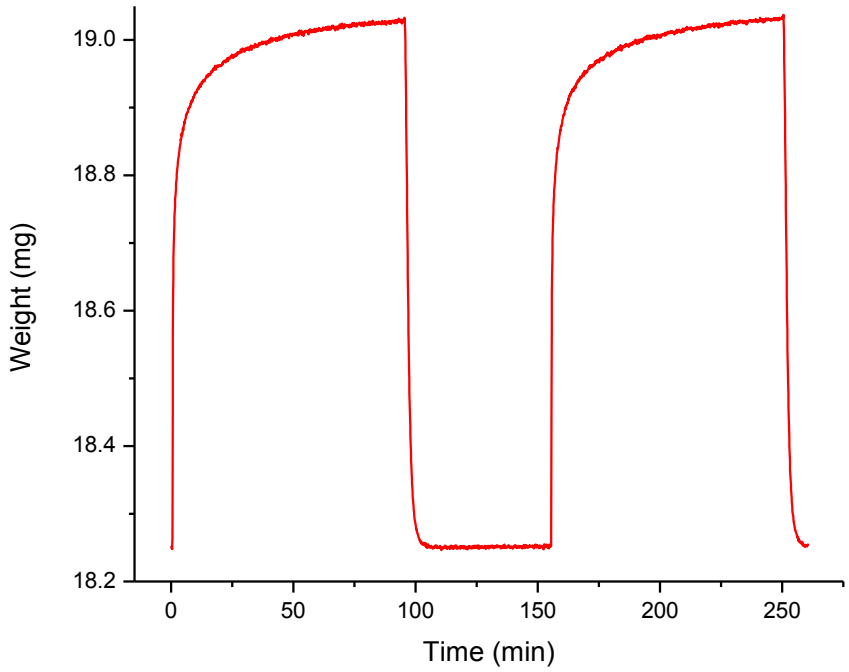

Figure 70. TGA trace of two loops of 42% CuO on SiO_2 at 900°C.

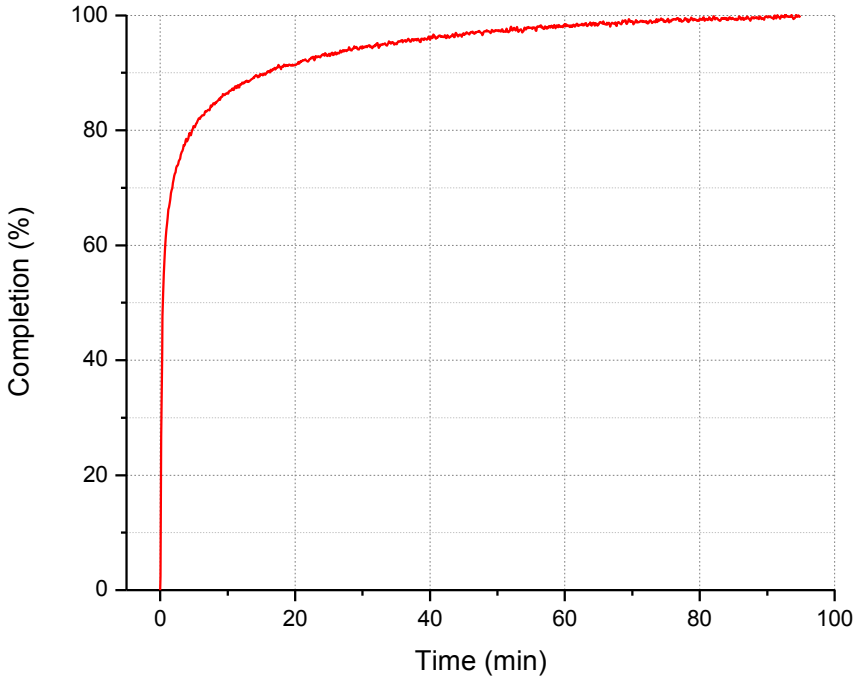

Figure 71. One complete oxidation reaction for a 19mg sample of 42% CuO on SiO_2 at 900°C.

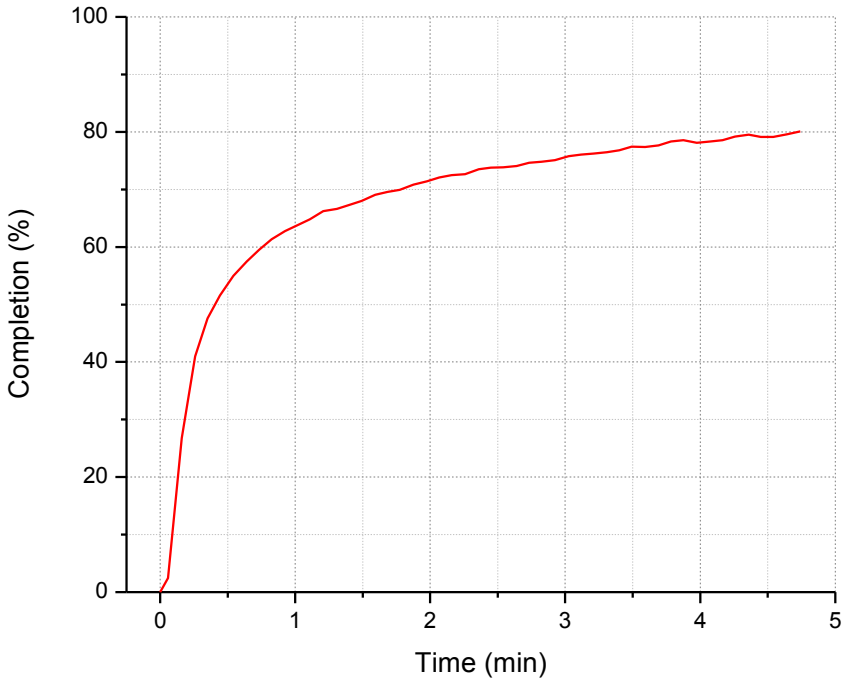

Figure 72. Oxidation of a 19mg sample of 42% CuO on SiO_2 to 80% Completion at 900°C.

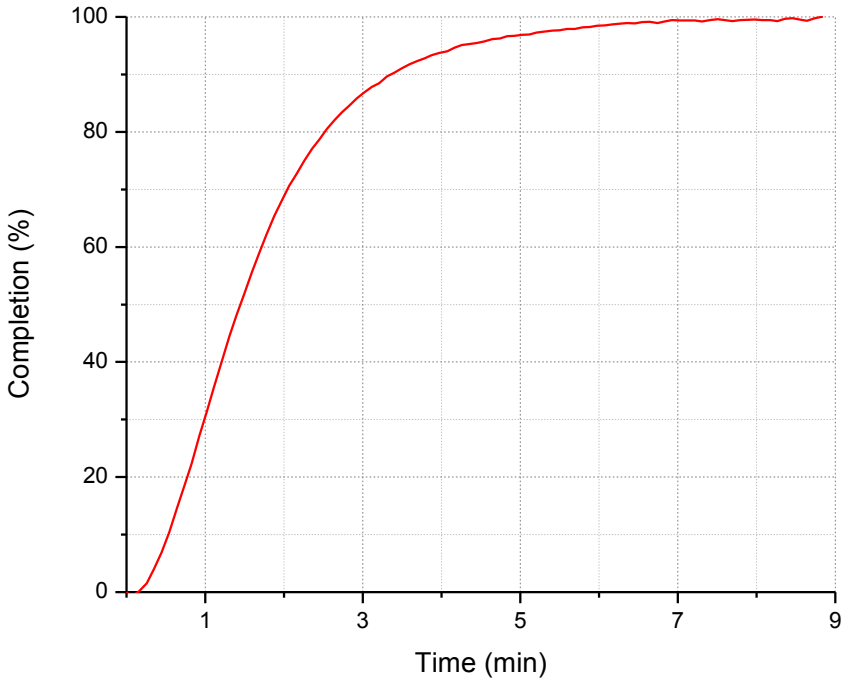

Figure 73. One complete reduction reaction for a 19mg sample of 42% CuO on SiO_2 at 900°C.

SEM Images

SEM and corresponding EDS images of the 16 (Figure 74) and 42% (Figure 75) samples were taken at various stages in the coat then bake methods to observe the changes between each step. The first stage is after the CuO has deposited on the β-SiC. The second is after the calcination of the material. The third is after fluidized-bed experiments.

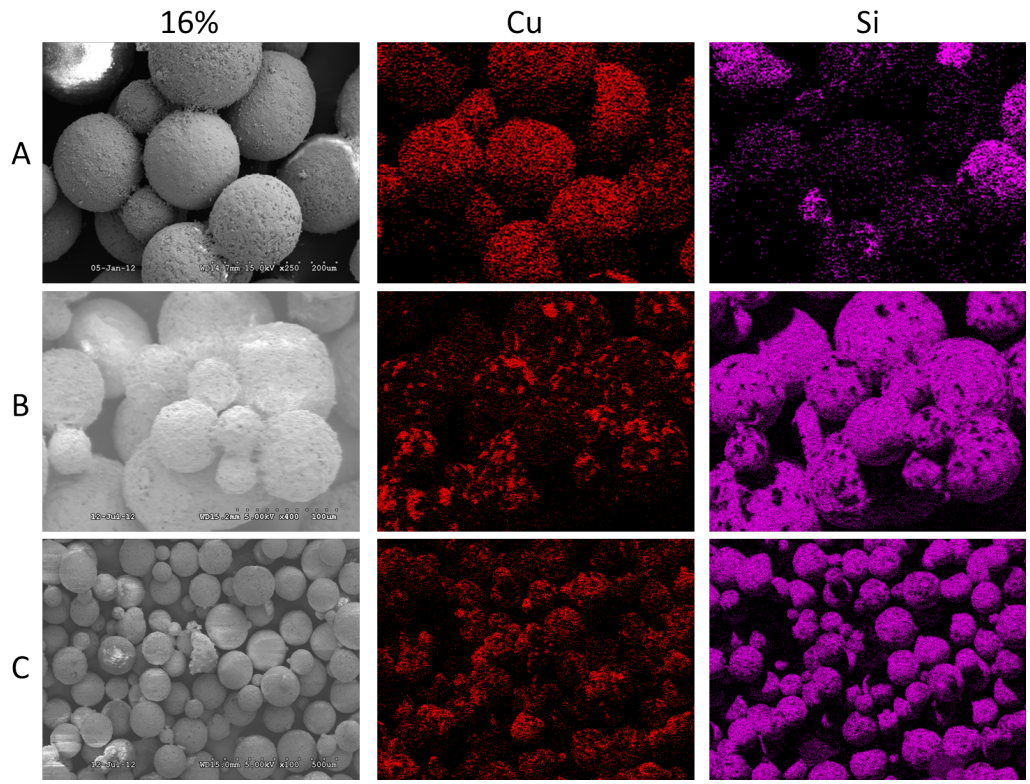

Figure 74. SEM images of the CB16 sample and corresponding EDS images of elemental Cu and Si A) before baking B) after baking C) after fluidization.

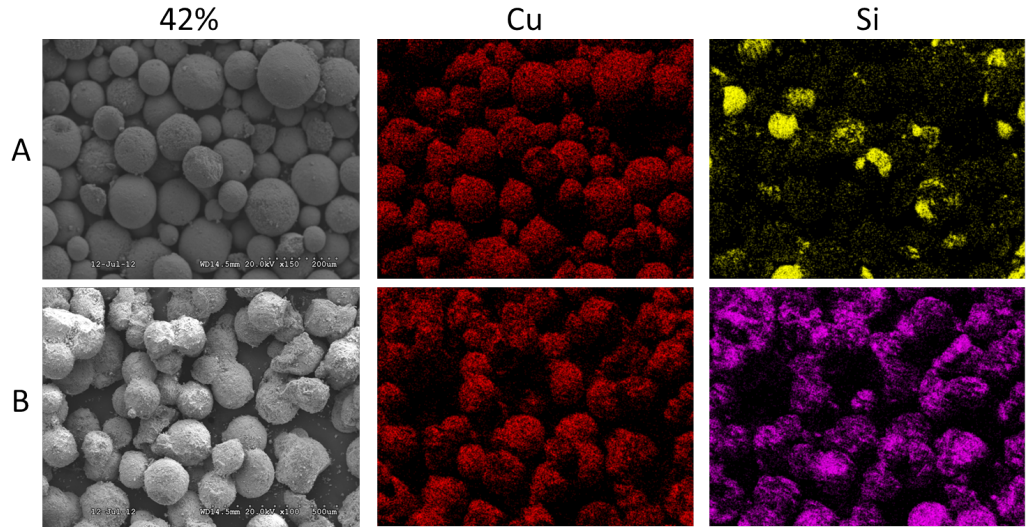

Figure 75. SEM images of the CB42 sample and corresponding EDS images of elemental Cu and Si A) before baking B) after baking.

The images show that the β-SiC was well coated by CuO. The images taken of the material before the calcination step show that the predominant element on the external surface is Cu, while Si is less apparent. This relationship is reversed in images taken after the calcination of the material in which Si is the more

prominent element and Cu is less apparent. This is favorable because de Diego et al. (2007) reported that the CuO deposited on the external surface of support particles is lost in fluidized-bed experiments. The coat then bake method allows for the CuO located on the external areas of the β-SiC to be shielded as the conversion to SiO_2 takes place (Moene et al. 1998). The CuO is buried inside and will subsequently not be knocked off of the support material during collisions that occur in fluidized-bed conditions.

In the SEM images of the samples after baking, there are clumps of multiple spheres that appear to have fused together. These clumps seem to be formed during the baking of the material and conversion to SiO_2 because they appear only after baking. These agglomerations also appear in the samples after fluidization; however, there is about the same amount of these agglomerations in each sample, which suggests that they fused together during the calcination step and not during the fluidized-bed reactor experiments.

CONCLUSIONS

Process and economic models. Comparing the process model results of CLOU with those of CLC employing an iron-based oxygen carrier revealed that:

The CLOU process has the potential to reduce reactor size and oxygen carrier inventory. As copper-based oxygen carriers cost significantly more than iron-based oxygen carriers, the lifetime of the oxygen carrier is the key factor for developing CLOU technology. Stability and strength are as important as oxygen reactivity. Additional conclusions include:

- It is vital to investigate strategies to reduce the residence time in the fuel reactor for the CLC process, as it affects oxygen carrier inventory, cyclone and reactor size, and fluidization costs.
- CLOU and CLC differ in energy extraction methodology, which impacts process design. For CLOU it is possible to extract energy from the air and fuel reactors. For CLC, the air reactor must be operated at a higher temperature than the fuel reactor. The metal oxide not only provides oxygen for fuel combustion in CLC but also supplies energy to support the endothermic reactions in the fuel reactor.
- The number of process trains required for the CLC and CLOU process is affected if the process is designed according to CFB criteria.
- CLC requires steam to facilitate coal gasification reactions, whereas CLOU operates on combustion released from the decomposition of a metal oxide. The effective utilization of steam for gasification and fluidization of oxygen carriers needs to be analyzed in detail while conceptualizing details for larger scale units.

Simulation of fluidized beds. The high-performance simulations developed under this subtask were able to capture the proper BFB behavior, and the results compare very well to experimental results. Our simulations also compared favorably to the previous simulations of BFB behavior. They were able to capture the transition of the stationary bed into the fluidized regime and replicate proper behavior of the bed as a function of bed height and superficial bed velocity. Including the effects of polydispersity did not necessarily translate to increased simulation accuracy. Simulation results using DQMOM models either matched, or under-performed, the behavior captured by simulations using monodisperse models, all at a much greater computational cost. While not the most efficient, DQMOM models can provide a distribution of particle sizes, something that is not possible with the monodisperse model. This leads to

the conclusion that the optimal choice of model to capture the fluidized-bed behavior varies. While the monodisperse model may be the most computationally efficient and fairly accurate, it may not provide information regarding particle characteristics distribution, something that is inherent in the more computationally intensive DQMOM model.

Laboratory-scale studies. The equilibrium behavior of the Cu_2O/CuO system targeted for CLOU is interesting in that the oxygen partial pressure becomes appreciable at temperatures above 825°C and rises rapidly at higher temperatures. Both oxidation and decomposition (O_2 release) depend on the so-called "driving force" associated with the difference between the O_2 partial pressure in the reactor environment and the equilibrium O_2 partial pressure. At otherwise similar conditions, a large difference between these two partial pressures would encourage fast reaction. However for oxidation in particular, as the equilibrium O_2 pressure increases with temperature, the difference between that and the 0.21 atm O_2 pressure of air results in less driving force. This reduction in driving force is even more extreme than any increase of rate with temperature due to intrinsic kinetics, with the consequence that the observed rate of oxidation actually decreases with temperature beyond roughly 850°C. In this study those two effects were separated and modeled. In addition, the influence of Cu_2O concentration (degree of conversion) was analyzed and found to best be modeled by considering two regimes, a low temperature regime in which the rate at high conversion slows due to pore blocking and a high temperature regime (>700°C) which is best modeled by considering grain nucleation and growth. Finally, the reaction order in oxygen driving force was concluded to be 1.3. The resulting models reasonably describe oxidation of copper-based oxygen carriers.

Release of oxygen by decomposition of CuO also depends on the driving force available. Oxygen present in the surrounding gas will slow the rate of reduction. The observed activation energy for CuO reduction of roughly 274 kJ/mol is a consequence of the intrinsic kinetics, with an activation energy of approximately 62 kJ/mol and the strong dependence of driving force on temperature. Reduction was determined to be zero order in CuO and approximately first order in oxygen driving force, defined as the difference between oxygen equilibrium partial pressure and the partial pressure of the surrounding gas.

The released oxygen has an important effect on conversion of solid fuels in a fluidized bed. Rates of fuel conversion for the copper-based CLOU carriers were much higher than under non-CLOU conditions, and the relative observed rates of conversion corresponded to the ranking of fuels by their reactivity. While small particles (150 microns) were rapidly reacted, large particles (6 mm) were not able to be fully converted in the small lab reactor due to mass competing influences of mass transfer into the particle and the rapid release of oxygen. In short, the large fuel particles were starved for oxygen. This has consequences for industrial reactors where carryover of carbon to the air reactor could be a concern. Certainly, smaller particles are preferable, provided that they are no so small they elutriate from the bed.

Elutriation is also a concern for oxygen-carrier particles, since they are engineered and manufactured with expensive materials such as copper. The best manufactured carriers are robust and display low rates of attrition and associated bed loss, around 0.0008% loss per hour. However some materials, in particular those manufactured by combining ultrafine powders of constituent materials, rapidly wear down and experience significant bed loss over short periods of time.

CLC Kinetics. CLC Kinetics team developed kinetic data for various supported copper material. SiC was investigated further due to promising results. The preparation of CuO/SiC materials using the rotary evaporation method improved kinetic data and the deposition of the CuO. The initial SiC material had an undesirably low surface area so higher surface area β-SiC was acquired. The problems presented by the instability of β-SiC were then solved by developing the coat and bake method of preparation. The samples prepared by the coat and bake method performed well in TGA and fluidized-bed experiments.

LIST OF PEER-REVIEWED PUBLICATIONS

Clayton, C.K., Sohn, H.Y., Whitty, K.J., "Oxidation Kinetics of Cu_2O in Oxygen Carriers for Chemical Looping with Oxygen Uncoupling," *Industrial & Engineering Chemistry Research,* 2014, 53, 2976-2986.

Clayton, C.K.; Whitty, K.J. Measurement and Modeling of Decomposition Kinetics for Copper-Based Chemical Looping with Oxygen Uncoupling, *Applied Energy*, 2013, in press.

Peterson, S.B.; Konya, G.; Clayton, C.K.; Lewis, R.J.; Eyring, Wilde, B.R.; Eyring, E.M.; Whitty, K.J. Characteristics and CLOU Performance of a Novel SiO_2-Supported Oxygen Carrier Prepared from CuO and β-SiC, *Energy & Fuels,* 2013, 27,10, pp. 6040-6047.

Sahir, A.H.; Dansie, J.K.; Cadore, A.L.; Lighty, J.S. A Comparative Process Study of Chemical-Looping Combustion (CLC) and Chemical-Looping with Oxygen Uncoupling (CLOU) for Solid Fuels, *International Journal of Greenhouse Gas Control*, 2014, 22, pp. 237-243.

Sahir, A.; Sohn, H.Y.; Leion, H.; Lighty, J.S.; Lighty, J.S. Rate Analysis of Chemical-Looping with Oxygen Uncoupling (CLOU) for Solid Fuels, *Energy & Fuels,* 2012, 26, pp. 4395-4404.

Sahir, A.; Lighty, J.S.; Sohn, H.Y. Kinetics of Copper Oxidation in the Air Reactor of a Chemical Looping Combustion System using the Law of Additive Reaction Times, *Industrial & Eng Chem Research*, 2011, 50 (23), pp. 13330–13339.

REFERENCES

Abad, A.; Adánez, J.; Celaya, J.; de Diego, L.F.; García-Labiano, F.; Gayán, P. Mapping of the Range of Operational Conditions for Cu-, Fe-, and Ni-based Oxygen Carriers in Chemical-Looping Combustion, *Chem. Eng. Sci.,* 2007a, 62, pp. 533-549.

Abad, A.; Adánez, J.; Cuadrat, A.; de Diego, L.F.; García-Labiano, F.; Gayán, P. The Use of Ilmenite as Oxygen-Carrier in a $500W_{th}$ Chemical-Looping Coal Combustion Unit, *Int. J. Greenhouse Gas Control,* 2011, 5, pp. 1630-1642.

Abad, A.; Adánez, J.; Cuadrat, A.; de Diego, L.F.; García-Labiano, F.; Gayán, P. Theoretical Approach on the CLC Performance with Solid Fuels: Optimizing the Solids Inventory, *Fuel,* 2012, 97, pp. 536-551.

Abad, A.; Adánez, J.; de Diego, L.F.; García-Labiano, F.; Gayán, P. Reduction Kinetics of Cu-, Ni-, and Fe-Based Oxygen Carriers Using Syngas ($CO + H_2$) for Chemical-Looping Combustion, *Energy Fuels,* 2007b, 21, pp. 1843-1853.

Adanez, J.; Abad, A.; Garcia-Labiano, F.; Gayan, P.; de Diego, L.F. Progress in Chemical-Looping Combustion and Reforming Technologies, *Prog. Energy Combust. Sci.,* 2012, 38, pp. 215-282.

Adanez, J.; Celaya, J.; de Diego, L. F.; Garcia-Labiano, F.; Gayan, P.; Palacios, J. M. Operation of a 10 kW_{th} Chemical-Looping Combustor During 200 h with a $CuO-Al_2O_3$ Oxygen Carrier, *Fuel,* 2007, 86, 7-8, pp. 1036-1045.

Adanez, J.; Corbella, B. M.; De, D. L.; Garcia, F.; Palacios, J. M. The Performance in a Fixed Bed Reactor of Copper-Based Oxides on Titania as Oxygen Carriers for Chemical Looping Combustion of Methane, *Energy Fuels,* 2005, 19, pp. 433-441.

Allen, C. Investigation of Attrition Rates for Copper-Based Chemical Looping Carrier Particles, B.Sc. Thesis, Dept. of Chemical Engineering, University of Utah, 2013.

Alvarez, M.; Baraki, R.; Clayton, C.; Eyring, E.; Hradisky, M.; Kelly, K.; Konya, G.; Lighty, J.S.; Sahir, A.; Sarofim, A.F.; Smith, P.J.; Whitty, K.J. Chemical Looping Combustion Reactions and Systems, Task 5 Topical Report to US DOE, Utah Clean Coal Program, University of Utah, March 2011.

Avrami, M. Kinetics of Phase Change. I General Theory, *J. Chem. Phys.,* 1939, 7, pp. 1103-1113.

Babu, S.P.; Shah, B.; Talwalkar, A., Fluidization Correlations for Coal Gasification Materials-Minimum Fluidization Velocity and Fluidized Bed Expansion Ratio, *AIChE Symp. Ser.,* 1978, 74, pp. 176-186.

Bartok, W.; Sarofim, A.F. *Fossil Fuel Combustion A Source Book*. John Wiley & Sons, 1991.

Basu, P.; Fraser, S.A. *Circulating Fluidized Bed Boilers-Design and Operations*. Butterworth-Heinemann, 1991.

Bayham, S.; Chen, D.; Chung, E.; Fan, L.-S.; Kathe, M.V.; Kim, H.R.; Luo, S.; McGiveron, O.; Sun, Z.; Tong, A.; Wang, A.; Wang, D.; Zeng, L. Coal Direct Chemical Looping Combustion Process: Design and Operation of a 25-kW_{th} Sub-Pilot Unit, *Fuel,* 2013, 108, pp. 370-384.

Berguerand, N.; Lyngfelt, A., Design and Operation of a 10 kW_{th} Chemical-Looping Combustor for Solid Fuels - Testing with South African Coal, *Fuel*, 2008, 87, pp. 2713-2726.

Bergurand, N.; Lyngfelt, A. Chemical-Looping Combustion of Petroleum Coke Using Ilmenite in a 10 kW_{th} Unit – High Temperature Operation, *Energy & Fuels*, 2009, 23, pp. 5257-5268.

Bohn, C.D.; Cleeton, J.P.E.; Dennis, J.S.; Kidambi, P.R.; Scott, S.A. Interaction of Iron Oxide with Alumina in a Composite Oxygen Carrier during the Production of Hydrogen by Chemical Looping, *Energy Fuels,* 2011, 26, pp. 603-617.

Bouillard, J.; Lyczkowski, R.; Gidaspow, D. Porosity Distributions in Fluidized Bed with an Immersed Obstacle, *AIChE J.,* 1989, 35, 6, pp. 908-922.

CD-Adapco. STAR-CCM+ Version 8.06, *User Guide*, 2013, pp. 4816-4926.

Chadda, D.; Fahim, M.A.; Ford, J.D. Chemical Energy Storage by the Reaction Cycle CuO/Cu_2O, *Int. J. Energy Res.,* 1989, 13, pp. 63-73.

Chemical Engineering Plant Cost Index, *Chemical Engineering*, July 1, 2012, p.60.

Chen, S.; Wang, D.; Xiang, W.; Xue, Z. Design and Fluid Dynamic Analysis of a Three-Fluidized-Bed Reactor System for Chemical-Looping Hydrogen Generation, *Ind. Eng. Chem. Res.,* 2012, 51, pp. 4267-4278.

Cho, P.; Lyngfelt, A.; Mattisson, T. The Use of Iron Oxide as an Oxygen Carrier in Chemical-Looping Combustion of Methane with Inherent Separation of CO_2, *Fuel,* 2001, 80, pp. 1953-1962.

Davies, D.E.; Evans, U.R.; Agar, J.N. The Oxidation of Iron at 175 to 350 °C, *Proc. R. Soc. Lond. A.* 1954, 225, pp. 427-443.

Ding, J.; Gidaspow, D. A Bubbling Fluidization Model Using Kinetic Theory of Granular Flow, *AIChE J.,* 1990, 36, p. 1473.

Epple, B.; Orth, M.; Strohle, J., Design and Operation of a 1 MW_{th} Chemical-Looping Plant, Proceedings of the 2nd International Conference on Chemical Looping, Darmstadt, Germany, 2012.

Evans, U.R. *The Corrosion and Oxidation of Metals*. Edward Arnold Ltd., London, 1960.

Eyring, E.M.; Konya, G.; Lighty, J.S.; Sahir, A.H.; Sarofim, A.F.; Whitty, K. Chemical Looping with Copper Oxide as Carrier and Coal as Fuel, *Oil Gas Sci. Technol. Rev. IFP Energies nouvelles,* 2011, 66, pp. 209-221.

Fan, L.S. *Chemical Looping Systems for Fossil Energy Conversions.* Wiley-AIChE, Hoboken, New Jersey, 2010.

Fan, R.; Marchisio, D. L.; Fox, R. O. Application of the Direct Quadrature Method of Moments to Polydisperse Gas-Solid Fluidized Beds, *Powder Technol.,* 2004, 139, pp. 7-20.

Fletcher, T.H.; Pugmire, R.J.; Smith, K.L.; Smoot, L.D. *The Structure and Reaction Processes of Coal*. Plenum Press, New York, 1994.

Gauthier, T.; Pelletant, W.; Sozinho, T.; Stainton, H. Main Results Of The 10 Kw Coal Pilot Plant Operation, 2nd International Conference on Chemical Looping 2012, Darmstadt, Germany, 2012.

Grace, J.R.; Sit, S.P. Effect of Bubble Interaction on Interphase Mass Transfer in Gas Fluidized Beds, *Chem. Eng. Sci.,* 1981, 36, pp. 327-335.

Hartge, E.-U.; Heinrich, S.; Kramp, M.; Thon, A.; Werther, J. Operational Experience with a Coupled Fluidized Bed System for Chemical Looping Combustion of Solid Fuels, 2nd International Conference on Chemical Looping Combustion, Darmstadt,Germany, 2012.

Hartge, E.-U.; Puettmann, A.; Werther, J. Application of the Flowsheet Simulation Concept to Fluidized Bed Reactor Modeling., Part I: Development of a Fluidized Bed Reactor Simulation Module, *Chem. Eng. Process.: Process Intensification,* 2012, 60, pp. 86-95.

Hurt, R.H.; Mitchell, R.E. Unified High-Temperature Char Combustion Kinetics for a Suite of Coals of Various Rank, *Int. Symp. Combust,* 1992, 24, pp. 1243-1250.

Isshiki, M.; Mimura, K.; Zhu, Y. Oxidation Mechanism of Cu_2O to CuO at 600-1050°C, *Oxid. Met.,* 2004, 62, pp. 207-222.

Jeronimo, M.A.; Richardson, J.F. Velocity-Voidage. Relations for Sedimentation and Fluidization, *Chem. Eng. Sci.,* 1979, 34, pp. 1419-1422.

Johnson, P. C. Frictional-Collisional Constitutive Relations for Granular Materials, with Applications to Plane Shearing, *J. Fluid Mech.,* 1987, 176, pp. 67-93.

Kunii, D.; Levenspiel, O. *Fluidization Engineering*, 2nd Ed. Newton, MA, Butterworth-Heinemann, 1991.

Kunii, D.; Levenspiel, O. *Fluidization Engineering.* Newton, MA, Butterworth-Heinemann, 1991.

Leckner, B.; Lyngfelt, A.; Mattisson, T. A Fluidized-Bed Combustion Process with Inherent CO_2 Separation; Application of Chemical-Looping Combustion, *Chem. Eng. Sci.,* 2001, 56, pp. 3101-3113.

Leion, H.; Lighty, J.S., Chemical-Looping Tutorial, 38th International Technical Conference on Clean Coal & Fuel Systems, Clearwater, FL, 2013.

Leion, H.; Lighty, J.S.; Sahir, A.H.; Sohn, H.Y. Rate Analysis of Chemical-Looping with Oxygen Uncoupling (CLOU) for Solid Fuels, *Energy Fuels,* 2012a, 26, pp. 4395-4404.

Leion, H.; Lyngfelt, A.; Mattisson, T. Chemical-Looping with Oxygen Uncoupling Using CuO/ZrO_2 with Petroleum Coke, *Fuel,* 2009a, 88, pp. 683-690.

Leion, H.; Lyngfelt, A.; Mattisson, T. Chemical-Looping with Oxygen Uncoupling for Combustion of Solid Fuels, *Int. J. Greenhouse Gas Control,* 2009b, 3, pp. 11-19.

Leion, H.; Lyngfelt, A.; Mattisson, T. The Use of Petroleum Coke as Fuel in Chemical-Looping Combustion, *Fuel,* 2007, 86, pp. 1947-1958.

Leion, H.; Lyngfelt, A.; Mattisson, T. Using Chemical-Looping with Oxygen Uncoupling (CLOU) for Combustion of Six Different Solid Fuels, *Energy Proc.,* 2009, 1, pp. 447-453.

Lewis, W.K.; Gilliland, E. R.; Sweeney, W.P. Gasification of Carbon: Metal Oxides in a Fluidized Powder Bed, *Chem. Eng. Prog.*, 1951, pp. 251-256.

Lighty, J.S., Chemical Looping with Oxygen Uncoupling (CLOU) for Coal Combustion, 2012 NETL CO_2 Capture Technology Meeting, Pittsburgh, Pennsylvania, USA, 2012.

Lighty, J.S.; Sahir, A.H.; Sohn, H.Y. Kinetics of Copper Oxidation in the Air Reactor of a Chemical Looping Combustion System using the Law of Additive Reaction Times, *Ind. Eng. Chem. Res.,* 2011, 50, pp. 13330-13339.

Lighty, J.S.; Sahir, A.H.; Tingey,N.C. Leveraging CLOU Experimental Studies To Envision Design Configurations For Coal-Fired Power Plants, The 37th International Technical Conference on Clean Coal & Fuel Systems Clearwater, FL, 2012b.

Linderholm, C.; Lyngfelt, A.; Markström, P. Chemical-Looping Combustion of Solid Fuels – Design and Operation of a 100 kW_{th} Unit with Bituminous Coal, *Int. J. Greenhouse Gas Control,* 2013a, 15, pp. 150-162.

Linderholm, C.; Lyngfelt, A.; Markström, P. Operation of a 100 kW Chemical-Looping Combustor with Mexican Petroleum Coke and Cerrejón Coal, *Appl. Energy*, 2013b.

Lun, C. K.; Savage, D. J.; Jefferey, S. B.; Chepurniy, N. Kinetic Theories for Granular Flow: Inelastic Particles in Couette Flow and Slightly Inelastic Particles in a General Flowfield, *J. Fluid Mech.,* 1984, 140, pp. 223-256.

Makkee, M.; Moene, R.; Moulijn, J. A. High Surface Area Silicon Carbide as Catalyst Support. Characterization and Stability, *Appl. Catal., A,* 1998, 167*,* 2, pp. 321-330.

Mantripragada, H.C.; Rubin, E.S. IECM Technical Documentation: Chemical Looping Combustion for Pre-Combustion CO_2 Capture, 2012.

Marchisio, D. L.; Fox, R. O. Solutions of Population Balance Equations Using the Direct Quadrature Method of Moments, *Aerosol Sci.,* 2005, 36, pp. 43-73.

Mazzei, L.; Marchisio, D.; Lettieri, P. Direct Quadrature Method of Moments for Mixing of Inert Polydisperse Fluidized Powders and the Role of Numerical Diffusion, *Ind. Eng. Chem. Res.,* 2010, 49, pp. 5141-5152.

Mele, J; Shaukat, S. Scale-Up Of a Cold Flow Model Of FICFB Biomass Gasification Process to an Industrial Pilot Plant - Example of Dynamic Similarity, *Prog. Biomass Energy Production*, Croatia: Intech, 2011, pp. 1-20.

Mori, S.; Wen, C.Y. Estimation of Bubble Diameter in Gaseous Fluidized Beds, *AIChE*, 1975, 21, pp. 109-115.

Pankratz, L.B. Thermodynamic Properties of Elements and Oxides-Bulletin 672. U.S. Department of the Interior, Bureau of Mines, 1982.

Passalacqua, A.; Fox, R. O. Numerical Simulation Of Turbulent Gas-Particle Flow In A Riser Using A Quadrature-Based Moment Method, ICMF – *The 7th International Conference in Multiphase Flows,* pp. 1-11,Tampa, Florida, 2010.

Prisedsky, V.V.; Vinogradov, V.M. Fragmentation of Diffusion Zone in High-Temperature Oxidation of Copper, *J. Solid State Chem.,* 2004, 177, pp. 4258-4268.

Sarofim, A.F.; Lighty, J.S.; Smith, P.J.; Whitty, K.J.; Eyring, E.; Sahir, A.; Alvarez, M.; Hradisky, M.; Clayton, C.; Konya, G.; Baracki, R.; Kelly, K. Topical Report. Chemical Looping Combustion Reactions and Systems, March 2011.

Schaeffer, G. Instability in the Evolution Equations Describing Incompressible Granular Flow. *J. Diff., Equ.*, 1987, 66, pp. 19-50.

Shadle, L.; Shahnam, M.; Cocco, R.; Issangya, A.; Guenther, C.; Syamlal, M., et al. Challenge Problem III, NETL-PSRI - *CFB X Workshop Presentation* , Oregon, 2011.

Shen, L.; Song, Q.; Wu, J.; Xiao, J.; Xiao, R. Chemical-Looping Combustion of Biomass in a 10 kW_{th} Reactor with Iron Oxide as an Oxygen Carrier, *Energy Fuels,* 2009, 23, pp. 2498-2505.

Shen, L.; Song, T.; Wu, J.; Zhang, H. Characterization of an Australia Hematite Oxygen Carrier in Chemical Looping Combustion with Coal, *Int. J. Greenhouse Gas Control,* 2012, 11, pp. 326-336.

Sinclair, J. L.; Jackson, R. Gas-Particle Flow in a Vertical Pipe with Particle-Particle Interactions, *AIChE J.,* 1989, 35, p. 523.

Sinnott, R.K.; Towler, G. *Chemical Engineering Design: Principles, Practice and Economics of Plant and Process Design*. Butterworth-Heinemann, 2007.

Sohn, H.Y. The Law of Additive Reaction Times in Fluid-Solid Reactions, *Metall. Trans. B,* 1978, 9, pp. 89-96.

Sohn, H.Y.; Kim, B.S. A Novel Cyclic Reaction System Involving CaS and $CaSO_4$ for Converting Sulfur Dioxide to Elemental Sulfur without Generating Secondary Pollutants. 2. Kinetics of the Reduction of Sulfur Dioxide by Calcium Sulfide Powder, *Ind. Eng. Chem. Res.,* 2002, 41, pp. 3087 – 3091.

Sohn, H.Y.; Savic, M.; Padilla, R.; Han, G. A Novel Cyclic Reaction System Involving CaS and $CaSO_4$ for Converting Sulfur Dioxide to Elemental Sulfur without Generating Secondary Pollutants. 2. Kinetics of the Reduction of Sulfur Dioxide by Calcium Sulfide Powder, *Chem. Eng. Sci.,* 2006, 61, pp. 5088 – 5093.

Wen Y.Y.; Li Z.S.; Xu L.; Cai N.S. Experimental Study of Natural Cu Ore Particles as Oxygen Carriers in Chemical Looping with Oxygen Uncoupling (CLOU), *Energy Fuels,* 2012, 26, 6, pp. 3919-3927.

Whitty, K.J., Practical Challenges of System Design for a CLOU-Based System for Chemical Looping Combustion of Coal 2nd International Conference on Chemical Looping, Darmstadt, Germany, 2012.

Won, S.; Sohn, H.Y. Kinetics of the Reaction Between Hydrogen Sulfide and Lime Particles, *Metall. Tran. B,* 1985, 16B, pp. 164 – 168.

Zenz, F.A. The Fluid Mechanics of Bubbling Beds, *Fibonacci Quarterly,* 1978, pp. 171-183.

Zhu Y.; Mimura K.; Isshiki M. Oxidation Mechanism of Cu_2O to CuO at 600-1050 °C, *Oxid. Met.,* 2004, 62, 3/4, pp. 207-222.